

A photoacoustic patch for three-dimensional imaging of hemoglobin and core temperature

Received: 31 May 2022

Accepted: 1 December 2022

Published online: 15 December 2022

 Check for updates

Xiaoxiang Gao^{1,6}, Xiangjun Chen^{2,6}, Hongjie Hu^{1,6}, Xinyu Wang¹, Wentong Yue¹, Jing Mu², Zhiyuan Lou¹, Ruiqi Zhang¹, Keren Shi², Xue Chen², Muyang Lin¹, Baiyan Qi², Sai Zhou², Chengchangfeng Lu³, Yue Gu², Xinyi Yang², Hong Ding¹, Yangzhi Zhu¹, Hao Huang¹, Yuxiang Ma¹, Mohan Li¹, Aditya Mishra², Joseph Wang^{1,2} & Sheng Xu^{1,2,3,4,5} ✉

Electronic patches, based on various mechanisms, allow continuous and noninvasive monitoring of biomolecules on the skin surface. However, to date, such devices are unable to sense biomolecules in deep tissues, which have a stronger and faster correlation with the human physiological status than those on the skin surface. Here, we demonstrate a photoacoustic patch for three-dimensional (3D) mapping of hemoglobin in deep tissues. This photoacoustic patch integrates an array of ultrasonic transducers and vertical-cavity surface-emitting laser (VCSEL) diodes on a common soft substrate. The high-power VCSEL diodes can generate laser pulses that penetrate >2 cm into biological tissues and activate hemoglobin molecules to generate acoustic waves, which can be collected by the transducers for 3D imaging of the hemoglobin with a high spatial resolution. Additionally, the photoacoustic signal amplitude and temperature have a linear relationship, which allows 3D mapping of core temperatures with high accuracy and fast response. With access to biomolecules in deep tissues, this technology adds unprecedented capabilities to wearable electronics and thus holds significant implications for various applications in both basic research and clinical practice.

Monitoring biomolecules in the human body can help track wellness levels, diagnose diseases, and evaluate therapeutic outcomes. In particular, the amount and location of hemoglobin in the body provide critical information about blood perfusion or accumulation in that area. Low blood perfusion inside the body may result in severe organ dysfunctions. It can happen in many kinds of diseases (such as myocardial infarction¹, post-cardiac arrest syndrome², and vascular diseases of the extremities³), or after surgery (such as organ transplant⁴). On the contrary, accumulation of blood is often a sign of inflammation⁵,

trauma⁶, or cancer⁷. For example, cysts with many possible types of biofluids inside may be found throughout the human body. Bloody cysts are suspicious and should be further examined and closely monitored for the risk of malignant tumors^{8,9}. Continuous monitoring can benefit understanding and diagnosing these pathophysiological conditions, and thus enable timely medical interventions to achieve better outcomes. However, existing methods are not designed for continuous monitoring on individual patients: some necessitate costly equipment, such as magnetic resonance imaging; some rely on

¹Department of Nanoengineering, University of California San Diego, La Jolla, CA 92093, USA. ²Materials Science and Engineering Program, University of California San Diego, La Jolla, CA 92093, USA. ³Department of Electrical and Computer Engineering, University of California San Diego, La Jolla, CA, USA. ⁴Department of Radiology, School of Medicine, University of California San Diego, La Jolla, CA 92093, USA. ⁵Department of Bioengineering, University of California San Diego, La Jolla 92093 CA, USA. ⁶These authors contributed equally: Xiaoxiang Gao, Xiangjun Chen, Hongjie Hu. ✉ e-mail: shengxu@ucsd.edu

radioactive tracers, such as positron emission tomography¹⁰. Ultra-sonography can image internal tissues and blood flow, but requires an operator and a separate lasing system for biomolecule sensing¹¹. The recent advances in soft electronics have given rise to soft patches that can adhere to the human skin for continuous health monitoring^{12–14}. These devices have demonstrated their capability in biomolecule sensing based on electrochemical reactions^{15–22} and optics^{23,24}. However, existing soft patches can only sense biomolecules close to the skin surface. None of them has access to biomolecules in deep tissues, which have a stronger and faster correlation with the physiological and metabolic processes in the human body than those close to the skin surface²⁵ (Supplementary Note 1, Supplementary Table 1).

Here we report a photoacoustic patch for continuous sensing of biomolecules in deep tissues. The device integrates an array of high-power VCSEL diodes and piezoelectric transducers, which are interconnected by serpentine metal electrodes and encapsulated in an elastomeric matrix. Pulsed laser emitted from the VCSEL array excites hemoglobin molecules to radiate acoustic waves. Those photoacoustic waves will be received by the transducer array and then processed to reconstruct a 3D map of the hemoglobin with a sub-millimeter resolution. Moreover, the photoacoustic signal amplitude has a linear relationship with the media temperature²⁶, which provides a noninvasive way for core temperature measurement with a high spatial resolution and fast response. This work integrates laser sources and piezoelectric transducers into an electronic patch, which is unique in design, fabrication, and working principle among all existing wearable electronic patches (Supplementary Note 2).

Results

Design, fabrication, and working principle of the soft photoacoustic patch

Figure 1a schematically illustrates the design and working principle of the soft photoacoustic patch. The patch includes a VCSEL array as the light source and a piezoelectric transducer array for photoacoustic wave detection. The laser beams are diffused in deep tissues. Hemoglobin molecules will undergo thermoelastic expansion after absorbing optical energy and collapse when the energy is absent. Therefore, when illuminated by the pulsed laser from the VCSEL array, hemoglobin will vibrate and emit acoustic waves. The piezoelectric transducers will receive the acoustic waves for generating the spatial distribution of the wave emitters. Therefore, photoacoustic imaging takes advantages of the unique absorption characteristics of biomolecules and highly penetrating acoustic waves to achieve high spatial resolution mapping of biomolecules in deep tissues.

In the patch, 24 VCSELS are evenly distributed in four equally spaced columns (Methods, Figs. S1–S3). The VCSELS in each column are connected in series. The distributed VCSEL layout can help generate uniform illumination in regions below the patch (Fig. S4). 240 piezoelectric transducers are arranged in between the VCSELS, in 15 columns with 16 transducers in each column. To address each transducer independently with a compact device profile, seven layers of serpentine interconnects are designed (Fig. S5). Four adjacent elements in the column are virtually connected in parallel to enhance the signal in the image reconstruction process (Fig. S6), forming 13 linear arrays in the row direction (Fig. S7). The overlap between adjacent arrays can increase the number of imaging planes, further improving the lateral resolution in the overlapping direction (Fig. S8). The VCSELS, transducers, and interconnects are all encapsulated in an elastomeric polymer, forming an “island-bridge” structure with an overall footprint of 2.0 cm × 1.6 cm and a thickness of 1.2 mm (Methods). In comparison with conventional photoacoustic imaging systems that need complicated components and strict operation environments (Fig. S9, Supplementary Note 3, Supplementary

Table 2), the integrated wearable photoacoustic patch greatly reduces the physical constraint on the human body, potentially allowing imaging on moving subjects.

High-power VCSELS are used in this study to achieve a great detection depth and a large signal-to-noise ratio (SNR). A wavelength of 850 nm is used because it has deep-tissue penetration and is in the first optical window for probing human tissues^{27,28} (Supplementary Note 4). Hemoglobin also has the dominant optical absorption coefficient compared with other molecules, such as water and lipid, at this wavelength. Furthermore, VCSEL at 850 nm wavelength is most commonly available because, on the one hand, 850 nm is a common optical wavelength whose attenuation in fibers is relatively low²⁹; on the other hand, silicon-based 850 nm photodetectors are low-cost and widely used³⁰. The receiving transducer element is composed of a piezoelectric layer and a backing layer (Figs. S10, S11). The piezoelectric layer is made of 2 MHz lead zirconate titanate (PZT) micropillars embedded in epoxy. Compared with bulk PZT, the 1–3 composite suppresses the transverse vibration and enhances the axial vibration of the PZT micropillars, thereby increasing the electromechanical coupling coefficient and improving the energy conversion efficiency. The backing layer, made of cured silver epoxy, has a high electrical conductivity and a strong attenuation effect on acoustic waves to dampen excessive vibrations and thus improve the signal bandwidth and axial resolution of the transducers (Fig. S12).

The as-fabricated soft photoacoustic patch is mechanically and electrically robust. Figure 1b shows the photographs of the patch under different modes of deformation, including bending on a developable surface, wrapping on a nondevelopable surface, and twisting and stretching. The photoacoustic patch is rigid locally at each piezoelectric transducer element and laser diode but soft globally on the system level. No external pressure is required to conformally attach the photoacoustic patch to the skin (Fig. S13). Figure 1c presents the infrared camera images of the patch during operation (850 nm laser wavelength). Mechanical deformations do not affect the performance of the VCSELS (Fig. S14).

Optical, thermal, and acoustic characterizations of the soft photoacoustic patch

The optical energy distribution in the tissue should be as uniform as possible to minimize systematic artifacts introduced to the photoacoustic images. Optical attenuation needs to be minimal to ensure the greatest detection depth. Figure 2a shows the simulated optical intensity in a 2 cm × 2 cm × 2.5 cm human muscle tissue (Methods). Each VCSEL emits a laser beam perpendicular to the diode surface into the tissue with a divergence angle of 20° and a peak power of 40 W per VCSEL (Methods). The top surface in Fig. 2a corresponds to the interface between the patch and the tissue. The simulated optical intensity distribution in four planes cross-sectioning the illuminated volume is characterized (the bottom panels of Fig. 2a). The origin of coordinates is set at the central point of the photoacoustic patch. The optical intensities in the plane 1 (XZ plane at $y=0$) and plane 2 (YZ plane at $x=0$) show uniform distribution in the horizontal direction and small attenuation along the axial direction. In the XY plane, the distributions are highly uniform, with 20% and 2.3% of the incident intensity at the depths of 1 cm (plane 3) and 2 cm (plane 4), respectively. This indicates the ability of the laser beams to penetrate thick tissue layers. The optical intensity distributions of a stretched, bent, and twisted VCSEL array under normal mechanical deformations induced by the skin are tested. The 20% uniaxially stretched array shows an optical distribution very similar to that of an undeformed array (Fig. S15, Methods).

VCSELS in operation will generate a lot of heat. Excessive heat will not only raise safety concerns, but also degrade the VCSEL performance³¹ and change the sensitivity of piezoelectric transducers (Figs. S16, S17). Figure 2b shows the thermal images of the patch on a

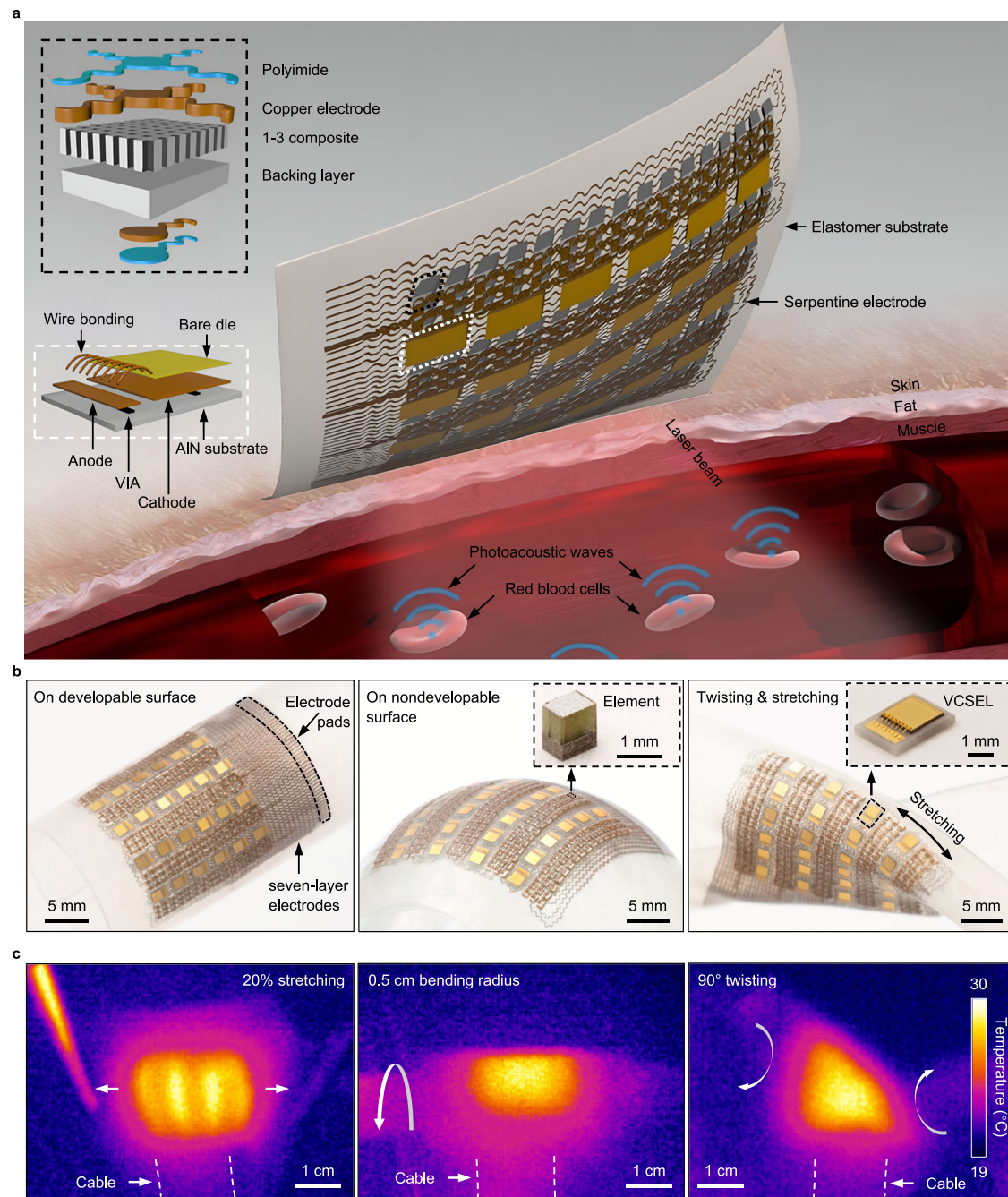


Fig. 1 | Design, fabrication, and working principle of the soft photoacoustic patch. **a** Schematics of the device structure and the working principle. The patch comprises an array of VCSELs and an array of piezoelectric transducers, interconnected by serpentine copper electrodes. All components are encapsulated in Ecoflex. Upon absorption of the optical energy, the hemoglobin molecules in red blood cells undergo thermoelastic expansion and radiate acoustic waves into the surrounding media. The photoacoustic waves will be collected by the transducer array and then relayed to a backend system for data processing. AlN: aluminum

nitride. VIA: vertical interconnect access. VCSEL: vertical-cavity surface-emitting laser. **b** Optical photographs of the soft photoacoustic patch under different modes of deformation, including bending on a developable surface, wrapping on a non-developable surface, and stretching and twisting. Insets in the middle and right panels are optical micrographs of a single transducer element and a VCSEL diode, respectively. **c** Infrared camera images of the soft photoacoustic patch when the VCSELs (850 nm laser wavelength) are in operation under different modes of deformation, including stretching, bending, and twisting.

human arm immediately after turning on the lasers (top panel) and after continuous operation for an hour (bottom panel) at a repetition frequency of 3 kHz and a pulse duration of 200 ns (Fig. S18). A relatively long pulse, i.e., 200 ns, is used to enhance the signal-to-noise ratio, which is close to the pulse duration in other studies that utilize LEDs or laser diodes as the light sources^{32–34} (Fig. S19). After one-hour operation, the maximum temperature measured was $\sim 36^\circ\text{C}$, slightly higher than the skin surface temperature, but still comfortable for the subject.

The photoacoustic patch generates as much heat as ultrasound-phased arrays³⁵, both of which are within safety standards. Figure 2c presents the changes in incident intensity from the VCSELs during continuous operation. At 3 kHz pulse repetition frequency and 200 ns pulse duration, the intensity decreases by only $<4\%$ after one hour, showing the high stability of the VCSELs.

For quantitative photoacoustic studies, it is critical for the transducer array to have a uniform distribution of detection sensitivity

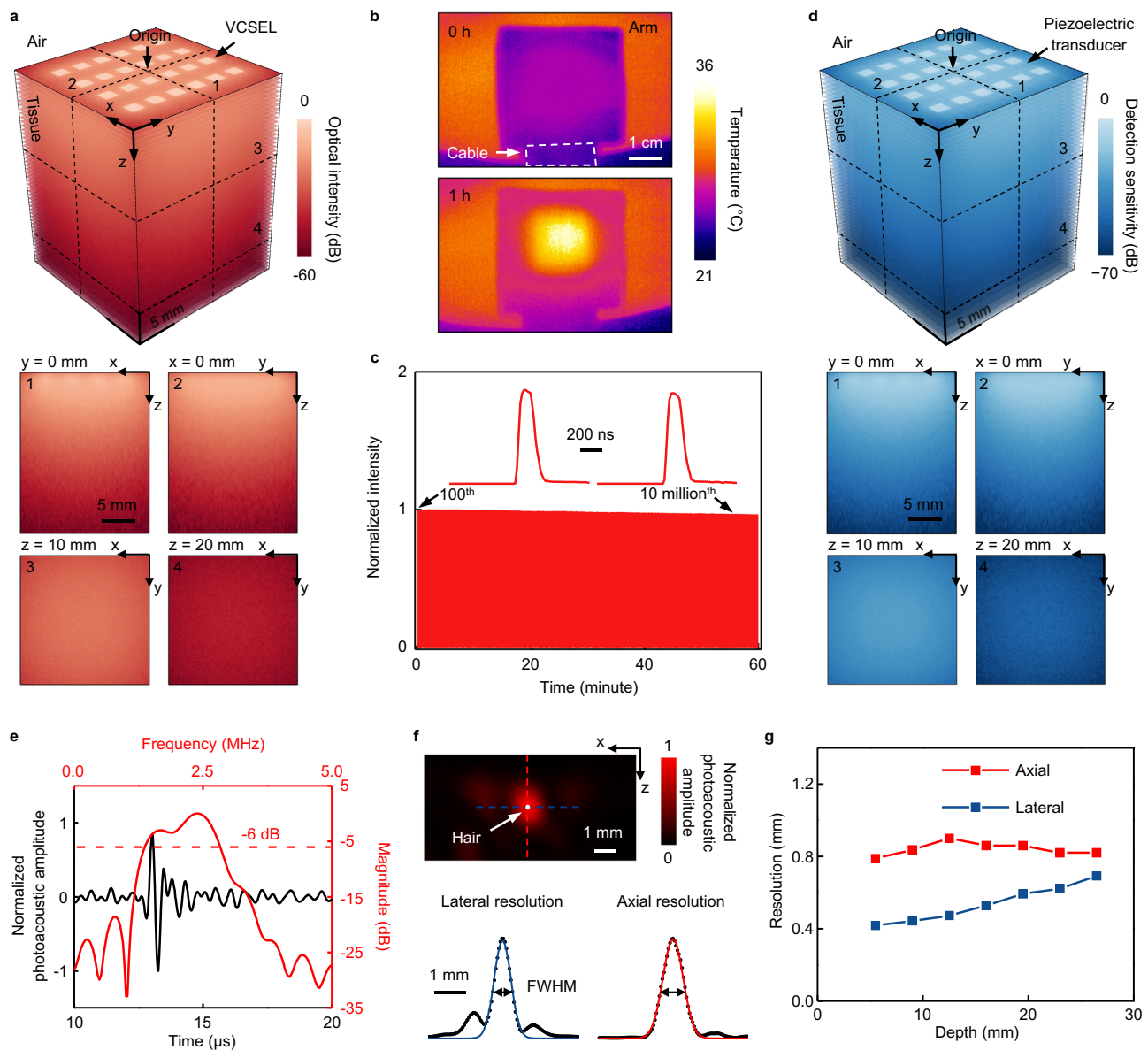


Fig. 2 | Characterizations of the soft photoacoustic patch. **a** Simulated optical intensity distribution in tissue. The 3D distribution map comprises 51 horizontal planes stacked together with display transparency of 60%. The four slices at the bottom panel highlight the optical intensity distribution at different cross-sections. VCSEL: vertical-cavity surface-emitting laser. **b** Thermal imaging of the photoacoustic patch on the arm immediately after turning on the lasers and after one hour of continuous operation. The maximum temperature is below 36 °C, which is comfortable for long-term wear. **c** Testing of the VCSELs' output stability as they continuously work for 1 h with a pulse duration of 200 ns at a pulse repetition frequency of 3 kHz. The insets correspond to the 100th and the 10 millionth pulses. The decrease in normalized light intensity after an hour is <4%. **d** Simulated

photoacoustic detection sensitivity distribution in tissue. The 3D distribution map comprises 51 horizontal planes stacked together with display transparency of 60%. The four slices at the bottom panel highlight the detection sensitivity distribution at different cross-sections. **e** Photoacoustic impulse response of the patch, in both time and frequency domains, characterized by detecting signal of a hair excited by the VCSELs. **f** A photoacoustic image of a hair at a depth of 2 cm in a gelatin phantom. The blue and red curves are the Gaussian fit to the lateral and axial photoacoustic amplitude profiles (black dots), respectively. The lateral and axial resolutions are determined by the FWHM in different directions. **g** The lateral and axial resolutions at different depths.

to photoacoustic signals in the target region. Figure 2d shows the simulated photoacoustic sensitivity distribution of the patch in the 2 cm × 2 cm × 2.5 cm human breast tissue in consideration of nonuniform light distribution in Fig. 2a (Methods, Fig. S20). Due to the remarkable penetration of acoustic waves in human tissues, the detection sensitivity loss caused by the wave-sensing ability of piezoelectric transducers is < -10 dB. The high detection sensitivity ensures the high imaging depth of the photoacoustic patch. The tested transmitting and receiving properties of piezoelectric transducers demonstrated their high penetration depth and uniform sensitivity (Figs. S21–S23, Methods).

The impulse response is a critical characteristic of a sensing system (Methods, Figs. S24, S25), which is characterized by the time domain photoacoustic signal of a linear source excited by the VCSELs in this study. We measured the photoacoustic signals of a human hair (with a diameter of ~80 μm). The working frequency of the system is then characterized by applying Fourier Transform to the temporal photoacoustic signal (black curve) received by one transducer element (Fig. 2e). As the optical intensity of VCSELs is much lower than a conventional bulky laser, photoacoustic signals in the time domain are averaged to increase the SNR. On the other hand, the times of averaging will reduce the frame rate of imaging. To balance the SNR and

frame rate in this study, the times of averaging are 3000 (Fig. S26), yielding a frame rate of 1 Hz and a SNR^{36–38} of 26.8 dB (signal of a hair at a depth of 2 cm in a gelatin phantom) at a lasing pulse repetition frequency of 3 kHz. The red curve shows the impulse response in the frequency domain, with a center frequency of 2.40 MHz and a bandwidth of 1.47 MHz (Figure 2e).

Imaging resolutions are characterized based on a linear source. Photoacoustic images are reconstructed based on signals generated by hairs embedded in gelatin phantoms at different depths^{39–42}. Figure 2f displays a 2D photoacoustic image of a hair at a depth of 2 cm (Methods, Fig. S27). The amplitude profiles (black dots) of the photoacoustic image in the lateral and axial directions are fitted by the Gaussian function, illustrated by the blue and red curves, respectively (the bottom panel). The image resolution is determined by the full width at half maximum (FWHM) of the Gaussian curve fit to the profile^{40–43}. The axial resolution is mainly determined by the signal frequency and remains almost constant at -0.8 mm for different imaging depths (Fig. 2g). The lateral resolution will be reduced from -0.4 mm to -0.7 mm as the imaging depth increases because of the degraded focusing (Fig. 2g).

Ex-vivo 3D hemoglobin mapping and core temperature measurement

The wavelength of 850 nm is critical for a high penetration depth in human tissues^{27,28}. Additionally, for photoacoustic mapping of hemoglobin amongst other biomolecules in the tissue, a laser wavelength where hemoglobin absorption is dominant needs to be selected. To characterize the sensing selectivity at this wavelength, we tested cyst phantoms with five different biofluid inclusions, including water, plasma, milk, fat, and bovine whole blood, in transparent colorless silicone tubes embedded underneath a 2 cm thick porcine tissue (Fig. S28). Figure 3a shows the measured optical absorption spectra of all types of biofluids (Methods), which shows that bovine whole blood has the dominant absorption coefficient at 850 nm. To further verify the selectivity, both ultrasound and photoacoustic images of the cyst phantoms are collected (Fig. 3b, Methods). Ultrasound-based B-mode images can only detect the acoustic impedance mismatch between different tissues, which is why the boundaries between the inclusions and matrixes are clear, while the types of biofluids are indistinguishable. The photoacoustic images are based on the contrast of optical absorptions, which differentiates the blood from other biofluids (Fig. S29).

16 rows of transducers form 13 linear arrays, each of which can produce a 2D photoacoustic image. Combining the 13 images, the patch can generate a 3D map of hemoglobin. The 3D mapping performance is tested on two crossed silicone tubes filled with bovine blood embedded underneath a 2 cm thick porcine tissue. Figure 3c shows a slice of the 3D map where the two silicone tubes overlap (top panel) and the corresponding photoacoustic signal amplitude profile along the green dashed line in the top panel (bottom panel). All 13 slices of the photoacoustic images are displayed in Fig. 3d, where the slice with overlapped tubes in Fig. 3c is highlighted. Figure 3e gives the integrated 3D mapping of hemoglobin at a depth of 2 cm (Figs. S30, S31). The patch can also distinguish two overlapping vessels (Fig. S32). When the stretching strain is within 15%, the patch performance is minimally affected (Fig. S33).

Core temperature is critical for governing the essential functions of the body and should be maintained near 37 °C⁴⁴. It typically fluctuates within 1 °C according to circadian rhythm⁴⁵, but can reach -40 °C amid strenuous workload or -35.6 °C in cold environments. A significant deviation of the core temperature indicates failing thermoregulation⁴⁴ with dire consequences^{46–49}, sometimes life-threatening. Most soft patches can only measure the temperature on the skin surface, which can be easily affected by the external environment and thus has a weak correlation to the core temperature.

Noninvasive sensing of core temperature is mainly based on Zero-Heat-Flux^{50,51} or Dual-Heat-Flux^{52,53} thermal models, which have long response time (~3 min)⁵¹ and limited detection depths (~1 cm)⁵¹ (Supplementary Note 5, Supplementary Table 3).

Photoacoustic signals are generated when the biomolecules convert the pulsed optical energy to mechanical energy in the form of photoacoustic waves⁵⁴. In the range of 10–55 °C, there is a linear relationship between the amplitude of photoacoustic waves and the temperature²⁶ (Supplementary Note 6), allowing the measurement of temperature by the photoacoustic approach. As an initial test, we used the soft photoacoustic patch to measure the temperature in a phantom and checked its performance with thermocouples (Fig. S34). The phantom is composed of warm bovine blood injected in transparent silicone tubes underneath 2 cm thick room-temperature porcine tissues. Thermocouples were placed in the tubes, where the photoacoustic measurements were also taken. We demonstrate the high accuracy (Fig. S35, Supplementary Note 7), spatial temperature mapping, and fast response (Fig. S36) of the photoacoustic patch in core temperature measurement by detecting static blood, as validated by the thermocouple.

To monitor flowing blood, we tested the core temperature of an ex-vivo porcine tissue (Fig. S37). A pump drove the blood to flow in a transparent silicone tube with an inner diameter of 3 mm. The flow rate was set to be -9 mL s⁻¹, resulting in a blood flowing speed of -127 cm s⁻¹, faster than the blood flow velocity of most blood vessels in the human body⁵⁵. The two ends of the tube were immersed in a beaker containing bovine blood, which was placed on a hot plate to heat the blood to different temperatures during flowing. The blood could also naturally cool down while the hot plate was turned off. A portion of the tube was embedded underneath a porcine tissue at a depth of -2 cm, which was measured by the photoacoustic patch. A thermocouple was inserted into the tube to measure the blood temperature simultaneously and record the data continuously. Figure 3f shows the beamformed photoacoustic amplitude (black dots) of flowing blood measured by the photoacoustic patch and the temperature (red line) measured by the thermocouple, which agree well with each other during the entire dynamic process. Two cycles of heating and cooling were tested, lasting -82 min. Figure 3g presents the scatter plot of the photoacoustic amplitude as a function of the thermometer temperature. The fitting of the measured data ($R^2 = 0.987$) demonstrates the linear relationship between the photoacoustic amplitude and the temperature in flowing blood.

In-vivo 3D imaging of blood vessels and venous occlusion test

To test the feasibility of in-vivo monitoring, we used the photoacoustic patch to image veins in the hand, foot, thigh, and forearm, monitor the venous response to the occlusion test, and image the internal jugular vein (IJV) (Fig. S38, Methods). Figure 4a-h presents the photos of a volunteer's hand, foot, thigh, and forearm, where the target veins are labeled. The photoacoustic patch acquired 13 cross sections of the veins, which were then converted to 3D images, respectively, as shown at the sides of corresponding photos. The 3D images clearly display the vein structures of different body locations. In comparison to Doppler ultrasound imaging³⁵, photoacoustic imaging has high sensitivity and contrast in detecting blood vessels, especially for small blood vessels with slow blood flow⁵⁶ (Fig. S39). Note that the flexible photoacoustic patch may also be affected by motion artifacts (Fig. S40), a common problem in existing wearable electronic devices^{57–59}. The volunteer kept the arm static during the measurements to minimize any motion artifacts.

Venous occlusion plethysmography is a noninvasive tool to assess the blood flow and vascular resistance of limbs^{60,61}. In the measurements, venous return from the forearm was briefly interrupted by inflating a cuff, wrapped around the upper arm, to above venous pressure but lower than the diastolic pressure (Methods).

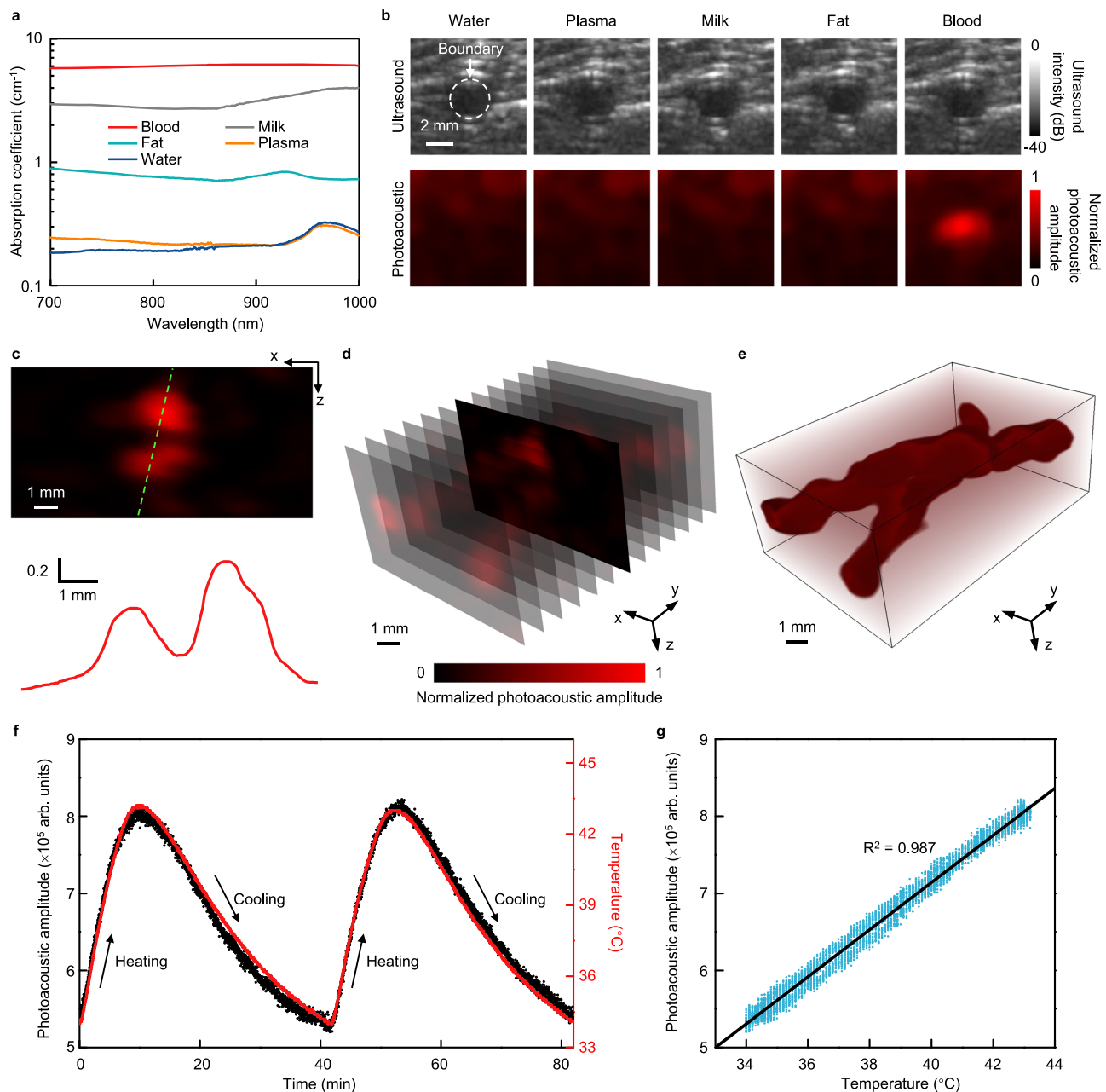


Fig. 3 | Ex-vivo 3D imaging of hemoglobin and monitoring of core temperature in deep tissues. **a** Optical absorption spectra of different body fluids. Absorption coefficients of water, plasma, milk, fat, and bovine whole blood are 0.197, 0.214, 2.716, 0.722, and 6.114 cm^{-1} at the wavelength of 850 nm, respectively. **b** Ultrasound B-mode and photoacoustic images of different cysts embedded in a porcine tissue at a depth of 2 cm. The ultrasound B-mode images, acquired by a commercial ultrasound probe, show no differences because of the low acoustic impedance contrast between various fluids. The soft photoacoustic patch differentiates the blood cyst based on the high optical absorption contrast. **c** A high-

resolution photoacoustic image of a blood vessel phantom, which contains two silicone tubes filled with blood embedded underneath a 2 cm thick porcine tissue. The red curve at the bottom panel shows the profile along the green dashed line. **d** 13 slices of photoacoustic images of the blood vessel phantom with display transparency of 80%. **e** 3D imaging of hemoglobin at a depth of 2 cm in porcine tissue. **f** Comparison between the beamformed photoacoustic signal amplitude and temperature of flowing blood during two cycles of heating and cooling. **g** Linear fitting of the photoacoustic amplitude and temperature.

As a result, the venous dimension will increase as the arterial blood inflow. We attached the photoacoustic patch on the forearm, above the veins, and continuously monitored the dynamic vascular response to a venous occlusion (Supplementary Movie 1). Figure 4i shows the change of the vein size during a 3 min continuous recording. Insets show the photoacoustic images of the vein at three different moments. The image pixels with a normalized value >0.5 were counted into the vein area⁶², as labeled by the white boundaries. No pressure was applied in the first 1 min, thus no significant area change was observed. At 60 seconds, the cuff was quickly inflated to

70 mmHg, resulting in an increasing vein area with the time. Inset image 2 presents an obvious expansion of the vein compared to inset 1. The cuff was rapidly released after 1-min inflation, accompanied by a dramatic drop in the vein area. Those results are similar to others acquired by bulky photoacoustic systems⁶³. The venous occlusion test demonstrated the fast response of the photoacoustic patch for in-vivo imaging.

We used the photoacoustic patch to 3D image the IJV ($>1.1 \text{ cm}$ in depth) in the neck (Fig. 4j and Fig. S41). Figure 4k shows 13 slices of photoacoustic images of the IJV superimposed on the corresponding

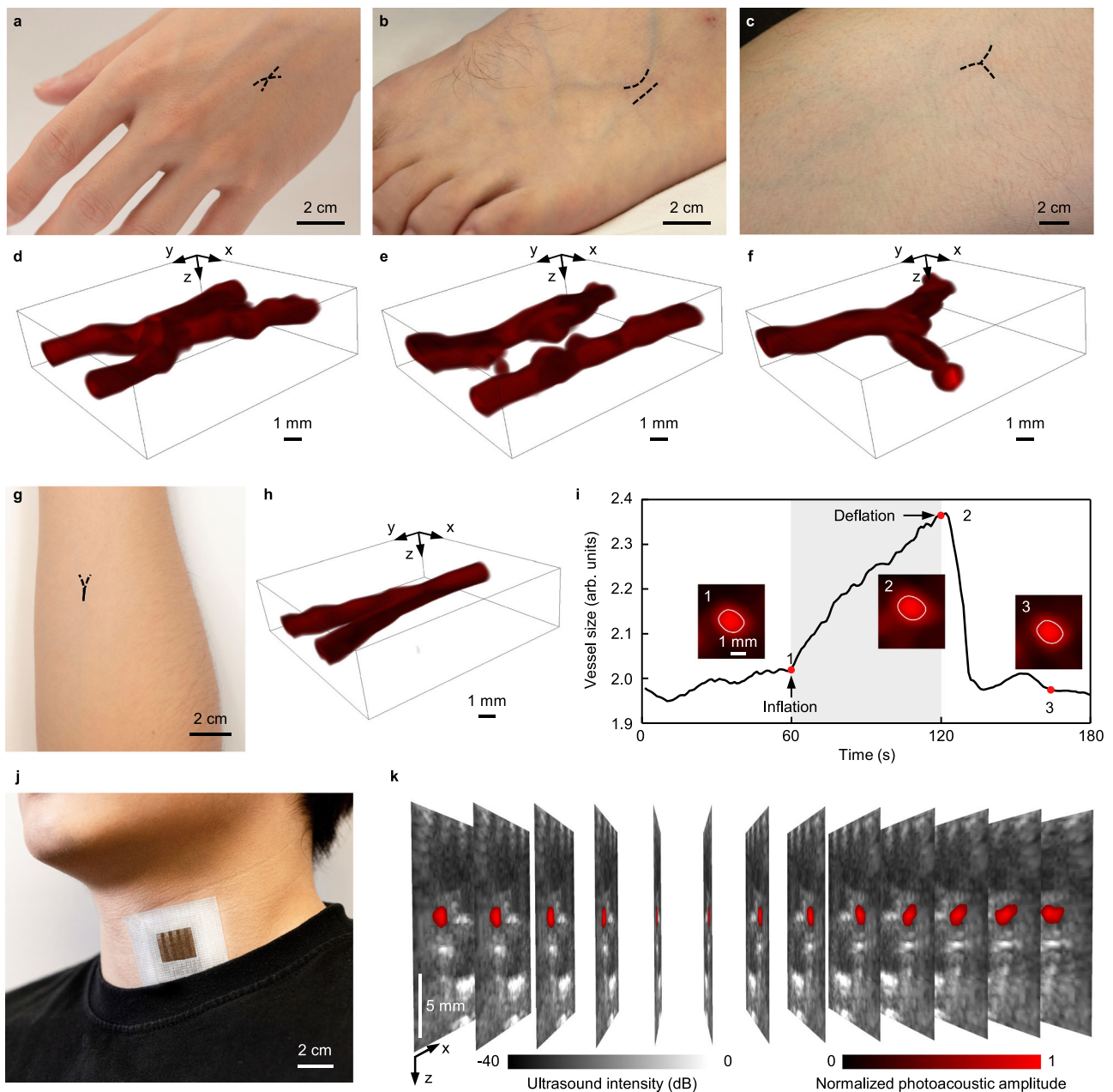


Fig. 4 | In-vivo imaging of blood vessels and venous occlusion test. a–h Photos of the hand, foot, thigh and forearm where the target veins are highlighted. The reconstructed 3D photoacoustic images are all shown accordingly. **i** Cross sectional size changes of the vein before cuff inflation, during cuff inflation with a pressure of 70 mmHg, and cuff deflation. The pixels inside the white boundary with a value >0.5

are counted to calculate the vein size. **j** A photograph of the patch attached to the human neck at a location above the internal jugular vein. **k** 13 slices of dual-mode images acquired by the photoacoustic patch, i.e., photoacoustic images of the internal jugular vein superimposed on ultrasound B-mode images. The pixel values of normalized photoacoustic images < 0.5 are not shown.

ultrasound B-mode images (Fig. S42), which are all acquired by the photoacoustic patch. The central frequency of the ultrasound transducers is close to 2 MHz, which results in the low contrast of the IJV in the ultrasound B-mode image. On the contrary, the IJV shows high contrast to other surrounding tissues in the photoacoustic image (Fig. S43), benefiting from the strong optical contrast between the hemoglobin and other molecules. The irregular skin curvature has a minimal influence on the imaging resolutions of the photoacoustic patch, due to the relatively low acoustic working frequency (Figs. S44, S45 and Supplementary Note 8). The carotid artery is invisible in the photoacoustic images because its strong pulsation will induce unstable phases to the photoacoustic signals and therefore damage their coherent averaging^{64,65} (Fig. S46).

Discussion

The soft photoacoustic patch demonstrated in this study allows for continuous, noninvasive mapping of hemoglobin and core temperature with high spatial resolution in real time. This work reports using soft electronic devices for 3D imaging of biomolecules in deep tissues (>2 cm in ex-vivo tests and >1.1 cm in in-vivo tests). The high-resolution imaging of hemoglobin will enable the monitoring of hemodynamics and vascular proliferation in tissues to manage a variety of conditions and diseases. Monitoring the dimension of blood vessels can be valuable for evaluating vessel functions and diagnosing vascular diseases. For instance, measuring the dynamic change of the vein diameter during an occlusion can help examine venous compliance, which is a strong indicator of cardiac function⁶⁰. The photoacoustic effect-based

temperature measurements, with the advantages of deep penetration, high accuracy, and fast response, introduce a strategy for monitoring the core temperature, e.g., during exercise, anesthesia, and surgical hypothermia, in fundamental biomedical research and clinical practice^{66,67}.

Although the photoacoustic patch discussed here only detects hemoglobin, this platform technology can potentially be extended to monitor many other endogenous biomolecules, such as melanin^{68,69}, glucose^{70–72}, lipid^{73,74}, cytochrome⁷⁵, nucleic acid⁷⁶, and proteins^{77,78} (Supplementary Note 9). Furthermore, exogenous contrast agents, like single-walled carbon nanotubes⁷⁹, gold nanoparticles⁸⁰, and methylene blue⁸¹, can further enhance the signal intensity, increase the detection depth, and improve the detection specificity⁸². The laser wavelength is the key to selectively monitoring various biomolecules. Integrating multiple laser diodes with different wavelengths on the photoacoustic patch can expand the portfolio of detectable biomolecules, with more accurate targeting of biomolecules by detecting a set of absorption characteristics at different wavelengths. It is possible to integrate two or more wavelengths VCSELs in the patch as VCSELs with a wide wavelength range have been developed, from blue light⁸³ (447 nm) to infrared light⁸⁴ (1550 nm), which overlaps with the typical wavelength range in photoacoustic imaging applications.

The current detection depth is still limited by the optical intensity of the VCSELs. It is challenging for the photoacoustic patch to image the cardiac region because the optical power of laser diodes used in this work is not as high as expensive bulky high-power lasers. The depth of the cardiac region ranges from several centimeters to >17 centimeters⁸⁵. The average shortest distance between the heart and the skin is about 3.1 cm when detecting from the apical view⁸⁶. This large imaging depth is currently not achievable by the wearable photoacoustic patch. In-vivo photoacoustic imaging of the human heart represents a grand challenge in the field, even using conventional bulky photoacoustic systems with expensive high-power lasers. In this work, we achieved an ex-vivo imaging depth of ~2 cm in porcine tissues and an in-vivo imaging depth of ~1 cm. Higher power VCSELs will be needed to further increase the detection depth to the regions of visceral organs. Additionally, developing higher power VCSELs, by either fabricating larger VCSELs with more light emitting elements (Figs. S3, S47) or constructing driving circuits with higher output current, will be essential for increasing the SNR of photoacoustic signals and thus reduce the times of averaging for imaging dynamic arteries.

Photoacoustic imaging without calibration can only monitor relative temperature changes. A calibration process that establishes the relationship between photoacoustic amplitude and absolute temperature can enable photoacoustic imaging to monitor absolute temperature. In this work, we demonstrated monitoring absolute core temperature in ex-vivo porcine tissues. While monitoring the photoacoustic amplitudes of blood, we recorded the absolute temperature simultaneously by a thermocouple. Therefore, the photoacoustic amplitude could be calibrated and transferred to absolute temperature. For in-vivo applications, photoacoustic imaging can monitor relative temperature changing without calibration. Invasive temperature catheters can be used for calibration. It is worth mentioning that for long-term monitoring, the calibration is only required once.

Before applying the photoacoustic patch to monitor blood temperature in the human body, additional challenges need to be solved. First, a gold standard technique for core temperature measurement is required to calibrate the photoacoustic amplitude. Some noninvasive core temperature sensors based on thermal flux models suffer from slow response and lack of spatial resolution, which are not suitable for calibration in this case. Invasive catheters can be directly inserted into the blood vessel to monitor temperature, but it is too invasive. Second, some other factors may also affect the photoacoustic signals, such as the amount of blood perfusion. More advanced methods should be

developed to eliminate the influence of these factors, such as the thermal memory based photoacoustic technique⁸⁷.

We adopted data averaging and bandpass filter to improve the signal-to-noise ratio. A high pulse repetition rate, i.e., 3 kHz, is used to ensure a high imaging frame rate (Supplementary Note 10). Although data averaging is a common and convenient way, thousands of times of averaging makes it time-consuming, causing more laser exposure. Besides, there are other methods for enhancing the SNR while requiring less time consumption (Supplementary Note 11), such as coded excitation^{88–91}, empirical mode decomposition^{92,93}, wavelet thresholding^{94,95}, Wiener deconvolution⁹⁶, and adaptive filtering⁹⁷. These methods and the data averaging can be adopted together to achieve better SNR⁹². In the current design, bulky ultrasound probes and sophisticated laser machines are eliminated, which have significantly improved the device portability and ease of use, but the photoacoustic patch is still wired to a backend system for signal acquisition and processing. Future efforts can focus on miniaturizing the control electronics to realize a fully integrated wearable system and, therefore, enable measurements on-the-go (Fig. S48).

Methods

Human experiment protocols

All human tests were performed under University of California San Diego Institutional Review Board (IRB) approval (number 800975). One 25-year-old male volunteered to be tested with informed consent obtained without compensation. For the venous occlusion experiment, the volunteer sat on a chair with a pressure cuff worn on the upper arm. The vertical distance between the neck and the forearm was about 30 cm. Then we attached the photoacoustic patch on the forearm above the veins using a medical tape. After that, the venous occlusion was performed: (1) No pressure was applied to the cuff in the first 1 minute; (2) inflate the cuff to 70 mmHg immediately and maintain for 60 s; (3) deflate the cuff to zero to let the veins recover to the normal status. In the detection of the internal jugular vein, the volunteer sat on a chair with the photoacoustic patch attached to the neck with a medical tape. For the imaging of veins in the hand, foot, thigh, forearm and venous occlusion test, a 1 cm-thick gelatin phantom was placed between the patch and skin to compensate non-uniform light distribution (Fig. S38).

Fabrication of laser diode chips

The fabrication process of the VCSEL diode chip is schematically illustrated in Fig. S2. The anode and cathode of the VCSEL die (850 nm, Ace Photonics) are on the top and bottom surfaces (Fig. S3), respectively. To facilitate the fabrication of the photoacoustic patch, the anode and cathode are routed to the same surface by creating vertical interconnect accesses (VIAs) and wire bonding. Two vertical openings were created by laser ablation in a 1.7 mm × 2.4 mm × 0.25 mm aluminum nitride (AlN) substrate and filled with silver epoxy (E-Solder 3022). The silver epoxy VIAs were cured in an oven at 80 °C for 2 h. The AlN substrate was cleaned with acetone and isopropyl alcohol to remove organic contaminants, followed by rinsing with DI water and drying with nitrogen gas. Moisture induced in the cleaning process was removed by baking the samples in a vacuum oven at 100 °C for 10 min. A lift-off process allowed patterning metal electrodes on AlN. The process involved photolithography (photoresist AZ 1529: spin-casting at 4000 r.p.m. for 60 s, baking on a hotplate at 95 °C for 120 s, UV irradiance at 350 mJ cm⁻², and developing for ~40 s with developer AZ 300 MIF) and then sputtering (Ti: 200 W, 3.0 mTorr, 5 sccm Ar, 5 min, ~50 nm; Au: 200 W, 3.0 mTorr, 5 sccm Ar, 15 min, ~400 nm). The sample surface was activated (reactive ion etching: 50 W, 50.0 mTorr, 35–40 °C, 50.0 sccm O₂, 30 s) before sputtering. The samples were soaked in acetone for 30 min to thoroughly remove all photoresists and lift off the metals on the top of the photoresists. Moisture induced in the lift-off process was removed by baking the samples in a vacuum oven at 100 °C for 10 min. The VCSEL die was then

pasted on the ground electrode pad on AlN with silver epoxy, which was cured in an oven at 80 °C for 2 h. The anodes of the VCSEL die and AlN substrate were connected with wire bonding.

Fabrication of the photoacoustic patch

The fabrication process can be generalized into three steps: (1) patterning of the stretchable multilayered electrodes, (2) preparation of the VCSEL diode chips and ultrasonic transducer array, and (3) soft packaging. Cu foils with 20 μm thickness were used as the multilayered conductive interconnects. To adhere the interconnects on the soft elastomeric substrate tightly, a PI thin film [poly(pyromellitic dianhydride-co-4,4'-oxydianiline) amic acid solution, PI2545 precursor, HD Microsystems] was spin-coated on the Cu, at the speed of 4000 r.p.m, with an acceleration of 5000 r.p.m per second, for 60 s. The PI was cured by soft baking at 100 °C for 3 min and hard baking at 300 °C for 1 h under a nitrogen atmosphere. The PI-based Cu foil was activated by ultraviolet light (PSD series Digital UV Ozone System, Novascan) for 2 min and then laminated on a temporary PDMS substrate (base to hardener ratio is 20:1, Sylgard 184 silicone elastomer). The ultraviolet light activation strengthens the bonding between the PI and the PDMS substrate. A nanosecond laser (Laser Mark's, central wavelength, 1059–1065 nm; power, 0.228 mJ; frequency, 35 kHz; speed, 300 mm s⁻¹; and pulse width, 500 ns) was used to ablate the Cu/PI into the "island-bridge" serpentine layout. The electrode patterns were designed by AutoCAD (Autodesk, USA). The patterned Cu/PI thin film was transferred to an Ecoflex substrate (15 μm thick; Ecoflex-0030, Smooth-On) on a glass slide using a water-soluble tape (3 M) after activation by ultraviolet light for 3 min. To tightly stack the second layer of the electrode on top of the first layer, a dielectric layer (15 μm) of Ecoflex was spin-coated on the first layer. Using the same method, six layers of top stimulation electrodes were built up and aligned under the microscope. The VIAs were developed by laser ablation to route all electrodes in multiple layers to the same plane. The VCSEL array was bonded with the six-layer electrode using silver epoxy (Esolder 3022, EIS, USA). Anisotropic conductive films (Elform) were hot pressed to the front pads of the electrodes to connect the patch to the external power supply and the data acquisition system. The bottom common ground electrode was fabricated in a similar way to the top electrodes.

The structure of the ultrasonic transducer consists of a piezoelectric material and a backing layer. 1-3 PZT-5A composites (Del Piezo, USA) were selected due to their high electromechanical coupling coefficients. The condensed backing layer was made of silver epoxy (Esolder 3022, EIS, USA) for absorbing the extra ultrasonic waves. The silver epoxy composite was mixed with the hardener in a 12.5:1 ratio over 10 min and mounted on a 0.3 mm thick mold, which was then cured at 80 °C for 2 h. The same silver epoxy was used to integrate the backing layer with the 1-3 composite material, and the entire piece was diced into multiple small elements (0.8 mm length × 0.6 mm width × 1 mm thickness).

A scaffold with 240 openings was customized to fix the piezoelectric transducers. Connections to the top and bottom electrodes were achieved with the conductive adhesive at 80 °C for 2 h. The device was encapsulated by filling the device with the uncured Ecoflex precursor, followed by curing at 80 °C for 20 min. After that, the glass substrates carrying the top and bottom electrodes were peeled off. VCSEL chips and piezoelectric transducers are connected to external driving and signal acquisition systems with wires. The connection of VCSEL chips can be integrated with that of the piezoelectric transducers, which does not increase the complexity of the overall wearable patch compared to ultrasound sensors⁹⁸.

Simulation of optical distribution

The simulation of the optical intensity distribution in a 3D space was performed by the Monte Carlo method using an open-source MATLAB toolbox—MCmatlab⁹⁹. A 4 cm × 4 cm × 4 cm homogeneous

region was set as the human breast tissue, with the absorption coefficient μ_a , scattering coefficient μ_s , Henyey – Greenstein scattering anisotropy factor g , and refractive index n set as 0.1 cm⁻¹, 85 cm⁻¹ ref. 100, 0.9 ref. 99, and 1.3, respectively. The region above the top surface was considered as air, with μ_a , μ_s , g , and n set as 1×10^{-8} cm⁻¹, 1×10^{-8} cm⁻¹, 1, and 1, respectively. The laser diode array was placed at the center of the top surface. The width of each laser source was 1.5 mm. Each laser diode emitted a laser beam into the tissue perpendicular to the surface with a divergence angle of 20°. All the boundaries were set to be cuboid. The wavelength was 850 nm.

Simulation of photoacoustic detection sensitivity

The simulation of photoacoustic detection sensitivity was performed in a 4 cm × 4 cm × 4 cm homogeneous region using an open-source MATLAB toolbox — k-Wave¹⁰¹. The transducer array was placed at the center of the top surface. Assuming the background tissue as the human breast, the sound speed and tissue density were set as 1510 m s⁻¹ and 1020 kg m⁻³, respectively. The frequency dependent acoustic absorption coefficient was considered as 0.75 dB (MHz)^y cm⁻¹, where y equals to 1.5 ref. 102. The simulation region was divided into voxel elements with a pitch of 0.05 mm in each direction. In each voxel, one point source emitted a pulsed photoacoustic signal with the amplitude decided by the light distribution. All transducers received the pulse signal, followed by Delay-And-Sum beamforming. The amplitude of the beamformed signal was the detection sensitivity of this voxel.

Characterization of VCSEL array

The laser power of a single VCSEL chip is about 40 W measured by a power meter (Newport Corporation, 835 Optical Power Meter, 818-SL detector, 883-SL attenuator), which has a sensing aperture of 11.3 mm to cover the entire light beam of one VCSEL. Considering the entire patch with a footprint of 2 cm × 1.6 cm, the average power is about 1.8×10^3 W m⁻², which is lower than the safety limit¹⁰³ of 3.99×10^3 W m⁻². Smaller pulse repetition frequency can be selected to further reduce the power if needed by specific use cases. To detect the light fields of optical beams in different cases, including a single VCSEL, and an undeformed, stretched, bent, or twisted VCSEL array, we scanned a photodetector point by point in free space to measure the optical intensity in a 2D plane. An optical attenuator (Thorlabs, NE60A-B) was fixed on the photodetector (Thorlabs, PDA10A2) to make sure the optical intensity does not exceed the measurement range of the photodetector. The scanning plane was 3 cm away from the VCSEL and VCSEL array. We measured five optical fields with a size of 2 cm × 2 cm and a step size of 1 mm (Fig. S15).

Characterization of piezoelectric transducers

The transmitting sound field of a transducer element was measured using a hydrophone (ONDA, Model no. HNP-0400) in a water tank (Fig. S21). The piezoelectric transducer was excited by a pulse voltage of 100 V. A hydrophone scanning system (ONDA, AIMS III) moved the hydrophone in the 3D space. The peak-to-peak value of the signal measured by the hydrophone was extracted. To test the receiving sensitivity of the piezoelectric transducers, the performances of the photoacoustic patch and the commercial probe P4-2v from Verasonics were compared. P4-2v was chosen because it has a central frequency of about 2.7 MHz, close to the transducers (~2.4 MHz) in the photoacoustic patch. A 100 V pulse was applied to a customized single transducer (0.5 mm × 0.5 mm) to emit ultrasound waves, which was measured by both the commercial probe and the photoacoustic patch (Fig. S22). Signals measured by four elements of the photoacoustic patch were summed, which was the same as the case in the practical applications. To map the receiving sensitivity in 3D space, the single transducer ultrasound source was moved by the scanning system

(ONDA, AIMS III) to emit ultrasound waves, which was measured by the photoacoustic patch and beamformed in the Verasonics system. The peak-to-peak value of the beamformed signal was extracted (Fig. S23).

System setup and data collection

Verasonics Vantage 256 worked as the host to control the timing sequence of the whole system and signal acquisition. It has 256 individual signal acquisition channels with built-in low-noise amplifier, programmable gain amplifier and filters. That means each element receives the photoacoustic signal independently. All of the elements can receive the data simultaneously. Signals of four elements will be summed digitally in the MATLAB program to form one element in each virtual linear array. A program was written by MATLAB and run on the Verasonics system, controlling the laser radiation and photoacoustic signal acquisition.

To synchronize the laser emission and signal acquisition, Verasonics exported a 3.3 V LVTTTL-compatible trigger signal to the signal generator (Rigol, DG822), which was a 1 μ s active low output. The signal generator would be triggered to output a 5 V pulse signal with a duration of 200 ns. The laser driver (PicoLAS, LDP-V 240-100 V3.3) received the output from the signal generator, and immediately provided a 50 A current to drive the laser diodes with a pulse duration of 200 ns. The peak power of each VCSEL was 40 W driven by a 50 A pulse current. After laser illumination, the Verasonics system started the signal acquisition process. The recorded photoacoustic signal was digitized at a sampling frequency of 62.5 MHz and filtered by a bandpass filter with a center frequency of 2.2 MHz and -6 dB bandwidth of 1.2 MHz. To enhance the SNR, photoacoustic signals were averaged 3000 times to reduce the incoherent noise. Verasonics controlled the VCSELs to emit laser beams and transducers to receive signals at a pulse repetition frequency of 3 kHz, resulting in a detection frame rate of 1 Hz. A C-language program was written and called in MATLAB by the host program to reconstruct the 2D images. Reconstructing one 2D image takes about 50 ms, which means ~ 0.65 s is required to reconstruct all of the 13 slices of 2D images. These slices of 2D images can be shown during the measurement in real-time, which reveal information in 3D space. Converting the 2D images into 3D image was manually processed offline in a software (Amira) after saving all of the 2D images. The processing time took <20 s. The conversion from 2D images to 3D image may be processed automatically in MATLAB in the future to save time. The time-domain signals were also saved for offline processing to reconstruct the 3D images.

The human skin and driving electrodes that connect VCSEL diodes are isolated by a 1 mm-thick Eco-flex 00–30 layer. As reported¹⁰⁴, the leakage current for such a silicon polymer layer with the same thickness is as low as 10^{-11} A at an applied electric field of $5 \text{ V } \mu\text{m}^{-1}$. Since the applied electric field in this study is less than $1 \text{ V } \mu\text{m}^{-1}$, the leakage current should be smaller than 10^{-11} A for the photoacoustic patch, which is very safe. In the ex-vivo temperature measurements (Fig. 3f, g), to avoid direct illumination on the thermocouples (Omega Engineering Inc., Model no. SC-TT-K-30-36) by the laser beam and getting photoacoustic signals from them, the thermocouples were placed at the peripheral region of the photoacoustic patch. Supplementary Tables 4 and 5 list the detailed information of experimental equipment and material used in this study, respectively.

Image reconstruction algorithms

The Coherence-Factor-weighted-Delay-And-Sum (CFDAS) algorithm was applied to reconstruct photoacoustic images. For the unmodified DAS beamforming algorithm, assuming the photoacoustic signals are measured by a transducer array with M elements, the received signal of each channel is expressed as $p_m(t)$. To reconstruct the image $I(x, z)$ at pixel (x, z) , the wave propagation time from the pixel to the m -th element is calculated as Δt_m . Therefore, the image $I(x, z)$ could be

computed through the summation of $\sum_{m=1}^M p_m(\Delta t_m)$. The CFDAS introduces an adaptive coherence factor as an additional weight to $\sum_{m=1}^M p_m(\Delta t_m)$, which is $\text{CF} = \frac{|\sum_{m=1}^M p_m(\Delta t_m)|^2}{M \sum_{m=1}^M |p_m(\Delta t_m)|^2}$ ¹⁰⁵. CFDAS has been demonstrated to improve the image quality¹⁰⁶ (Fig. S27). The reconstructed 2D images were combined in Amira to form 3D images. The gaps between the 2D image slices were smoothed by Amira automatically.

Test of optical absorption spectra

The NIR-UV-Vis measurements were carried out through a PerkinElmer lambda 1050 UV/Vis/NIR Spectrometer. Water absorbance spectrum was measured under 150 mm InGaAs Int. Sphere Absorbance module and the rest were carried out through 3D WB Det. Absorbance Module. Before each measurement, a 100% transmittance (0 absorbance) baseline was auto-zeroed. The water spectrum was denoised through white certified reflectance standard from Labsphere Company while the rest background was calibrated with pure water. The detection cuvette had a transmittance length of 5 mm. The injected beam (Slit width of 2.00 nm) was sourced from the combination of D2 Lamp and Tungsten Lamp with a lamp change at 860.8 nm. The spectra were collected in the wavelength range from 1000 nm to 700 nm with a data interval of 1 nm.

Acquisition of ultrasound B-mode images

The ultrasound B-mode images of cyst phantoms were acquired by the Verasonics Vantage 256 with a L11-5v linear array. The center frequency of the probe was 7.8 MHz. The compounding imaging strategy was applied to reconstruct the images, which transmitted plane waves in 21 directions, received the echoes, and combined them all to form a single image.

Reporting summary

Further information on research design is available in the Nature Portfolio Reporting Summary linked to this article.

Data availability

All data supporting the findings of this study are available within the paper and its Supplementary Information. The data generated in this study are available from a public data repository at https://figshare.com/articles/dataset/PA_patch/21440925.

References

- Neri, M., Riezzo, I., Pascale, N., Pomara, C. & Turillazzi, E. Ischemia/reperfusion injury following acute myocardial infarction: a critical issue for clinicians and forensic pathologists. *Mediators Inflamm.* 2017, 7018393 (2017).
- Binks, A. & Nolan, J. Post-cardiac arrest syndrome. *Minerva Anesthesiol.* **76**, 362–368 (2010).
- Taruttis, A. et al. Optoacoustic imaging of human vasculature: feasibility by using a handheld probe. *Radiology* **281**, 256–263 (2016).
- Weigand, K. et al. Ischemia/Reperfusion injury in liver surgery and transplantation: pathophysiology. *HPB Surg.* 2012, 176723 (2012).
- Kriegelstein, C. F. et al. Role of blood- and tissue-associated inducible nitric-oxide synthase in colonic inflammation. *Am. J. Pathol.* **170**, 490–496 (2007).
- Rossaint, R. et al. Management of bleeding following major trauma: an updated European guideline. *Crit. Care* **14**, 1–29 (2010).
- Antonescu, C. Malignant vascular tumors—an update. *Mod. Pathol.* **27**, S30–S38 (2014).
- Ko, K. H., Kim, E. K. & Park, B. W. Invasive papillary carcinoma of the breast presenting as post-traumatic recurrent hemorrhagic cysts. *Yonsei Med. J.* **47**, 575–577 (2006).

9. Kitada, M. et al. Surgical treatment of intracystic carcinoma of the breast. *World J. Surg. Oncol.* **9**, 1–4 (2011).
10. Gambhir, S. S. Molecular imaging of cancer with positron emission tomography. *Nat. Rev. Cancer* **2**, 683–693 (2002).
11. Wang, L. V. & Yao, J. A practical guide to photoacoustic tomography in the life sciences. *Nat. Methods* **13**, 627–638 (2016).
12. Niu, S. M. et al. A wireless body area sensor network based on stretchable passive tags. *Nat. Electron.* **2**, 361–368 (2019).
13. Bandodkar, A. J. et al. Sweat-activated biocompatible batteries for epidermal electronic and microfluidic systems. *Nat. Electron.* **3**, 554–562 (2020).
14. Chung, H. U. et al. Skin-interfaced biosensors for advanced wireless physiological monitoring in neonatal and pediatric intensive-care units. *Nat. Med.* **26**, 418–429 (2020).
15. Kim, J., Campbell, A. S., de Avila, B. E. & Wang, J. Wearable biosensors for healthcare monitoring. *Nat. Biotechnol.* **37**, 389–406 (2019).
16. Gao, W. et al. Fully integrated wearable sensor arrays for multiplexed in situ perspiration analysis. *Nature* **529**, 509–514 (2016).
17. Sempionatto, J. R. et al. An epidermal patch for the simultaneous monitoring of haemodynamic and metabolic biomarkers. *Nat. Biomed. Eng.* **5**, 737–748 (2021).
18. Chen, Y. et al. Skin-like biosensor system via electrochemical channels for noninvasive blood glucose monitoring. *Sci. Adv.* **3**, e1701629 (2017).
19. Lin, H. et al. A programmable epidermal microfluidic valving system for wearable biofluid management and contextual biomarker analysis. *Nat. Commun.* **11**, 1–12 (2020).
20. Koh, A. et al. A soft, wearable microfluidic device for the capture, storage, and colorimetric sensing of sweat. *Sci. Transl. Med.* **8**, 366ra165 (2016).
21. Wang, Z. et al. Microneedle patch for the ultrasensitive quantification of protein biomarkers in interstitial fluid. *Nat. Biomed. Eng.* **5**, 64–76 (2021).
22. Blicharz, T. M. et al. Microneedle-based device for the one-step painless collection of capillary blood samples. *Nat. Biomed. Eng.* **2**, 151–157 (2018).
23. Yokota, T. et al. Ultraflexible organic photonic skin. *Sci. Adv.* **2**, e1501856 (2016).
24. Khan, Y. et al. A flexible organic reflectance oximeter array. *Proc. Natl Acad. Sci. U. S. A.* **115**, E11015–E11024 (2018).
25. Baca, J. T., Finegold, D. N. & Asher, S. A. Tear glucose analysis for the noninvasive detection and monitoring of diabetes mellitus. *Ocul. Surf.* **5**, 280–293 (2007).
26. Shah, J. et al. Photoacoustic imaging and temperature measurement for photothermal cancer therapy. *J. Biomed. Opt.* **13**, 034024 (2008).
27. Shi, L., Sordillo, L. A., Rodriguez-Contreras, A. & Alfano, R. Transmission in near-infrared optical windows for deep brain imaging. *J. Biophotonics* **9**, 38–43 (2016).
28. Sordillo, L. A., Pu, Y., Pratavieira, S., Budansky, Y. & Alfano, R. R. Deep optical imaging of tissue using the second and third near-infrared spectral windows. *J. Biomed. Opt.* **19**, 056004 (2014).
29. Sakr, H. et al. Hollow core optical fibres with comparable attenuation to silica fibres between 600 and 1100 nm. *Nat. Commun.* **11**, 1–10 (2020).
30. Youn, J.-S., Lee, M.-J., Park, K.-Y. & Choi, W.-Y. 10-Gb/s 850-nm CMOS OEIC receiver with a silicon avalanche photodetector. *IEEE J. Quantum Electron.* **48**, 229–236 (2011).
31. Jasim, F. Z., Omar, K. & Hassan, Z. Temperature effect on VCSEL output performance. *Optoelectron. Adv. Mat.* **3**, 1136–1138 (2009).
32. Allen, T. J. & Beard, P. C. Pulsed near-infrared laser diode excitation system for biomedical photoacoustic imaging. *Opt. Lett.* **31**, 3462–3464 (2006).
33. Upputuri, P. K. & Pramanik, M. Fast photoacoustic imaging systems using pulsed laser diodes: a review. *Biomed. Eng. Lett.* **8**, 167–181 (2018).
34. Zhong, H. et al. Enabling both time-domain and frequency-domain photoacoustic imaging by a fingertip laser diode system. *Opt. Lett.* **44**, 1988–1991 (2019).
35. Wang, C. et al. Continuous monitoring of deep-tissue haemodynamics with stretchable ultrasonic phased arrays. *Nat. Biomed. Eng.* **5**, 749–758 (2021).
36. Friedlein, J. T. et al. Dual-comb photoacoustic spectroscopy. *Nat. Commun.* **11**, 1–10 (2020).
37. Telenkov, S. & Mandelis, A. Signal-to-noise analysis of biomedical photoacoustic measurements in time and frequency domains. *Rev. Sci. Instrum.* **81**, 124901 (2010).
38. Lengenfelder, B. et al. Remote photoacoustic sensing using speckle-analysis. *Sci. Rep.* **9**, 1–11 (2019).
39. Wang, Y. et al. In vivo three-dimensional photoacoustic imaging based on a clinical matrix array ultrasound probe. *J. Biomed. Opt.* **17**, 061208 (2012).
40. Hariri, A. et al. The characterization of an economic and portable LED-based photoacoustic imaging system to facilitate molecular imaging. *Photoacoustics* **9**, 10–20 (2018).
41. Cebrecos, A. et al. Beamforming for large-area scan and improved SNR in array-based photoacoustic microscopy. *Ultrasonics* **111**, 106317 (2021).
42. Deán-Ben, X. L., López-Schier, H. & Razansky, D. Photoacoustic micro-tomography at 100 volumes per second. *Sci. Rep.* **7**, 1–8 (2017).
43. Wang, Y., Zhan, Y., Harris, L. M., Khan, S. & Xia, J. A portable three-dimensional photoacoustic tomography system for imaging of chronic foot ulcers. *Quant. Imag. Med. Surg.* **9**, 799 (2019).
44. Cheshire, W. P. Jr Thermoregulatory disorders and illness related to heat and cold stress. *Auton. Neurosci.* **196**, 91–104 (2016).
45. Coiffard, B., Diallo, A. B., Mezouar, S., Leone, M. & Mege, J. L. A tangled threesome: circadian rhythm, body temperature variations, and the immune system. *Biology* **10**, 65 (2021).
46. Glazer, J. L. Management of heatstroke and heat exhaustion. *Am. Fam. Physician* **71**, 2133–2140 (2005).
47. Pozos, R. S. & Danzl, D. Human physiological responses to cold stress and hypothermia. in: *Medical Aspects of Harsh Environments*, eds K. Pandolf and R. Burr (Washington: Borden Institute), 351–382 (2001).
48. Pasquier, M. et al. Deep accidental hypothermia with core temperature below 24 °C presenting with vital signs. *High. Alt. Med. Biol.* **15**, 58–63 (2014).
49. Jardine, D. S. Heat illness and heat stroke. *Pediatr. Rev.* **28**, 249–258 (2007).
50. Eshraghi, Y. et al. An evaluation of a zero-heat-flux cutaneous thermometer in cardiac surgical patients. *Anesth. Analg.* **119**, 543–549 (2014).
51. Pesonen, E. et al. The focus of temperature monitoring with zero-heat-flux technology (3M Bair-Hugger): a clinical study with patients undergoing craniotomy. *J. Clin. Monit. Comput.* **33**, 917–923 (2019).
52. Huang, M., Tamura, T., Tang, Z., Chen, W. & Kanaya, S. A wearable thermometry for core body temperature measurement and its experimental verification. *IEEE J. Biomed. Health Inform.* **21**, 708–714 (2017).
53. Kitamura, K. I., Zhu, X., Chen, W. X. & Nemoto, T. Development of a new method for the noninvasive measurement of deep body temperature without a heater. *Med. Eng. Phys.* **32**, 1–6 (2010).
54. Wang, L. V. & Hu, S. Photoacoustic tomography: in vivo imaging from organelles to organs. *Science* **335**, 1458–1462 (2012).
55. Castillo, M. & Marino, T. The core curriculum, ultrasound. *Academic Radiol.* **9**, 729–730 (2002).

56. Li, Y. L., Hyun, D., Abou-Elkacem, L., Willmann, J. K. & Dahl, J. J. Visualization of small-diameter vessels by reduction of incoherent reverberation with coherent flow power doppler. *IEEE Trans. Ultrason. Ferroelectr. Freq. Control* **63**, 1878–1889 (2016).
57. Jeong, J. W. et al. Capacitive epidermal electronics for electrically safe, long-term electrophysiological measurements. *Adv. Healthc. Mater.* **3**, 642–648 (2014).
58. Jeong, J. W. et al. Materials and optimized designs for human-machine interfaces via epidermal electronics. *Adv. Mater.* **25**, 6839–6846 (2013).
59. Wang, Y. et al. Electrically compensated, tattoo-like electrodes for epidermal electrophysiology at scale. *Sci. Adv.* **6**, eabd0996 (2020).
60. Wilkinson, I. B. & Webb, D. J. Venous occlusion plethysmography in cardiovascular research: methodology and clinical applications. *Br. J. Clin. Pharm.* **52**, 631–646 (2001).
61. Kamshilin, A. A., Zaytsev, V. V. & Mamontov, O. V. Novel contactless approach for assessment of venous occlusion plethysmography by video recordings at the green illumination. *Sci. Rep.* **7**, 464 (2017).
62. Wang, Y. et al. Assessment of brain functional activity using a miniaturized head-mounted scanning photoacoustic imaging system in awake and freely moving rats. *Biosensors* **11**, 429 (2021).
63. Yang, J. et al. Photoacoustic imaging of hemodynamic changes in forearm skeletal muscle during cuff occlusion. *Biomed. Opt. Express* **11**, 4560–4570 (2020).
64. Manwar, R., Zafar, M. & Xu, Q. Signal and image processing in biomedical photoacoustic imaging: a review. *Optics* **2**, 1–24 (2021).
65. Singh, M. K. A, Sato, N, Ichihashi, F & Sankai, Y. LED-Based Photoacoustic Imaging. Vol. 10, 978–981 (Springer: 2020).
66. Kim, J. et al. Real-time photoacoustic thermometry combined with clinical ultrasound imaging and high-intensity focused ultrasound. *IEEE Trans. Biomed. Eng.* **66**, 3330–3338 (2019).
67. Landa, F. J. O., Dean-Ben, X. L., Sroka, R. & Razansky, D. Volumetric optoacoustic temperature mapping in photothermal therapy. *Sci. Rep.* **7**, 9695 (2017).
68. Zhang, H. F., Maslov, K., Stoica, G. & Wang, L. V. Functional photoacoustic microscopy for high-resolution and noninvasive in vivo imaging. *Nat. Biotechnol.* **24**, 848–851 (2006).
69. Kim, H. S., Nguyen, V., Bom, H. S. & Min, J. J. In vivo imaging of hemoglobin and melanin variations using photoacoustic tomography. *J. Nucl. Med.* **56**, 1206 (2015).
70. Sim, J. Y., Ahn, C. G., Jeong, E. J. & Kim, B. K. In vivo microscopic photoacoustic spectroscopy for non-invasive glucose monitoring. *Invisible to Skin Secretion Products. Sci. Rep.* **8**, 1059 (2018).
71. Dasa, M. K., Markos, C., Janting, J. & Bang, O. Multispectral photoacoustic sensing for accurate glucose monitoring using a supercontinuum laser. *J. Opt. Soc. Am. B* **36**, A61–A65 (2019).
72. Pleitez, M. A. et al. In vivo noninvasive monitoring of glucose concentration in human epidermis by mid-infrared pulsed photoacoustic spectroscopy. *Anal. Chem.* **85**, 1013–1020 (2013).
73. Cao, Y. et al. Fast assessment of lipid content in arteries in vivo by intravascular photoacoustic tomography. *Sci. Rep.* **8**, 2400 (2018).
74. Buma, T., Conley, N. C. & Choi, S. W. Multispectral photoacoustic microscopy of lipids using a pulsed supercontinuum laser. *Biomed. Opt. Express* **9**, 276–288 (2018).
75. Zhang, C., Zhang, Y. S., Yao, D. K., Xia, Y. & Wang, L. V. Label-free photoacoustic microscopy of cytochromes. *J. Biomed. Opt.* **18**, 20504 (2013).
76. Shi, J. et al. High-resolution, high-contrast mid-infrared imaging of fresh biological samples with ultraviolet-localized photoacoustic microscopy. *Nat. Photonics* **13**, 609–615 (2019).
77. Li, L. et al. Small near-infrared photochromic protein for photoacoustic multi-contrast imaging and detection of protein interactions in vivo. *Nat. Commun.* **9**, 2734 (2018).
78. Mishra, K., Fuenzalida-Werner, J. P., Ntziachristos, V. & Stiel, A. C. Photocontrollable proteins for optoacoustic imaging. *Anal. Chem.* **91**, 5470–5477 (2019).
79. De La Zerda, A. et al. Carbon nanotubes as photoacoustic molecular imaging agents in living mice. *Nat. Nanotechnol.* **3**, 557–562 (2008).
80. Chen, Y.-S., Zhao, Y., Yoon, S. J., Gambhir, S. S. & Emelianov, S. Miniature gold nanorods for photoacoustic molecular imaging in the second near-infrared optical window. *Nat. Nanotechnol.* **14**, 465–472 (2019).
81. Ashkenazi, S. Photoacoustic lifetime imaging of dissolved oxygen using methylene blue. *J. Biomed. Opt.* **15**, 040501 (2010).
82. Weber, J., Beard, P. C. & Bohndiek, S. E. Contrast agents for molecular photoacoustic imaging. *Nat. Methods* **13**, 639–650 (2016).
83. Kuramoto, M. et al. Watt-class blue vertical-cavity surface-emitting laser arrays. *Appl. Phys. Express* **12**, 091004 (2019).
84. Qiao, P., Cook, K. T., Li, K. & Chang-Hasnain, C. J. Wavelength-swept VCSELs. *IEEE J. Sel. Top. Quantum Electron.* **23**, 1700516 (2017).
85. Mitchell, C. et al. Guidelines for performing a comprehensive transthoracic echocardiographic examination in adults: recommendations from the American Society of Echocardiography. *J. Am. Soc. Echocardiogr.* **32**, 1–64 (2019).
86. Rahko, P. S. Evaluation of the skin-to-heart distance in the standing adult by two-dimensional echocardiography. *J. Am. Soc. Echocardiogr.* **21**, 761–764 (2008).
87. Zhou, Y. et al. Thermal memory based photoacoustic imaging of temperature. *Optica* **6**, 198–205 (2019).
88. Mienkina, M. P. et al. Multispectral photoacoustic coded excitation imaging using unipolar orthogonal Golay codes. *Opt. Express* **18**, 9076–9087 (2010).
89. Su, S.-Y. & Li, P.-C. Coded excitation for photoacoustic imaging using a high-speed diode laser. *Opt. Express* **19**, 1174–1182 (2011).
90. Mienkina, M. P. et al. Experimental evaluation of photoacoustic coded excitation using unipolar golay codes. *IEEE Trans. Ultrason. Ferroelectr. Freq. Control* **57**, 1583–1593 (2010).
91. Zhang, H. K., Kondo, K., Yamakawa, M. & Shiina, T. Coded excitation using periodic and unipolar M-sequences for photoacoustic imaging and flow measurement. *Opt. Express* **24**, 17–29 (2016).
92. Zhou, M., Xia, H., Zhong, H., Zhang, J. & Gao, F. A noise reduction method for photoacoustic imaging in vivo based on EMD and conditional mutual information. *IEEE Photonics J.* **11**, 1–10 (2019).
93. Sun, M., Feng, N., Shen, Y., Shen, X. & Li, J. Photoacoustic signals denoising based on empirical mode decomposition and energy-window method. *Adv. Adapt. Data Anal.* **4**, 1250004 (2012).
94. Donoho, D. L. & Johnstone, J. M. Ideal spatial adaptation by wavelet shrinkage. *biometrika* **81**, 425–455 (1994).
95. Zhou, M. et al. Wavelet de-noising method with adaptive threshold selection for photoacoustic tomography. In *Proc. 40th Annual International Conference on Engineering in Medicine and Biology Society*, 4796–4799 (2018).
96. Van de Sompel, D., Sasportas, L. S., Jokerst, J. V. & Gambhir, S. S. Comparison of deconvolution filters for photoacoustic tomography. *PLoS One* **11**, e0152597 (2016).
97. Manwar, R. et al. Photoacoustic signal enhancement: towards utilization of low energy laser diodes in real-time photoacoustic imaging. *Sensors* **18**, 3498 (2018).
98. Hu, H. et al. Stretchable ultrasonic transducer arrays for three-dimensional imaging on complex surfaces. *Sci. Adv.* **4**, eaar3979 (2018).
99. Marti, D., Aasbjerg, R. N., Andersen, P. E. & Hansen, A. K. MCmatlab: an open-source, user-friendly, MATLAB-integrated three-dimensional Monte Carlo light transport solver with heat diffusion and tissue damage. *J. Biomed. Opt.* **23**, 121622 (2018).

100. Schmitt, J. M. & Kumar, G. Optical scattering properties of soft tissue: a discrete particle model. *Appl. Opt.* **37**, 2788–2797 (1998).
 101. Treeby, B. E. & Cox, B. T. k-Wave: MATLAB toolbox for the simulation and reconstruction of photoacoustic wave fields. *J. Biomed. Opt.* **15**, 021314 (2010).
 102. Treeby, B. E. & Cox, B. T. Modeling power law absorption and dispersion for acoustic propagation using the fractional Laplacian. *J. Acoust. Soc. Am.* **127**, 2741–2748 (2010).
 103. Standard ANSI Z136. 1. American National Standard for the Safe Use of Lasers. American National Standards Institute Inc., New York (1993).
 104. Vaicekauskaite, J., Mazurek, P., Vudayagiri, S. & Skov, A. L. Mapping the mechanical and electrical properties of commercial silicone elastomer formulations for stretchable transducers. *J. Mater. Chem. C*. **8**, 1273–1279 (2020).
 105. Park, S., Karpouk, A. B., Aglyamov, S. R. & Emelianov, S. Y. Adaptive beamforming for photoacoustic imaging. *Opt. Lett.* **33**, 1291–1293 (2008).
 106. Liao, C. K., Li, M. L. & Li, P. C. Optoacoustic imaging with synthetic aperture focusing and coherence weighting. *Opt. Lett.* **29**, 2506–2508 (2004).
- performed the experiments. X.G. and Z.L. performed data processing. X.G., X.J.C., H.J.H., R.Z., and S.X. wrote the paper. K.S., X.C., M.Y.L., and B.Q. helped with phantom preparation. S.Z., C.L., and Y.G. provided suggestions on device design and fabrication. X.Y., H.D., Y.Z., H.H., Y.M., M.L., A.M., and J.W. provided advice on data analysis. All authors provided constructive and valuable feedback on the manuscript.

Competing interests

The authors declare no competing interests.

Additional information

Supplementary information The online version contains supplementary material available at <https://doi.org/10.1038/s41467-022-35455-3>.

Correspondence and requests for materials should be addressed to Sheng Xu.

Peer review information *Nature Communications* thanks Fei Gao, Benjamin Tee and the other, anonymous, reviewer(s) for their contribution to the peer review of this work.

Reprints and permissions information is available at <http://www.nature.com/reprints>

Publisher's note Springer Nature remains neutral with regard to jurisdictional claims in published maps and institutional affiliations.

Open Access This article is licensed under a Creative Commons Attribution 4.0 International License, which permits use, sharing, adaptation, distribution and reproduction in any medium or format, as long as you give appropriate credit to the original author(s) and the source, provide a link to the Creative Commons license, and indicate if changes were made. The images or other third party material in this article are included in the article's Creative Commons license, unless indicated otherwise in a credit line to the material. If material is not included in the article's Creative Commons license and your intended use is not permitted by statutory regulation or exceeds the permitted use, you will need to obtain permission directly from the copyright holder. To view a copy of this license, visit <http://creativecommons.org/licenses/by/4.0/>.

© The Author(s) 2022

Acknowledgements

The authors thank Z. Wu for the guidance on the ultrasonic imaging algorithm and data processing, L. Yin for discussions on the laser diode fabrication, D. Yount for discussions on the wire bonding, Y. Chen and Y. Lei for discussions on the ultrasound transducer fabrication, Z. Chen for discussions on data processing, and S. Xiang for the feedback on manuscript preparation. The material is partially based on research sponsored by Air Force Research Laboratory under agreement number FA8650-18-2-5402 (S.X.). The U.S. Government is authorized to reproduce and distribute reprints for Government purposes notwithstanding any copyright notation thereon. The views and conclusions contained herein are those of the authors and should not be interpreted as necessarily representing the official policies or endorsements, either expressed or implied, of Air Force Research Laboratory (AFRL) or the U.S. Government. This work was partially supported by the National Institutes of Health grants 1R21EB025521-01 (S.X.), 1R21EB027303-01A1 (S.X.), and 3R21EB027303-02S1 (S.X.).

Author contributions

X.G., X.J.C., H.J.H., and S.X. designed the research. X.G., X.J.C., H.J.H., X.W., W.Y., and J.M. fabricated the device. X.G., X.J.C., W.Y., and R.Z.

Supplementary Information for

A photoacoustic patch for three-dimensional imaging of hemoglobin and core temperature

Xiaoxiang Gao^{1,†}, Xiangjun Chen^{2,†}, Hongjie Hu^{1,†}, Xinyu Wang¹, Wentong Yue¹, Jing Mu², Zhiyuan Lou¹, Ruiqi Zhang¹, Keren Shi², Xue Chen², Muyang Lin¹, Baiyan Qi², Sai Zhou², Chengchangfeng Lu³, Yue Gu², Xinyi Yang², Hong Ding¹, Yangzhi Zhu¹, Hao Huang¹, Yuxiang Ma¹, Mohan Li¹, Aditya Mishra², Joseph Wang^{1,2}, Sheng Xu^{1,2,3,4,5,*}

1. Department of Nanoengineering, University of California San Diego, La Jolla, CA 92093, USA

2. Materials Science and Engineering Program, University of California San Diego, La Jolla, CA 92093, USA.

3. Department of Electrical and Computer Engineering, University of California San Diego, La Jolla, CA, USA.

4. Department of Radiology, School of Medicine, University of California San Diego, La Jolla, CA 92093, USA.

5. Department of Bioengineering, University of California San Diego, La Jolla 92093, CA, USA.

†These authors contributed equally to this work.

*Corresponding author. E-mail: shengxu@ucsd.edu

Supplementary Note 1 | Comparison between different biomolecular imaging methods

Conventionally, there are several non-invasive methods for detecting biomolecules with high penetration depth (>10 cm) such as magnetic resonance imaging (MRI)^{1,2} and positron emission tomography (PET)^{3,4}. MRI leverages the different magnetic properties of various biomolecules to generate images. More specifically, those biomolecules possess multiple relaxation times after receiving radiofrequency pulses. PET is based on the detection of two annihilation photons, which are generated by collisions of the injected radioactive tracers and electrons within the tissue. The tracers will only couple with the target molecules so that high contrast will be achieved. However, the existence of radioactive tracers prevents this technique from long-term use. For these two methods, the associated equipment is too cumbersome and expensive, thus impossible for wearable long-term health monitoring.

Several optical methods are used for biomolecular imaging. The principle of fluorescence imaging is that materials will emit fluorescent light at a specific wavelength after absorbing high energy photons. Different molecules possessing various molecular energy structures result in various fluorescence. Although the spatial resolution is high (~4 μm), this technique is highly limited by its shallow penetration depth (~3 mm)⁵. Optical coherence tomography (OCT) typically uses near-infrared light for imaging. The backscattered light is measured with an interferometric setup to reconstruct the depth profile of the tissue⁶. But the penetration depth is still limited (~2 mm)⁷.

Photoacoustic imaging involves shining a laser beam onto tissues. After that, the light energy is absorbed by the biomolecules and converted to mechanical vibration energy, i.e., photoacoustic waves. Photoacoustic imaging entails several advantages⁸ compared to the aforementioned optical

imaging: (1) by illuminating various molecules at different wavelengths, photoacoustic tomography exhibits high contrasts regarding chemical compositions; (2) the spatial information of biomolecules is encoded in the ultrasound waves, which has relatively weak attenuation in biological tissues. Therefore, photoacoustic imaging can achieve high spatial resolution (tens of micrometers) mapping of biomolecules in deep tissues (several centimeters in depth)^{9,10}. As of now, existing photoacoustic imaging devices are bulky and cumbersome, not suitable for wearable long-term continuous use.

The emergence of wearable devices such as soft electrochemical electronics¹¹ and soft optoelectronics¹² makes continuous monitoring possible. Nevertheless, these devices are still limited by the shallow detection depth beneath the skin. Additionally, these devices can only provide measurements at specific locations, lacking spatial resolutions.

The soft photoacoustic patch in this work inherits the merits of photoacoustic imaging, which is biomolecular selectivity and high imaging resolution in deep tissues. Also, the flexible and stretchable configuration allows the device to be conformally attached to the skin, which can potentially enable convenient and continuous measurements on the go. By innovative designs in device layout and advanced data processing methods of the soft photoacoustic patch, we achieved a detection depth >2 cm with high spatial resolution in biological tissues.

Supplementary Note 2 | Innovation of the photoacoustic patch in the fields of soft electronics and photoacoustic imaging

The innovation of this work can be summarized as the following points. In soft electronics, we developed the flexible and stretchable electronic patch that can noninvasively detect and image molecules in deep tissues. Skin-like wearable patches that integrate various kinds of sensors can monitor the health and wellness of the human body. Existing skin-like wearable patches can sense biomolecules in sweat¹³⁻¹⁵, saliva^{16,17}, and tears¹⁸⁻²⁰ on the skin surface, or interstitial fluids with micro needles^{21,22}. But none of the existing patches have access to those biomolecules embedded deeply underneath the skin (>1 cm). Importantly, those biomolecules in deep tissues should have a stronger and faster correlation to the dynamic processes inside the human body^{23,24}. The wearable photoacoustic patch reported in this work adds an extra sensing dimension for chemical signals in the human body using soft electronics. Furthermore, our wearable patch can map and monitor core temperature in deep tissues with high accuracy and quick response. In existing literatures, core temperature can only be detected by an invasive catheter^{25,26} or by heat-flux-model-based wearable temperature sensors^{27,28}. However, the latter methods have slow response speed (about several hundreds of seconds) and lack capability of temperature mapping.

In photoacoustic imaging, we developed the low form factor photoacoustic patch. Conventional photoacoustic imaging systems use a laser source to generate ultrasound waves in tissues, and ultrasound transducers to receive photoacoustic waves. Laser equipment is always very bulky and heavy, not suitable for wearing. Safety regulations also require the operation of lasers by professionals. Even though some reported studies introduced the applications of laser diodes²⁹⁻³² or LEDs^{33,34} as laser sources, nobody reported using vertical cavity surface emitting laser (VCSEL) bare dies, which have small thickness, ~200 micrometers, and are thus challenging to be integrated on the soft electronic platform. Furthermore, all the reported photoacoustic studies utilize bulky

ultrasound transducers to receive photoacoustic waves. Our work introduced a flexible and stretchable ultrasound transducer array as the sensing components. This work develops a flexible and stretchable photoacoustic patch by redesigning and fabricating both the laser source and ultrasound transducer elements. This work makes photoacoustic imaging possible for long-term monitoring even in freely moving subjects.

In summary, we developed a flexible and stretchable photoacoustic patch that can image molecules in deep tissues. This patch can map and monitor the core temperature in deep tissues with high accuracy and quick response. This patch is also innovative in terms of the laser source and ultrasound sensing elements of photoacoustic imaging systems, all in low form factors. None of these advances have been reported by our group or any other groups in the world.

Supplementary Note 3 | Comparison between different photoacoustic imaging systems

For a photoacoustic imaging system, the key sensing components are (1) laser sources for exciting the target molecules to generate photoacoustic waves and (2) piezoelectric transducers for detecting acoustic waves. Conventionally, the optical sources used in the photoacoustic system can be divided into three categories. The first type is the conventional high-power laser system, whose peak pulse power is usually on the order of millijoule^{35,36}, with a penetration depth spanning from 3 mm to 4 cm⁹. These high-power lasers are mostly used to provide strong light intensity to excite the target molecules to generate photoacoustic waves. Operating these lasers needs strict training and to be in laboratories that meet high safety standards. Additionally, these laser systems are costly and bulky, which are not suitable for wearable applications. The second type is the hand-held compact laser with a relatively lower energy than the first type. A typical laser of this kind

has a size as small as $160\text{ mm} \times 64\text{ mm} \times 40\text{ mm}$ ³⁷. Still, they are too large to be suitable for continuous wearing. The third type is light-emitting diodes or laser diodes. Although some photoacoustic systems employ light-emitting diodes and laser diodes as the optical source, they still rely on bulky rigid ultrasound probes to receive the acoustic waves^{29,38}. Those ultrasound probes require manual holding and the subject to be static during testing. Additionally, they use edge-emitting semiconductor laser diodes, which are not suitable to be integrated into a conformal patch because the edge-emitting semiconductor laser diodes usually have a large size (more than several millimeters) in the emission direction²⁹.

The photoacoustic patch in this work integrates both the laser source and the piezoelectric transducer into a low form factor conformal patch ($20\text{ mm} \times 16\text{ mm} \times 1.2\text{ mm}$), by encapsulating an array of laser diode chips ($1.7\text{ mm} \times 2.4\text{ mm} \times 0.4\text{ mm}$) and transducer elements ($0.6\text{ mm} \times 0.8\text{ mm} \times 1.0\text{ mm}$) into a flexible and stretchable silicone polymer matrix. In terms of the complexity of the system, we have significantly simplified a conventional photoacoustic imaging system by replacing the bulky laser source with surface-mounted laser diode dies. Although the VCSEL chips (<\$10 each) may increase the cost compared to an ultrasound patch, it greatly reduces the cost of conventionally used laser sources. In addition, the cost of each VCSEL die chip can further be reduced if the quantity of chips is increased. The stretchability of the overall patch is enabled by the serpentine shaped metal electrodes that interconnect the laser diode chips and the transducer elements. The device is rigid locally at the laser diode chips and the transducer elements but is soft globally on the system level. The penetration depth of this soft photoacoustic patch in tissues can reach >2 cm. The technology is potentially suitable for wearable health monitoring without immobilizing the test subjects.

To develop a fully integrated wearable system in the future, handling the quantity of data needs to be solved. Different clinical cases require different quantities of continuous imaging for clinical application. The monitoring period extends from several minutes to several days. Assuming each 2D image has a size of $2\text{ cm} \times 2\text{ cm}$, composed of 200×200 pixels, one 2D image would occupy $\sim 39\text{ KB}$ for 1-byte unsigned integer data type. Thus, 13 slices will be $\sim 507\text{ KB}$. To be specific, continuous monitoring for 5 minutes, 5 hours, or 5 days will create datasets with the size of about 149 MB, 8.7 GB, and 209 GB, respectively. Such file sizes are easy to be accommodated since common commercial hard disks have space larger than several Terabytes. To handle these data for a completely portable system, a solution is to transfer the image data from the portable system to an external data storage equipment, which can be easily achieved by USB 2.0 cables (data transfer speed $> 60\text{ MB s}^{-1}$) or WiFi (data transfer speed $> 2.5\text{ MB s}^{-1}$).

It is worth mentioning that the big difference of optical intensity between high power lasers and laser diode chips may have influence on the detection of non-static tissues. Because the high-power laser has very strong light intensity, it can generate strong photoacoustic signals with only one pulse. Pulsation of the tissues (e.g., major arteries) will not affect the imaging result. However, for laser diode chip based photoacoustic systems, the light intensity and therefore photoacoustic signals are relatively weak. Averaging several thousands of signals are required to increase the signal-to-noise ratio. Acquiring several thousands of signals may take one second or even a longer time, during which the photoacoustic signal will move forward and back due to movements of the tissue, resulting in unstable phases of the photoacoustic signals, and thus destroying the coherent

averaging (Fig. S46)³⁹. Therefore, compensation of motion will be required to achieve a good averaging result for artery imaging⁴⁰.

Supplementary Note 4 | Summary of first, second, and third optical windows

Near-infrared light has high penetration depth in human tissues compared to the visible light because of its weak scattering and absorption⁴¹. For probing human tissues, three commonly used optical windows are in the range of 650 ~ 950 nm, 1000 ~ 1350 nm, and 1600 ~ 1870 nm⁴². In the first window, hemoglobin still has a higher optical absorption than water and lipid. Therefore, photoacoustic signals of hemoglobin can be generated with low background noise. No extra contrast agent is needed to highlight the hemoglobin. In the second window, the penetration depth increases. But additional contrast agents are needed to label the hemoglobin molecules because of their low absorption coefficients⁴³⁻⁴⁵. The third window has even deeper penetration because of reduced scattering, but is rarely used due to the dominant water absorption⁴⁶, suppressing the detection of other molecules.

Supplementary Note 5 | Comparison between different temperature measurement methods

The gold standard for measuring the core temperature is to use a catheter to measure the temperature in the pulmonary artery⁴⁷, which is too invasive for routine measurements. Implantable devices with biocompatibility can be directly fixed in the human body, thus providing accurate and continuous temperature measurements in deep tissues^{48,49}. However, in a lot of cases, the infection risks, application complexity, data communication, and power supplies of the implantable devices introduce more challenges than benefits.

There are various strategies for noninvasive temperature measurements of the human body. Wearable skin-like soft sensors usually integrate temperature sensitive electronic components, such as the thermistor⁵⁰, the ion conductor⁵¹, and the thermocouple⁵². But they can only measure the temperature on the skin surface. Magnetic resonance imaging can quantify the internal temperature variance at a depth >10 cm and spatial resolution of 2 mm⁵³. However, owing to the bulky and expensive system, it is not realistic to use MRI in daily activities.

Wearable sensors that can measure core temperatures are developed mostly based on the zero-heat-flux model⁵⁴ and the dual-heat-flux model^{55,56}. In the zero-heat-flux model, when the skin and deep tissue temperatures are considered identical, there will be no heat flow between them. As a result, the core temperature is the same as the skin surface temperature^{57,58}. Nevertheless, these sensors require external heaters to achieve a thermal equilibrium between the skin surface and the core body and thus have a relatively long response time (>180 s)⁵⁸, especially at a considerable depth underneath the skin. To eliminate the use of the heater, sensors based on the dual heat flux model are developed²⁷. But this method requires an even longer response time (~447 s)²⁷ and it is imprecise since it is only a predicted value.

Compared to the existing methods, the photoacoustic patch has multiple advantages, including high penetration depth (>2 cm on tissues), short response time (~1 s), and soft mechanical design for continuous wearing.

Supplementary Note 6 | Mechanism of temperature sensing by the photoacoustic patch

Generating photoacoustic waves is a process of converting optical energy to mechanical vibration energy. After the laser illumination, biomolecules (e.g., hemoglobin in this work) will absorb the optical energy, undergo thermoelastic expansion, and radiate acoustic waves into the surrounding media. For a nanosecond laser source, the generation of photoacoustic waves satisfies the stress and thermal confinements⁵⁹. The photoacoustic signal amplitude can be express as:⁶⁰

$$P = \Gamma \mu_a F \quad (1)$$

where Γ is the Grüneisen parameter, μ_a is the absorption coefficient, and F is the laser fluence. During the test, the light fluence F is a constant for the same laser source. μ_a also keeps unchanged for the same type of biomolecule. The Grüneisen parameter is what changes the signal amplitude, and linear to the temperature in the range of 10 ~ 55 °C⁵⁹⁻⁶¹. Therefore, the photoacoustic signal and the temperature show a linear relationship in the vicinity of human core temperature (~37 °C). The Grüneisen parameter Γ can be expressed as:

$$\Gamma = \Gamma_0 + \alpha T \quad (2)$$

where Γ_0 is the value at temperature T_0 , α is a constant decided by the tissue type. The photoacoustic signal amplitude can be rewritten as:⁶²

$$P = (\Gamma_0 + \alpha T) \mu_a F = \alpha \mu_a F T + \Gamma_0 \mu_a F \quad (3)$$

The photoacoustic signal can quantify the temperature after calibrating $\alpha\mu_a F$ and $\Gamma_0\mu_a F$, which can be considered as the slope and intercept of a linear function, respectively.

Pure ultrasound techniques can also noninvasively measure the temperature in deep tissue because the tissue temperature will change the sound speed. However, there are some limitations for temperature measurements with ultrasound. First, the biggest problem is that ultrasonography can only detect the contrast of acoustic impedance, which means ultrasound collects anatomical information. As ultrasonography cannot distinguish different biomolecules, it cannot recognize the inclusion components inside cysts, which is critical for determining if the cyst is benign or malignant. Second, ultrasonography may suffer from low contrast to recognize small blood vessels. Photoacoustic imaging, as a promising biomedical imaging technique, has made a lot of advances in the last two decades⁸. Since the photoacoustic signal originates from the light absorption, photoacoustic imaging holds optical contrast, rather than the acoustic impedance contrast. In addition, photoacoustic imaging combines the best of two worlds: generating signal optically and sensing signal acoustically, which makes photoacoustic imaging best for high-resolution high-contrast imaging of biomolecules in deep tissues. Third, for temperature sensing, ultrasound has a much lower sensitivity than photoacoustics. A quantitative comparison between these two methods has been described. For instance, assuming the temperature of water increases from 20 to 30 °C, the sound speed will increase from ~1481 to ~1507 m s⁻¹⁶³, with a relative change of sound speed only ~0.176% per degree centigrade. On the other side, the photoacoustic signal amplitude will be enhanced by 51% for such a 10 °C increase, resulting in a relatively large amplitude change of ~5.1% per degree centigrade⁶⁰.

Supplementary Note 7 | Bland-Altman analysis

Bland-Altman plot analyzes the agreement between a pair of datasets. This plot is widely used in statistics in analytical chemistry as well as biomedicine⁶⁴ to compare a new measurement method with the gold standard⁶⁵⁻⁶⁷. Assuming the datasets measured by the two methods are X and Y, the y-coordinate of the Bland-Altman plot are the differences in each paired X and Y values, while the x-coordinate represents the average value of X and Y. In Bland-Altman plot, there are three horizontal lines, representing the mean bias \bar{d} , the upper limit of agreement E_{upper} and the lower limit of agreement E_{lower} . They are defined as follows:

$$\bar{d} = \frac{1}{n} \sum_{i=1}^n (Y_i - X_i) \quad (4)$$

$$E_{upper} = \bar{d} - 1.96 \times sd \quad (5)$$

$$E_{lower} = \bar{d} + 1.96 \times sd \quad (6)$$

where sd is the standard deviation. 1.96 is the boundary of the 95-confidence interval in standard normal distribution. It means that the probability of the population mean value is between -1.96 and 1.96 standard deviations.

Supplementary Note 8 | Characterization of the skin curvature on the imaging performance

To examine the influence of irregular human neck curvature on the imaging performance of the soft photoacoustic patch, the skin curvature distribution was characterized. We used a 3D scanner (HDI Advances, LMI Technologies, Vancouver, Canada) to scan the area above the internal

jugular vein (Fig. S44a). The 3D skin surface morphology was reconstructed with high spatial resolution in the software, which was then imported into Catia software (Dassault Systèmes, France) for curvature extraction. Accurate spatial positions of the skin could be read in the Catia. We acquired 26 typical 1D skin curves by placing 26 planes, with a spacing of 1 mm, vertical to the skin and extracting the intersection line between the planes and the skin surface (Fig. S44b). Then, the skin curvatures were calculated by circle fitting⁶⁸ (Fig. S44c). All of the extracted curvatures are shown in Fig. S44d. The smallest curvature radius is 6.5 cm, which corresponds to the largest deviation from an ultrasound array on a planar surface. The raw irregular skin curves were then used to decide the positions of irregularly distributed ultrasound transducer elements.

To quantify the influence of the skin curvature on the imaging performance, the generation process of the photoacoustic signals was then simulated in a MATLAB toolbox — k-Wave⁶⁹. Seven equally distributed point sources were set at the depth of 5, 7.5, 10, 12.5, 15, 17.5, and 20 mm in human tissues. The ultrasound array of a 2 MHz center frequency was placed at the depth of 0 mm. The spatial mesh in each direction was set to be 0.05 mm, much smaller than the ultrasound wavelength of 0.77 mm to ensure high accuracy. The sampling frequency was 62.5 MHz, the same as the experimental setup. The background media was considered as breast tissues. The sound speed and tissue density were set as 1510 m s^{-1} and 1020 kg m^{-3} , respectively. The frequency dependent acoustic absorption coefficient was considered as $0.75 \text{ dB (MHz}^y \cdot \text{cm)}^{-1}$, where y equals to 1.5. The Coherence Factor weighted Delay And Sum algorithm was applied to reconstruct the photoacoustic images, with the ultrasound array set as a planar and a curvilinear array. Figure S45a shows the imaging results of the two scenarios side by side. The axial and lateral resolutions for the two scenarios are extracted and displayed in Figs. S45b-S45c. The results show that the average

axial and lateral resolutions are only reduced by 0.06 mm and 0.24 mm, respectively, when the transducer array moves from a planar geometry to a curved geometry without phase correction. Therefore, the irregular skin curvature had a negligible influence on the imaging performance of the soft photoacoustic patch. The reason for this negligible influence is that the working frequency of the photoacoustic patch is ~2 MHz, which is relatively low. The skin curvature radius is not small enough to produce an adverse effect for the long acoustic wavelength in this study.

Supplementary Note 9 | Feasibility of photoacoustic imaging on the detection of different biomolecules

The continuous detection of melanin could have potential applications in close monitoring metastasis of melanoma tumor cells⁷⁰. In addition, melanoma has a very high possibility of metastasis, which causes more than 90% cancer related mortality⁷¹. Detection and monitoring of metastasis of melanoma tumor cells can help staging the cancer and take effective means of medical intervention at the early stage. Continuous monitoring of circulating melanoma tumor cells has been well studied^{70,72,73}. Photothermal therapy has also been used to kill circulating tumors with the assistance of continuous photoacoustic imaging⁷³.

For the detection of glucose⁷⁴⁻⁷⁶, cytochromes^{77,78} and nucleic acid, many studies have actually demonstrated both *in-vitro* and *in-vivo* label-free imaging using photoacoustic techniques. But for now, photoacoustic imaging is not mature as a reliable technique to continuously monitor humans due to technical and regulatory challenges.

As for exogenous contrast agents, one typical example is indocyanine green (ICG), which has been approved by Food and Drug Administration due to its high biosafety⁷⁹. ICG was not only widely used in photoacoustic imaging studies, but also well established in clinical applications in the field of other optical imaging technique⁸⁰. Specifically for photoacoustic imaging, ICG has been used in the vena mediana cubiti of the right arm of a human volunteer to enhance the monitoring of blood haemodynamics in the finger⁸¹. In a much more comprehensive study, metastatic status of sentinel lymph nodes in melanoma has been detected with the administration of ICG in 20 patients⁸². The latter study demonstrates that patients can benefit from ICG-assisted photoacoustic imaging for clinical management of melanoma.

Supplementary Note 10 | Comparison of laser pulse repetition rates between different photoacoustic tomography imaging systems

Traditional photoacoustic tomography (PAT) imaging systems usually use expensive high-power lasers as the light source, such as Q-switched Nd:YAG or dye lasers⁸³. They usually have a pulse energy ranging from tens of millijoules to several joules and a pulse repetition rate of around 10-100 Hz^{9,70,84-90}. One laser shot can deliver sufficient light energy to generate a strong photoacoustic signal with a high signal-to-noise ratio (SNR). Therefore, without the need of data averaging, traditional PAT systems can have an imaging frame rate around 0.5~100 Hz.

However, for small-size low-cost PAT systems, expensive bulky lasers are replaced by compact inexpensive laser diodes or even light emitting diodes (LEDs)^{31,38,91-94}. These light sources typically have a pulse energy from several microjoules to a few hundreds of microjoules. The laser energy per pulse is not strong enough to generate a measurable photoacoustic signal with an

acceptable SNR. Therefore, the data averaging scheme is required to improve the SNR by averaging photoacoustic signals generated by multiple laser shots. Usually, the number of averaging ranges from tens to several thousands, depending on the laser energy. To ensure a high imaging frame rate, a high pulse repetition rate is necessary for the laser diodes or LEDs to achieve the multiple data acquisition, typically in a range from several hundreds of Hz to tens of kHz. In fact, 3 kHz is a typical pulse repetition rate compared with other low-cost PAT systems.

In summary, we need to perform data averaging to improve the SNR because the laser pulse energy is low for laser diodes compared to conventional high-power lasers. To ensure a high imaging frame rate, we need to emit laser pulses at a high pulse repetition rate accordingly. For example, we need to average 3000 times of photoacoustic signals to improve the SNR. Therefore, to ensure an imaging frame rate of about 1 Hz, we have to emit 3000 laser pulses per second.

Supplementary Note 11 | Alternative denoising methods for improving signal-to-noise ratio

In this work, we adopted data averaging and bandpass filter to improve the signal-to-noise ratio (SNR) of photoacoustic signals. The bandpass filter is to eliminate the noise outside the bandwidth of the ultrasound transducers. But thousands of times of averaging makes it time consuming, causing more laser exposure. There are other methods for SNR enhancement while requiring less time consumption, as discussed in the following.

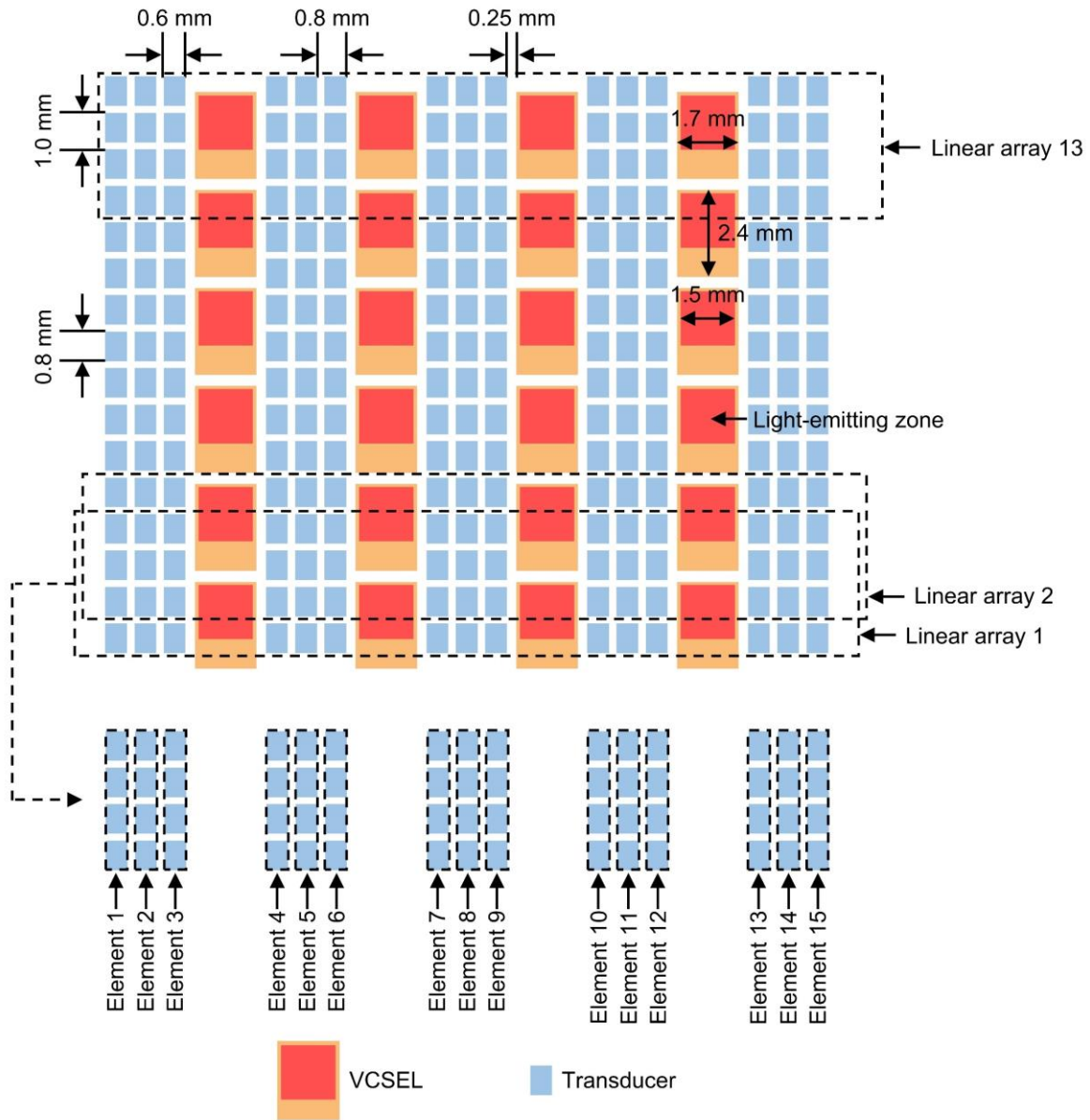
From the hardware perspective, some studies developed code excitation technique⁹⁵⁻⁹⁸ to compensate for the low optical energy of laser diodes. Laser diode drivers control the diodes to emit light pulses at a specific sequence. The photoacoustic signal is then acquired by passing

through a match filter, which is the so-called decoding. The laser diode drivers usually require a high pulse repetition frequency to satisfy the code excitation. Although the data acquisition time of the data averaging method can also be reduced by using a high pulse repetition frequency, the code excitation scheme consumes even less time^{95,97} to achieve the same SNR as data averaging.

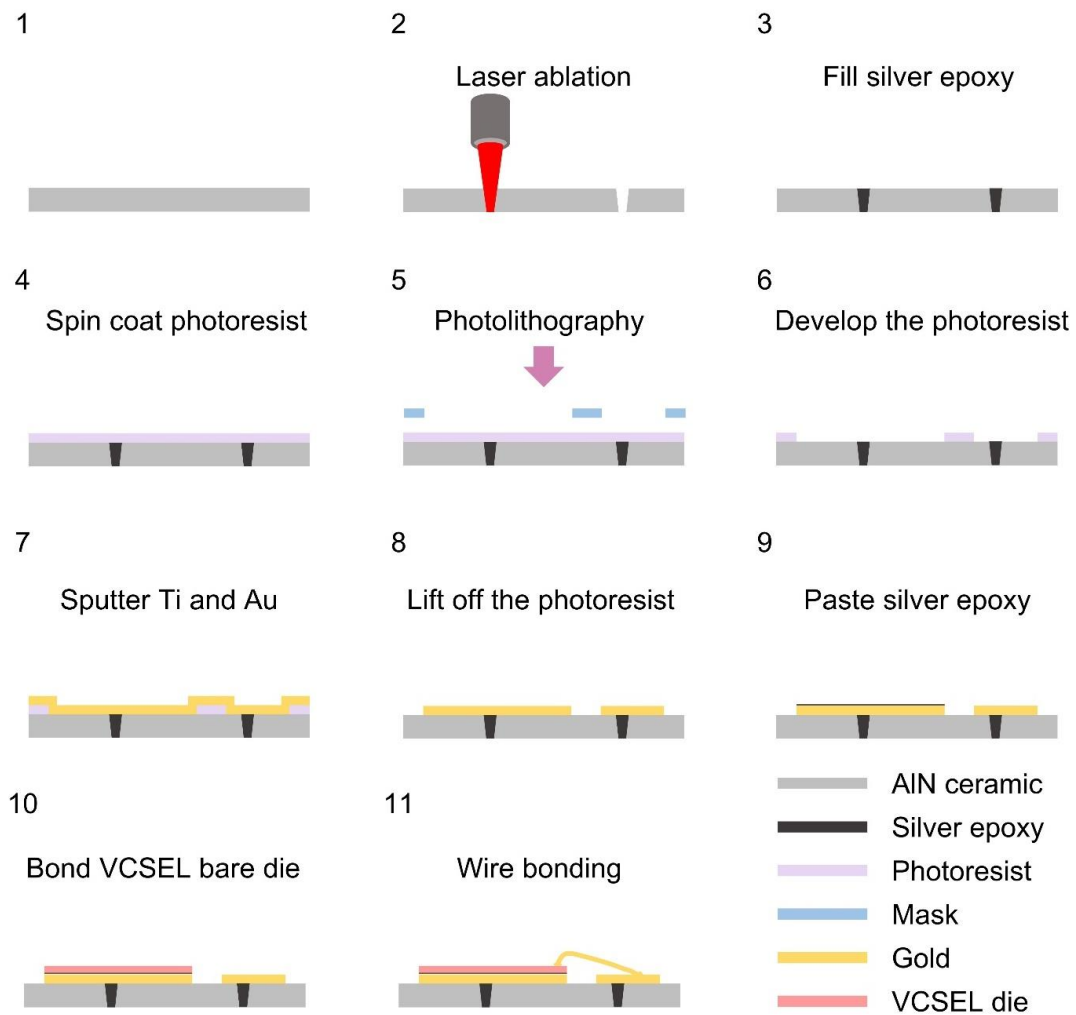
From the signal processing perspective, there are also many denoising algorithms to improve the SNR of temporal photoacoustic signals. Typical methods include empirical mode decomposition^{99,100}, wavelet thresholding^{101,102}, Wiener deconvolution¹⁰³, and adaptive filtering¹⁰⁴. Empirical mode decomposition adaptively decomposes the photoacoustic signal into a number of intrinsic mode functions, some of which represent clean photoacoustic signals and some belong to noise. Removing the intrinsic mode functions corresponding to noise based on some criteria, such as mutual information minimization⁹⁹ and energy window¹⁰⁰, will eliminate the noise in photoacoustic signals. Wavelet thresholding decomposes the signal into several basis functions with their own coefficients¹⁰¹. Small coefficients with the corresponding basis functions are considered as noise. Discarding the small coefficients based on hard or soft thresholding rules¹⁰¹ and recombining the left basis functions with large coefficients form denoised photoacoustic signals. Wiener deconvolution models the power spectrum density of clean photoacoustic signals and additive noise. Photoacoustic signals are denoised by minimizing the expected mean squared error between the measured and clean photoacoustic signals¹⁰³. An adaptive filtering algorithm assumes that there is at least one uncorrelated component between the measured and time-shifted photoacoustic signals¹⁰⁴. This adaptive noise cancelling method does not require the prior knowledge of clean signals or noise, compared to conventional adaptive noise filters. All these denoising algorithms can be applied to the photoacoustic signals generated by one laser shot,

consuming less time than multiple data acquisition for the data averaging method. But their performance relies on the selection of specific parameters, such as the reserved number of intrinsic mode functions in empirical mode decomposition, threshold in the wavelet thresholding denoising, correlation estimation between the signal and noise in Wiener deconvolution, and time delay for adaptive filtering¹⁰⁴. The data averaging method and these denoising algorithms can be adopted together to achieve better SNR⁹⁹.

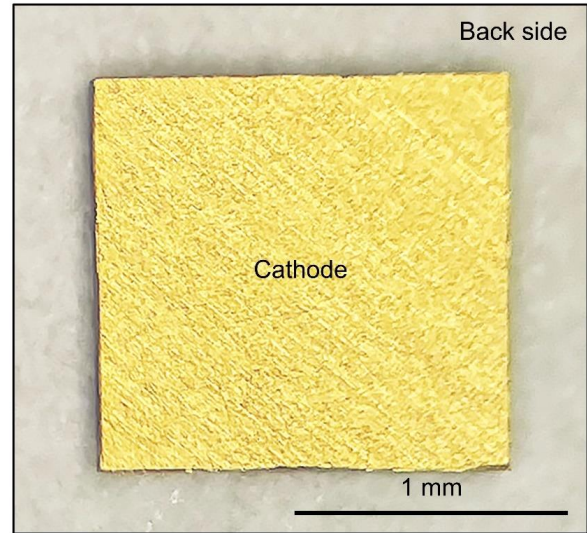
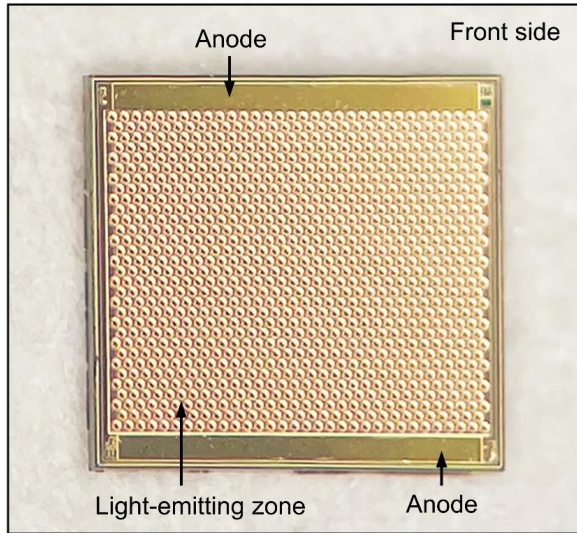
Supplementary Figures



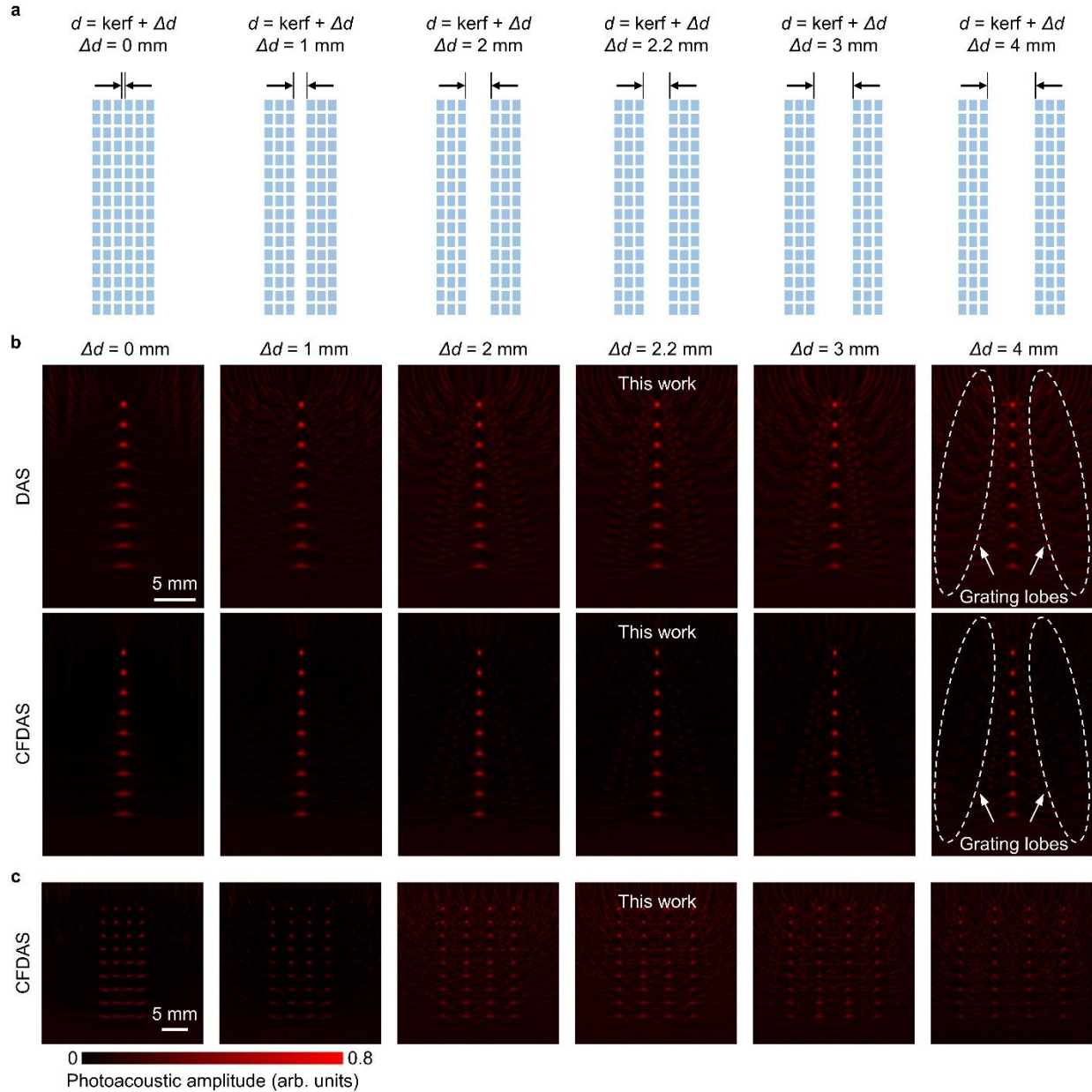
Supplementary Figure 1 | Layout design of the soft photoacoustic patch. The sizes of the laser diodes and the transducers, as well as the spacing between them, are labeled. In data processing, signals of four adjacent elements in the column are summed, digitally connected in parallel to enhance the signal amplitude. Therefore, the 16 rows of transducers form 13 linear arrays during the signal processing. In the column direction, we arrange as many VCSELs as possible to improve the optical energy intensity. In the row direction, we pack as many piezoelectric transducers as possible between VCSELs to improve the image quality. VCSEL: vertical-cavity surface-emitting laser.



Supplementary Figure 2 | Fabrication processes of integrating the VCSEL bare die on an AlN substrate. The anode and cathode of the VCSEL bare die are on the top and bottom surfaces, respectively. We fabricate two vertical interconnect accesses in the AlN substrate and bond the VCSEL bare die by wire bonding and conductive adhesives. Then both the cathode and anode are on the bottom surface, which is readily for bonding with the serpentine Cu electrodes. VCSEL: vertical-cavity surface-emitting laser. AlN: aluminum nitride. Ti: titanium. Au: gold.

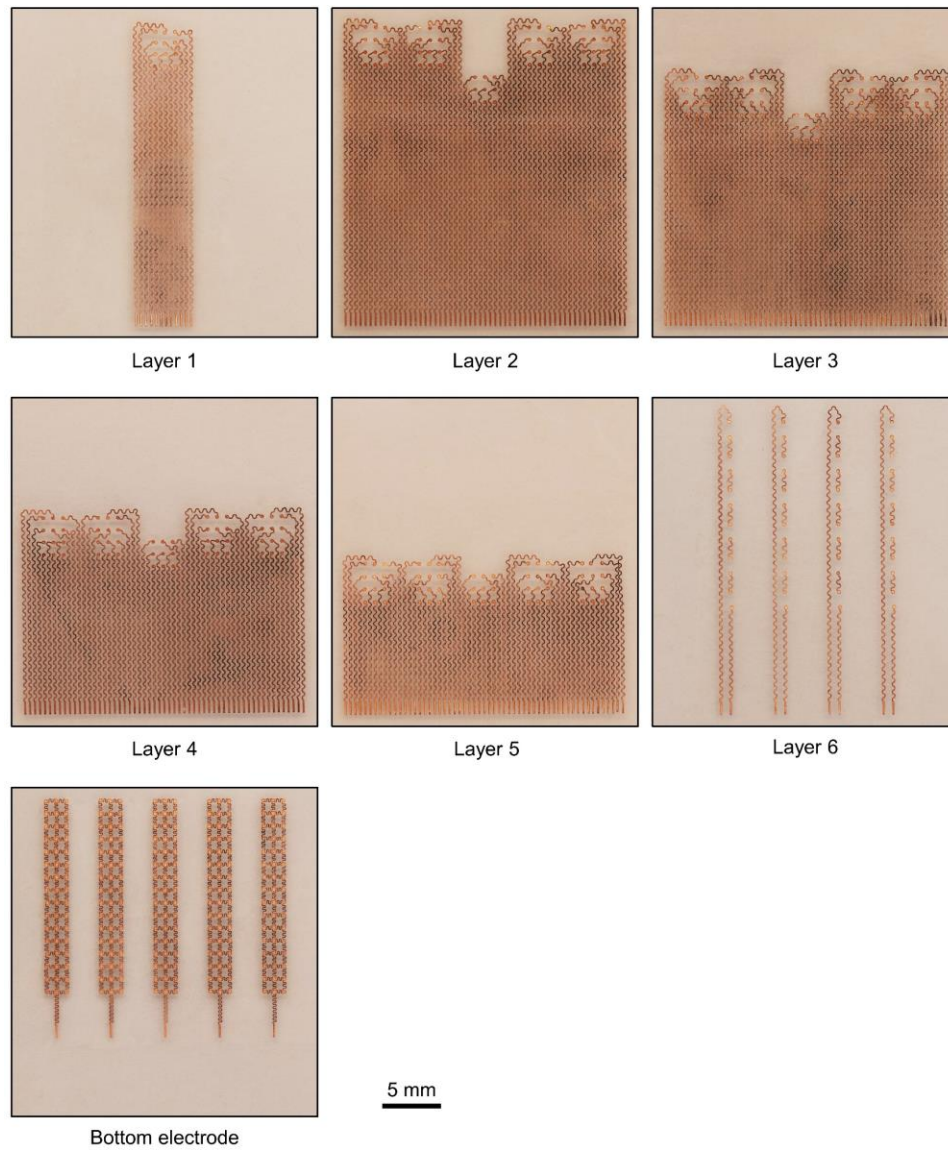


Supplementary Figure 3 | Optical photographs of the front and back sides of a VCSEL bare die. Key components of the bare die are labeled.

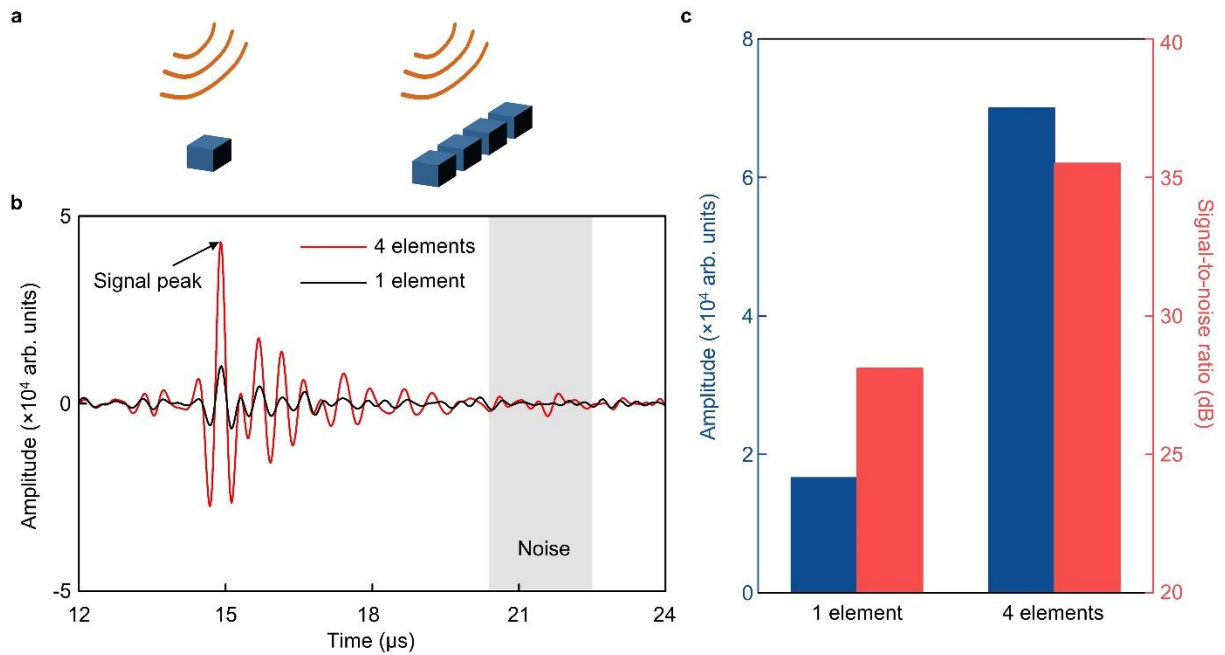


Supplementary Figure 4 | Influence of VCSEL distribution on the imaging performance. a, Schematics show how VCSEL chip increases the distance between transducers. Δd is defined as the extra distance caused by VCSEL chips between every three columns of ultrasound transducers. **b,** Simulation results show reconstructed images corresponding to different cases of Δd . Unmodified Delay-And-Sum (DAS) algorithm and Coherence-Factor-weighted-Delay-And-Sum (CFDAS) algorithm were applied to reconstruct images, respectively. When Δd equals to 0, the ultrasound transducer array has a uniform pitch between all elements. As the placement of VCSEL chips become sparser, i.e., Δd gets larger, stronger grating lobes are induced. However, the displacement of VCSEL chips also extends the aperture of the linear array, which improves the lateral resolution of photoacoustic images. Therefore, in comparison to the uniformly distributed ultrasound transducer array, VCSEL chips introduce weak grating lobes, but improve the lateral imaging resolution. For the unmodified DAS beamforming algorithm, assuming the photoacoustic signals are measured by a transducer array with M elements, the received signal of each channel

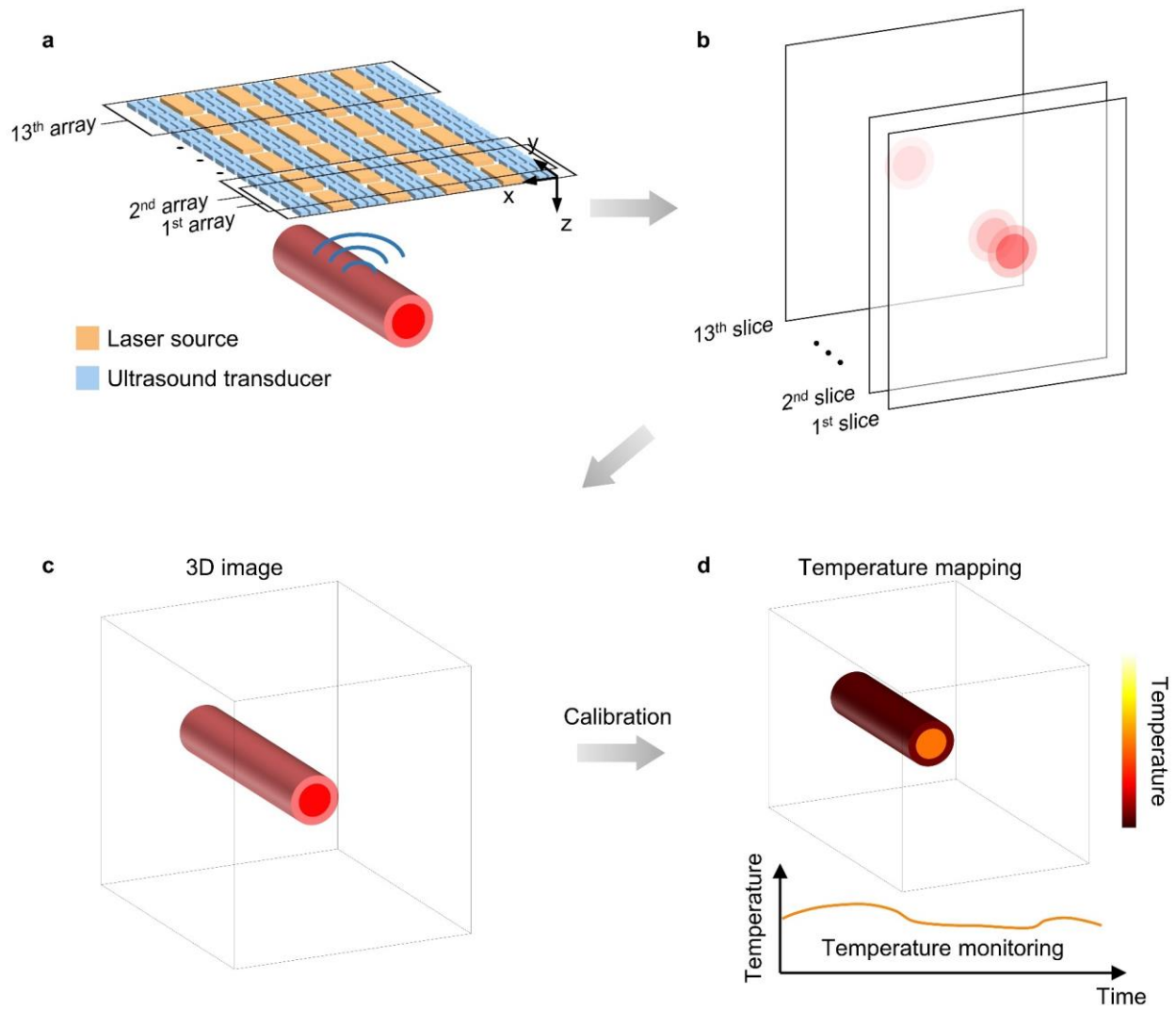
is $p_m(t)$. To reconstruct the image $I(x, z)$ at pixel (x, z) , the wave propagation time from the pixel to the m -th element is Δt_m . Therefore, the image $I(x, z)$ could be computed through the summation of $\sum_{m=1}^M p_m(\Delta t_m)$. In the results of applying DAS to beamforming, the grating lobes become larger as Δd increases caused by VCSELS, which degrades images. Therefore, we utilize CFDAS to compensate for this effect. CFDAS introduces an adaptive coherence factor as an additional weight to $\sum_{m=1}^M p_m(\Delta t_m)$, which is $CF = \frac{|\sum_{m=1}^M p_m(\Delta t_m)|^2}{M \cdot \sum_{m=1}^M |p_m(\Delta t_m)|^2}$. Both in ultrasound B-mode imaging¹⁰⁵ and photoacoustic imaging^{106,107}, the coherence factor weighted DAS beamforming has been demonstrated to suppress the grating lobes. The second row of images show the CFDAS algorithm decreases the impact of grating lobes. **c**, Images of points targets right underneath the VCSELS reconstructed with CFDAS algorithm. All the images share the same color map, ranging from 0 to 0.8. The images of all targets under the VCSEL have high axial and lateral resolutions, which are only slightly affected by the increased Δd . Furthermore, the intensities of the targets only decrease slightly.



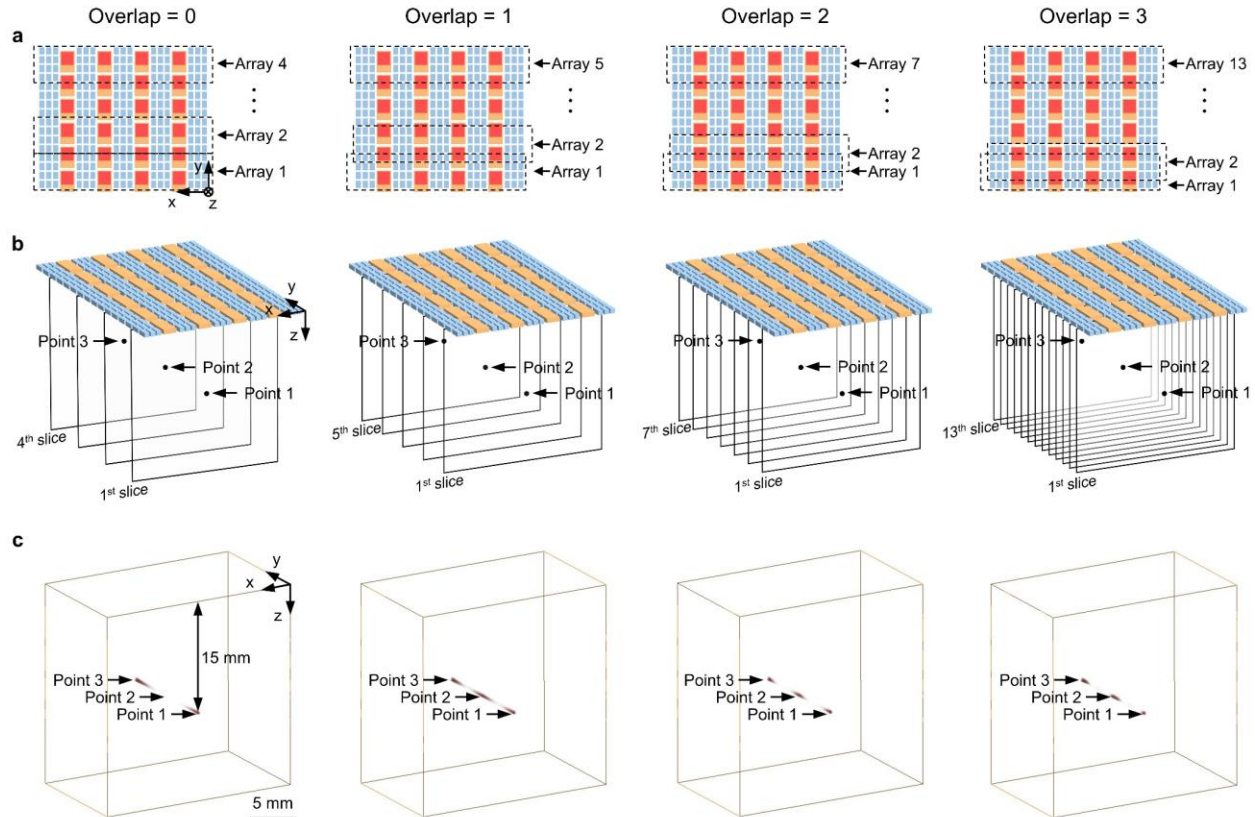
Supplementary Figure 5 | Optical photographs of all the seven layers of Cu electrodes. The first six layers form the top electrodes, among which layer 6 is for the VCSELs, while others are for the piezoelectric transducers. The bottom electrode is the common ground for all the transducers.



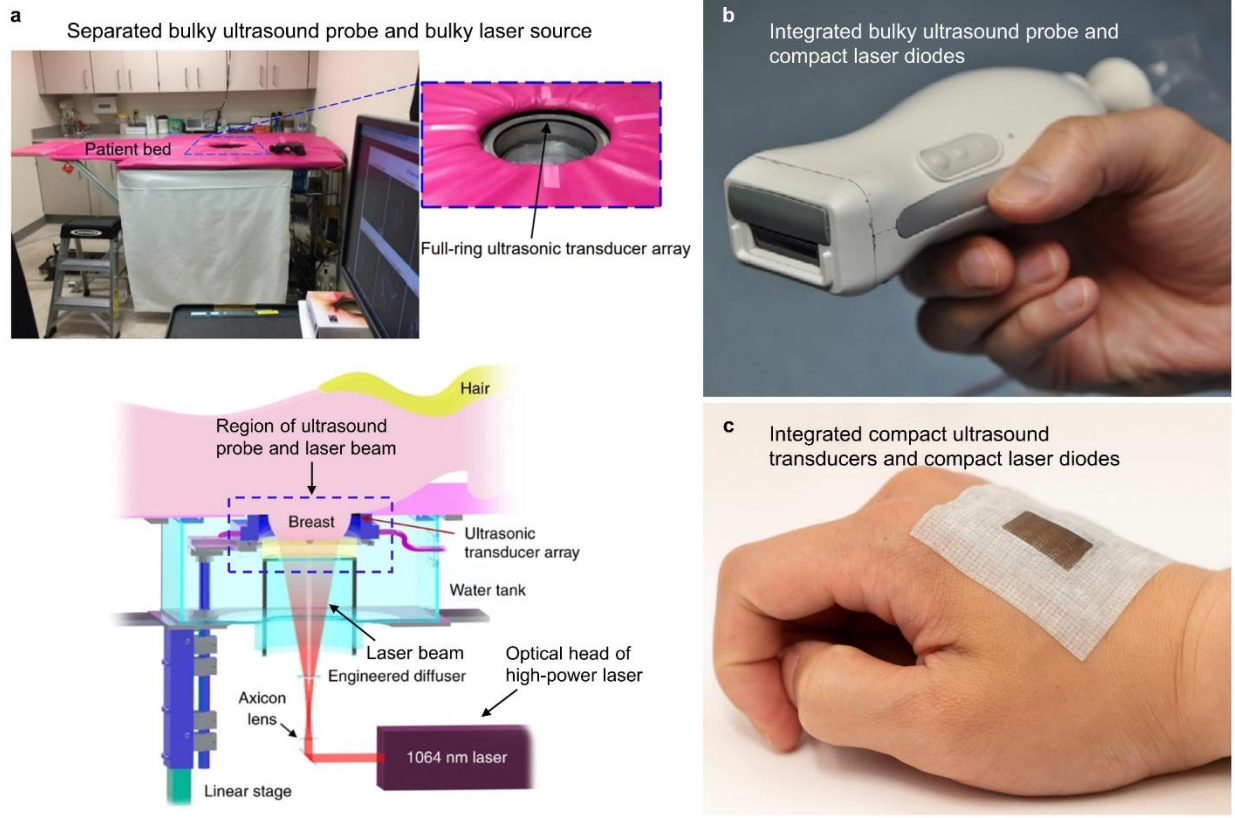
Supplementary Figure 6 | Performance comparison between one element and four parallelly connected elements. **a**, Schematics of the two measurement strategies. **b**, The time domain photoacoustic signals received by one element and four elements. **c**, Comparison of signal amplitudes and signal-to-noise ratios between one element and four elements. Signal-to-noise ratio is defined as $20\log_{10}(\text{Peak photoacoustic signal}/\text{Root mean squared error of noise})^{108-110}$.



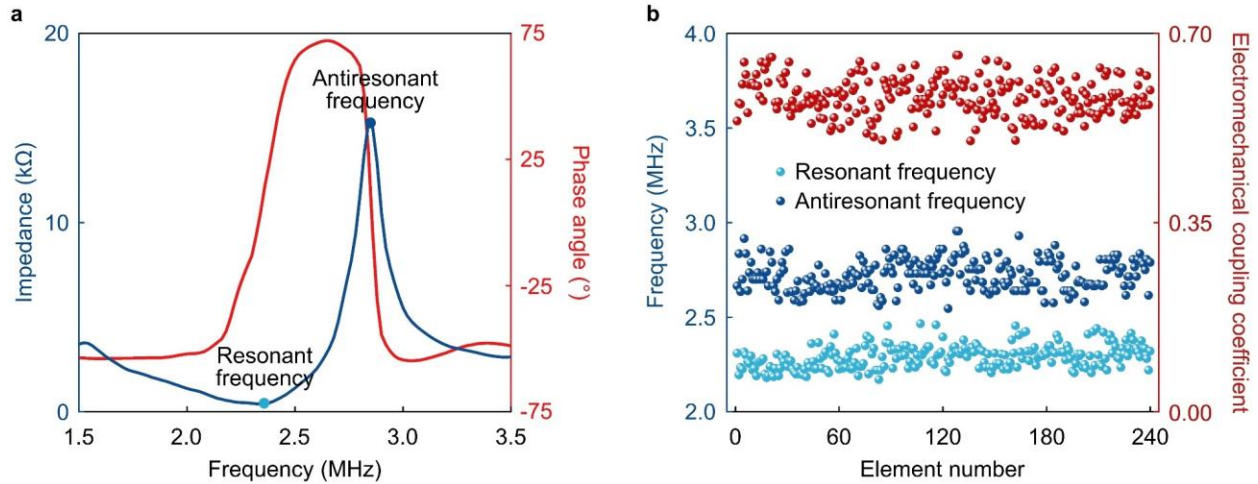
Supplementary Figure 7 | Workflow of the photoacoustic patch. **a**, Signals received by four elements in the y direction are summed to enhance the signal-to-noise ratio. 13 linear arrays in total are formed equivalently. **b**, 13 slices of 2D images are reconstructed by the patch. **c**, A 3D image is formed based on the 13 slices of 2D images. **d**, After calibration, 3D temperature mapping is achieved, which is the basis for the continuous core temperature monitoring.



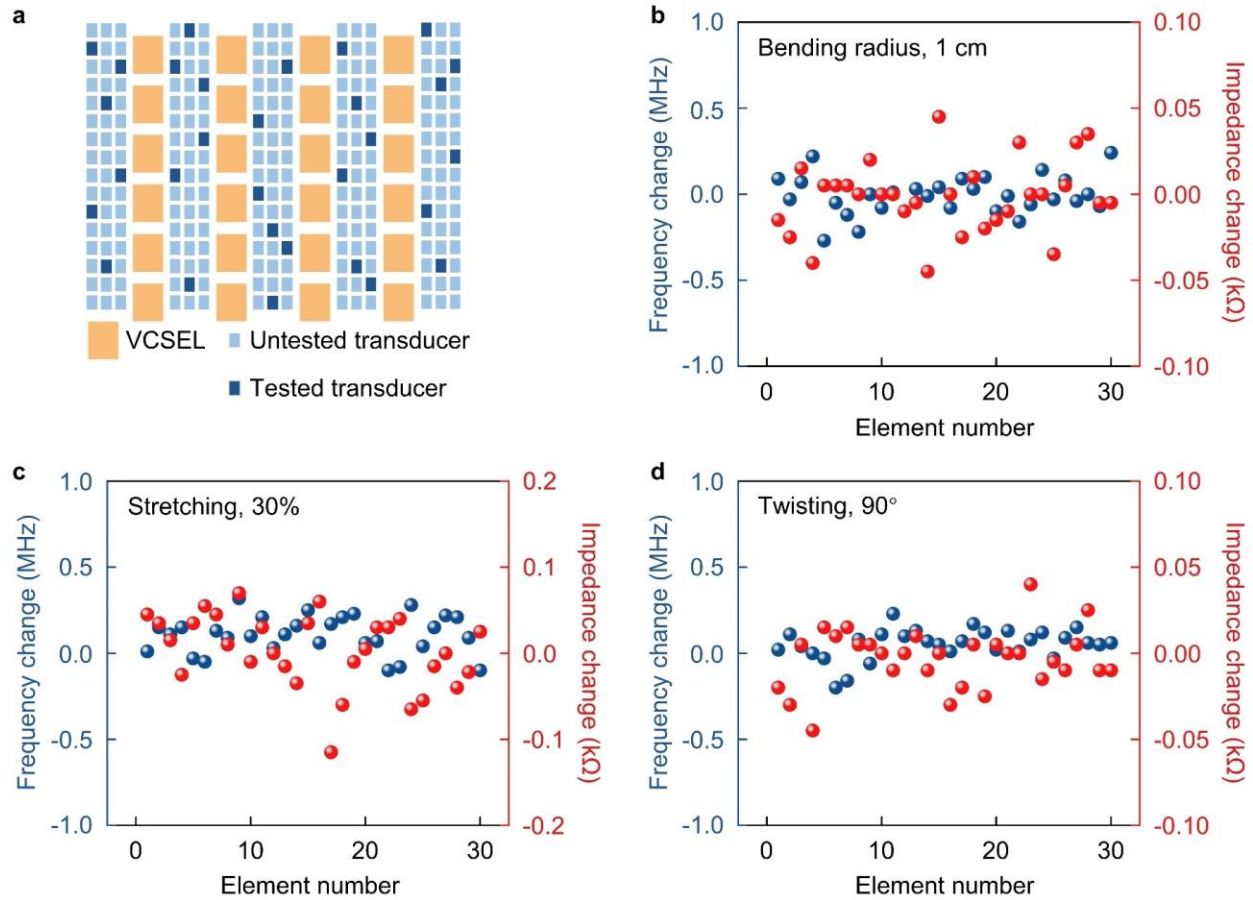
Supplementary Figure 8 | Influence of overlap of ultrasound transducers. **a**, Schematics showing four cases with the different numbers of overlapped transducers between adjacent linear arrays. **b**, Imaging planes corresponding to different setups. Three uniformly distributed point sources were set at the depth of 1.5 cm. **c**, Reconstructed 3D images for different cases. Because of the overlap between adjacent arrays, we can have a large number of linear arrays, which increases the number of 2D images in the y direction. The 3D images show that when there is no overlap, we only have four 2D images. Not all the point sources can be recognized in the 3D image. As the overlap increases, the number of 2D images increases. All points sources are captured. Furthermore, the width of the points in the y direction decreases as the overlapping increases, which means the lateral resolution in the y direction is improved. In summary, increasing the number of overlapped transducers increases the number of 2D images, improving the lateral resolution in the y direction.



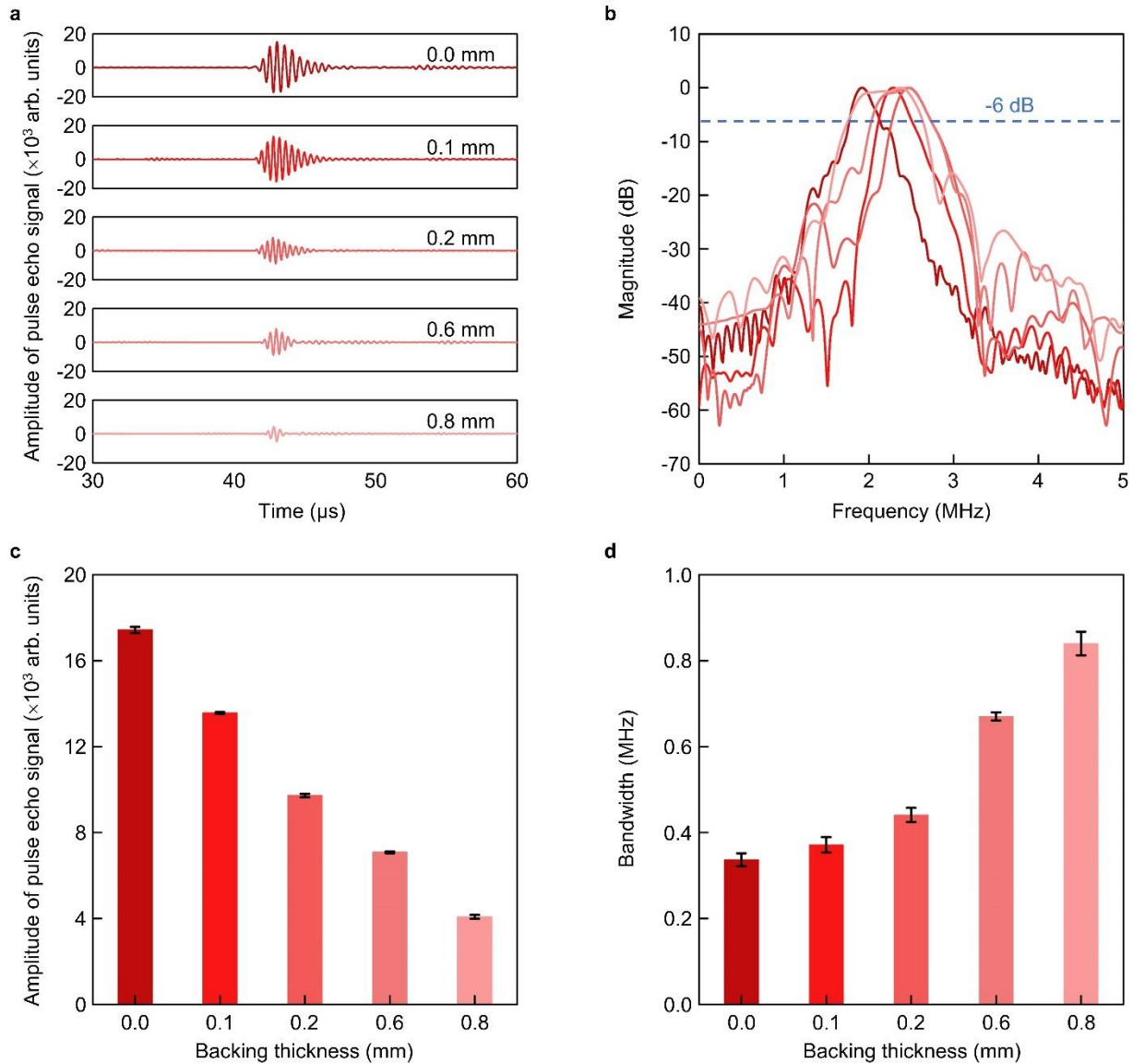
Supplementary Figure 9 | Three typical photoacoustic tomography imaging systems. a, Conventional PAT system using bulky ultrasound transducers and expensive bulky high-power lasers⁹. This PAT system has the largest size because the ultrasound probe and the laser are both bulky, immovable, and physically separated. The laser beam is usually guided by optical fibers or lens to illuminate human tissues. The size of the laser is usually over tens of centimeters. The image is adapted from REF⁹, which is licensed under a Creative Commons Attribution 4.0 International License (<http://creativecommons.org/licenses/by/4.0/>). We added several labels to illustrate the equipment. **b,** Alternatively, a low-cost photoacoustic probe integrating a traditional bulky ultrasound probe and compact laser diodes³². The laser diodes are installed in the ultrasound probe and only need to be connected with an external compact laser diode driver. The integrated photoacoustic probe is handheld and movable. This PAT system reduces the size of the whole system because the laser diodes have much smaller size compared to conventional high-power lasers. The image is copied from REF³², which is licensed under the CC BY-NC-ND license (<https://creativecommons.org/licenses/by-nc-nd/4.0/>). No changes were made. **c,** Wearable photoacoustic patch integrating low form-factor ultrasound transducers and vertical-cavity surface-emitting laser (VCSEL) diodes. To date, this kind of design has the smallest size in the literature because we greatly reduced the sizes of both ultrasound transducers and laser sources. The laser diodes only need to be connected to an external compact laser diode driver. The patch can be attached to the skin with medical tape, allowing hands-free monitoring.



Supplementary Figure 10 | Characterization of the piezoelectric transducers. **a**, The impedance and phase angle of a typical piezoelectric transducer element. The resonant and antiresonant frequencies have been labeled. **b**, Resonant frequency, antiresonant frequency, and electromechanical coupling coefficient of all the 240 transducer elements, showing the consistency of the fabrication process.

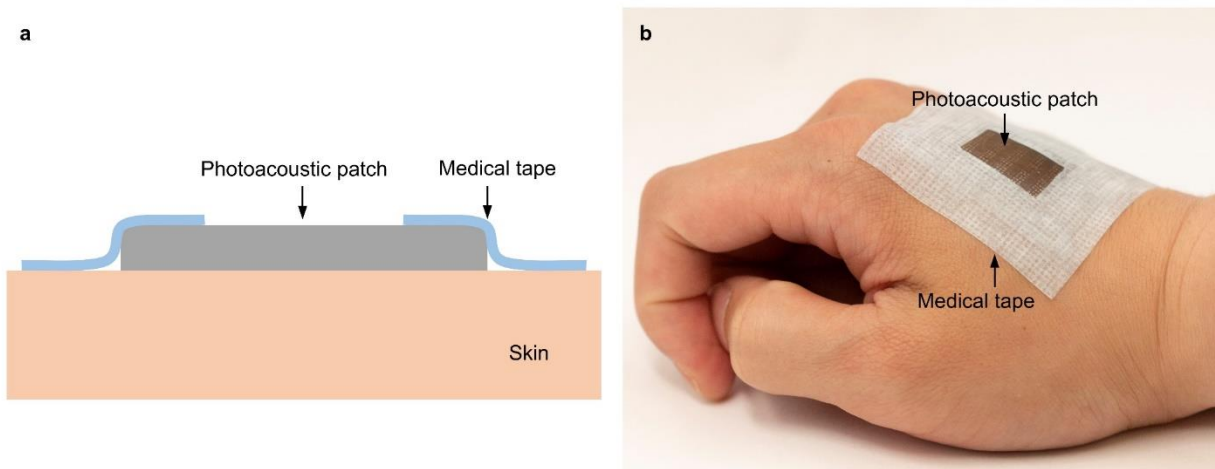


Supplementary Figure 11 | Influence of mechanical deformations on the transducer impedance. **a**, Distribution of representative transducer elements measured under mechanical deformations. Changes in resonant frequencies and impedance when **b**, bending, **c**, stretching and, **d**, twisting the soft photoacoustic patch. Those deformations have minimal impact on the transducer impedance.

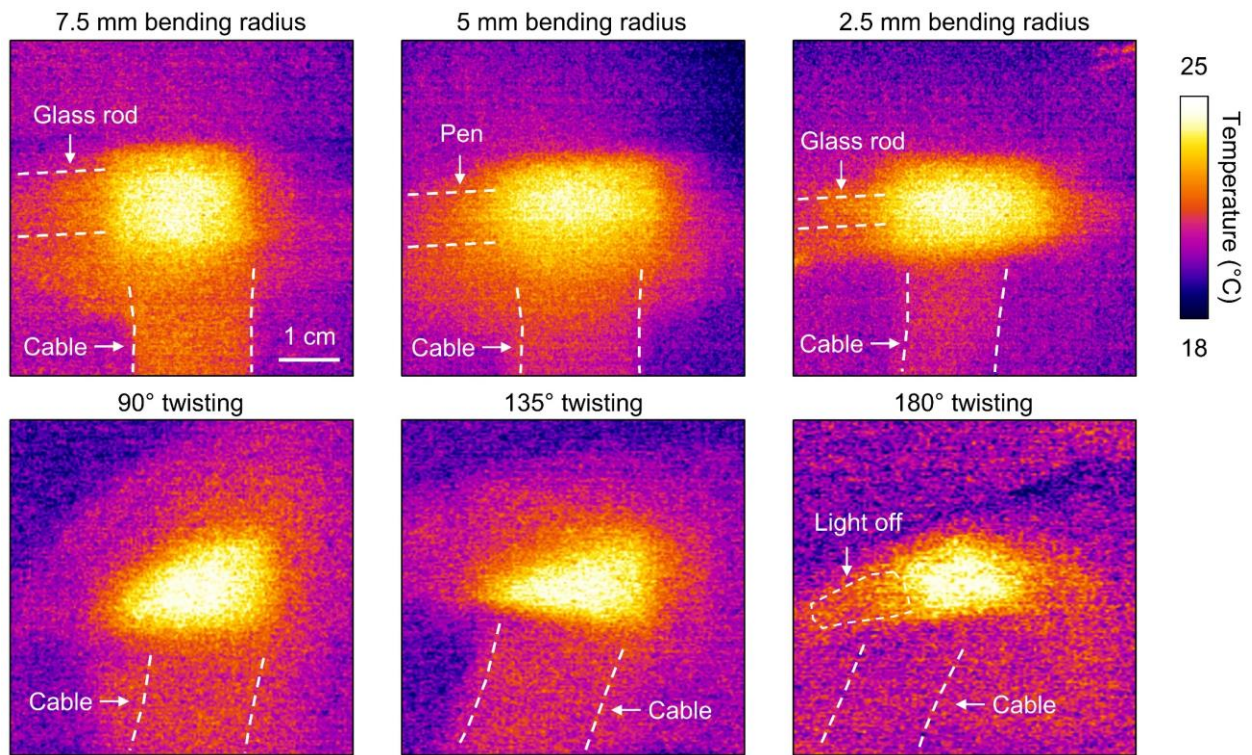


Supplementary Figure 12 | Influence of backing layer thickness on the transducer performance. The backing layer decreases the signal amplitude if too thick. We need to make sure the transducers have high sensitivity to receive weak photoacoustic signals, and small thickness not to affect the flexibility and stretchability of the patch. These two factors require the thickness of the backing layer to be as small as possible. On other hand, we still need the backing layer to dampen excessive vibrations to improve the signal bandwidth. In our design, high sensitivity and high flexibility are more important than high bandwidth. To measure the relationships among bandwidth, signal amplitude, and the thickness of the backing layer, we fabricated five different transducer elements, which have the same size of $3 \text{ mm} \times 3 \text{ mm}$, but different thicknesses of the backing layer: 0, 0.1, 0.2, 0.6, and 0.8 mm. We excited each element with the same voltage of 50 V and measured the pulse echo signal of each element reflected by an aluminum block. **a**, Time-domain pulse echo signals of different transducers. **b**, Frequency-domain pulse echo signals. **c**, The relationship between the signal amplitude and backing layer thickness. Data are presented as mean values \pm standard deviation of 20 measurements. **d**, The relationship between the -6dB bandwidth and backing layer thickness. Data are presented as mean values \pm

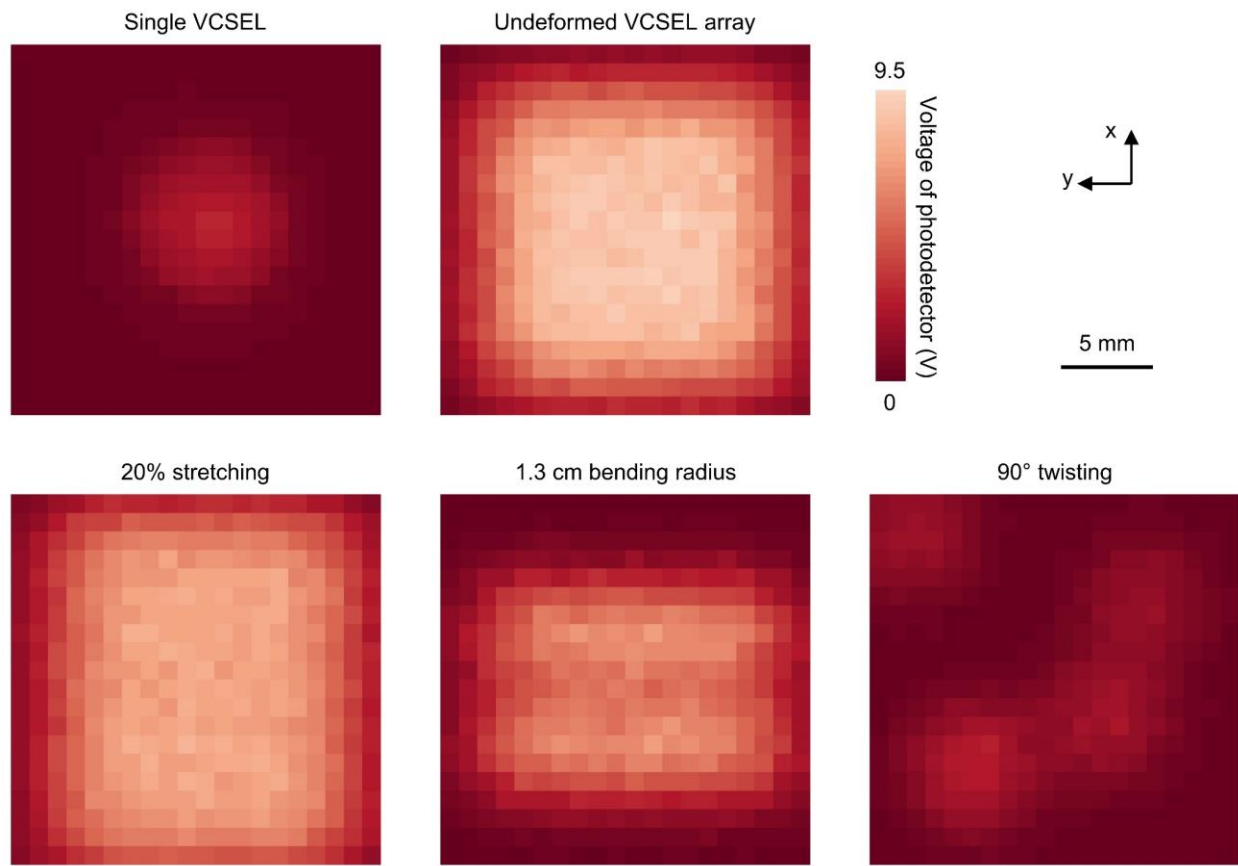
standard deviation of 20 measurements. The results show that the amplitude decreases and the bandwidth increases, when the thickness of backing layer increases. In this study, we set the backing thickness as 0.2 mm.



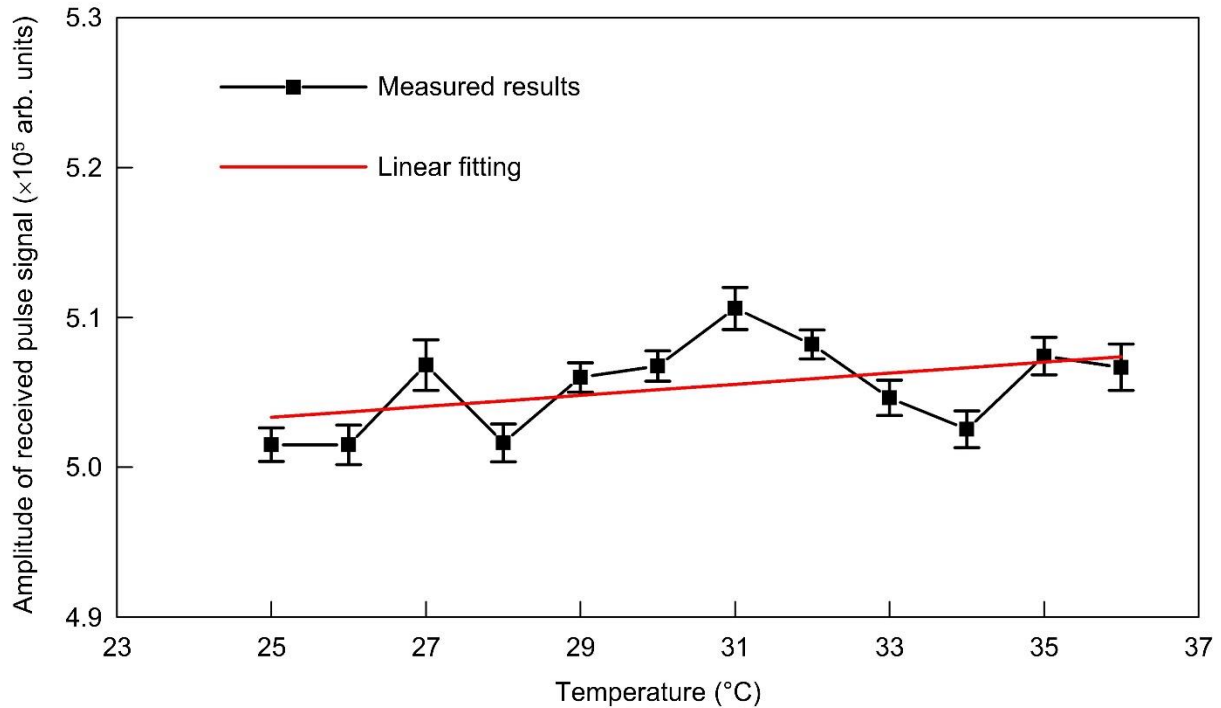
Supplementary Figure 13 | Conformal attaching of the photoacoustic patch to the skin. **a**, A schematic cross-sectional image of attaching the photoacoustic patch to the skin by using a medical tape. The photoacoustic patch is fabricated by encapsulating ultrasound transducer elements and laser diodes in flexible and stretchable silicone elastomer, i.e., Ecoflex in this work. The ultrasound transducer elements and laser diodes are connected by stretchable serpentine electrodes, in an island-bridge structure. The photoacoustic patch is rigid locally at each ultrasound transducer element and laser diode but soft globally on the system level. Therefore, no external pressure is required to conformally attach the photoacoustic patch to the skin. **b**, A photo shows attaching the photoacoustic patch on the hand with only a medical tape.



Supplementary Figure 14 | Infrared camera images of the photoacoustic patch under different degrees of bending and twisting. The patch can survive a bending radius of 2.5 mm and a twisting angle of 135°.

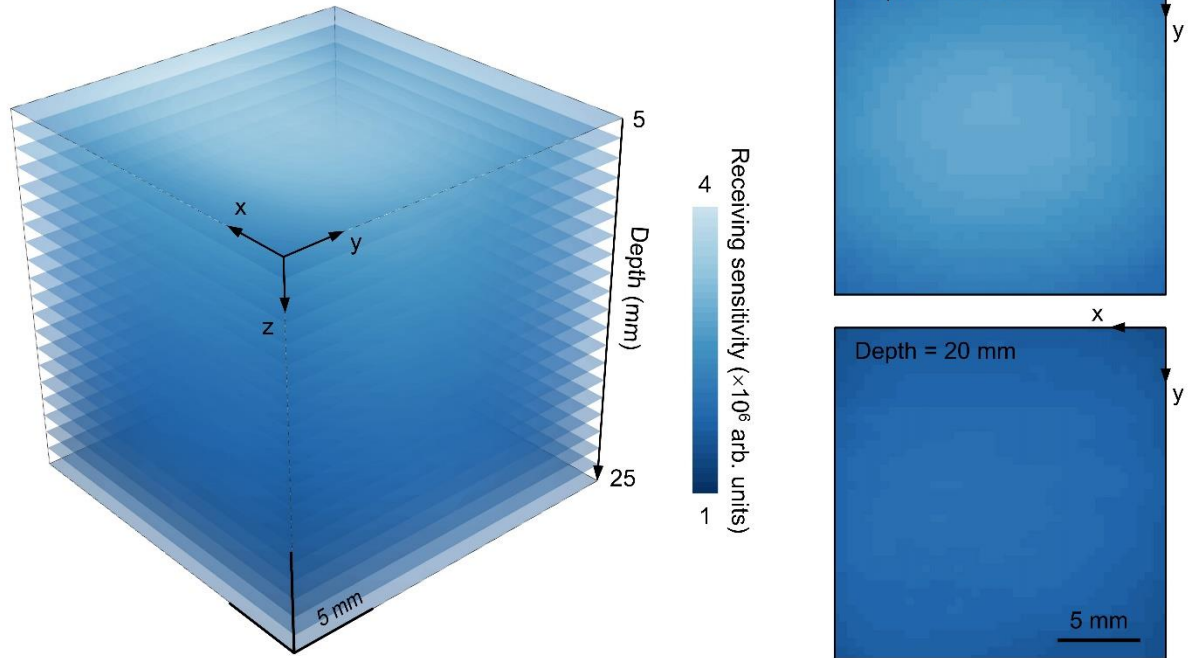


Supplementary Figure 15 | Light intensity distributions of a single VCSEL, and an undeformed, stretched, bent, or twisted VCSEL array. The optical intensity distribution under 20% uniaxial stretching is very similar to that of the undeformed state. Under large degrees of bending and twisting, the light distribution will be distorted.

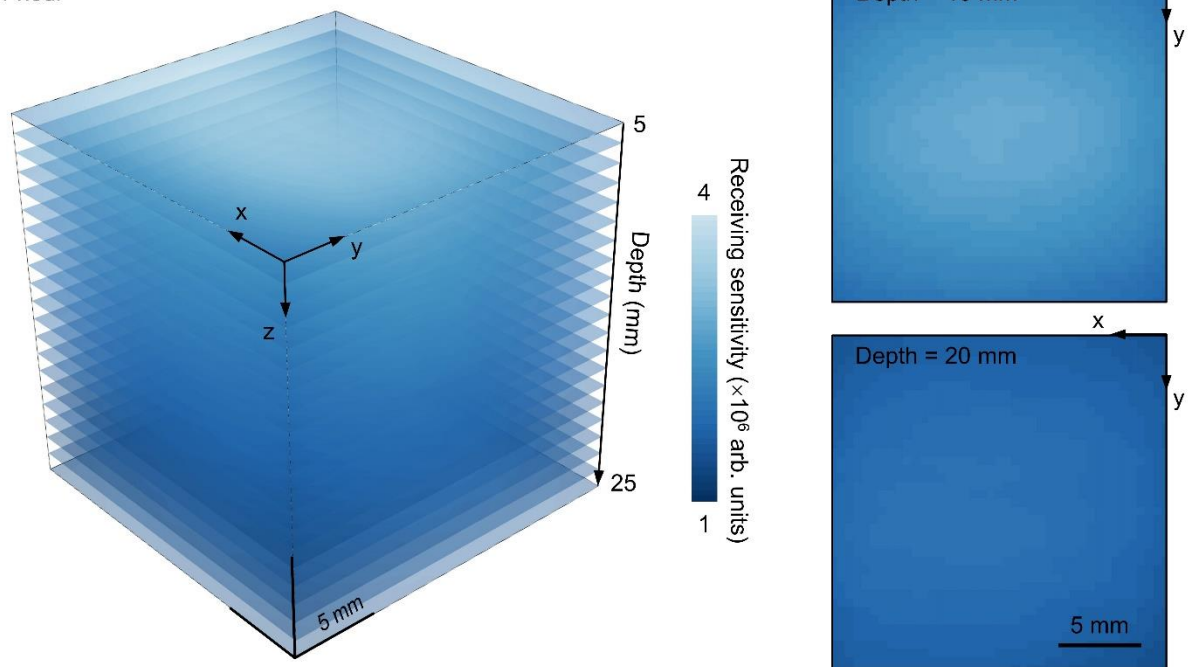


Supplementary Figure 16 | Tested relationship between the receiving sensitivity of piezoelectric transducers and temperature. The patch and a commercial ultrasound probe (Verasonics, P4-2v) were immersed in water directly opposite to each other. The water’s initial temperature was about 40 °C. The commercial probe was excited by a voltage pulse at a transmitting frequency of 2 MHz, while the photoacoustic patch received the ultrasound signals. A thermocouple (Omega Engineering Inc., SC-TT-K-30-36) was immersed in water to simultaneously measure the water temperature. Signals received by the ultrasound transducer in the patch were recorded at different temperatures from 25 °C to 36 °C, which was the temperature range of the photoacoustic patch after being turned on. The signals’ peak-to-peak amplitudes are shown here. The square points are the average of 20 measurements, while the error bars are the stand deviations. The red line is the linear fitting of the average amplitudes. As shown, there is fluctuation at different temperatures. The highest amplitude is about 1.8% higher than the lowest, which can be further reduced by averaging more measurements and transducers. The fitting result shows a 0.8% increase of signal amplitude as the temperature increases. This increase is very small, because the photoacoustic signal typically increases about 5% per degree centigrade⁶⁰. In addition, the temperature of photoacoustic patch reaches a stable state after being turned on for about 8 minutes. We can easily avoid the influence of temperature on the receiving sensitivity if we start the long-term monitoring from 8 minutes after turning on the laser diodes.

0 hour

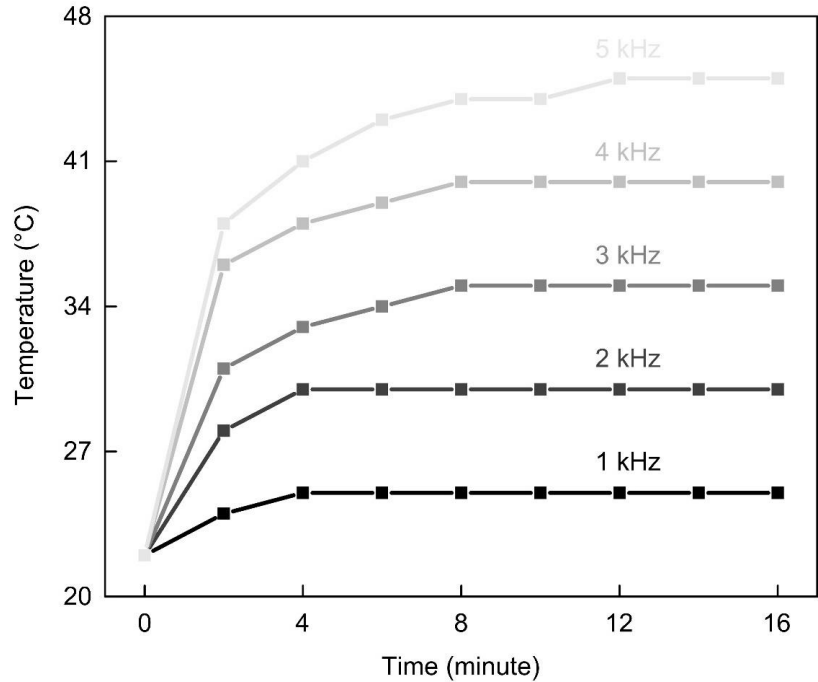


1 hour

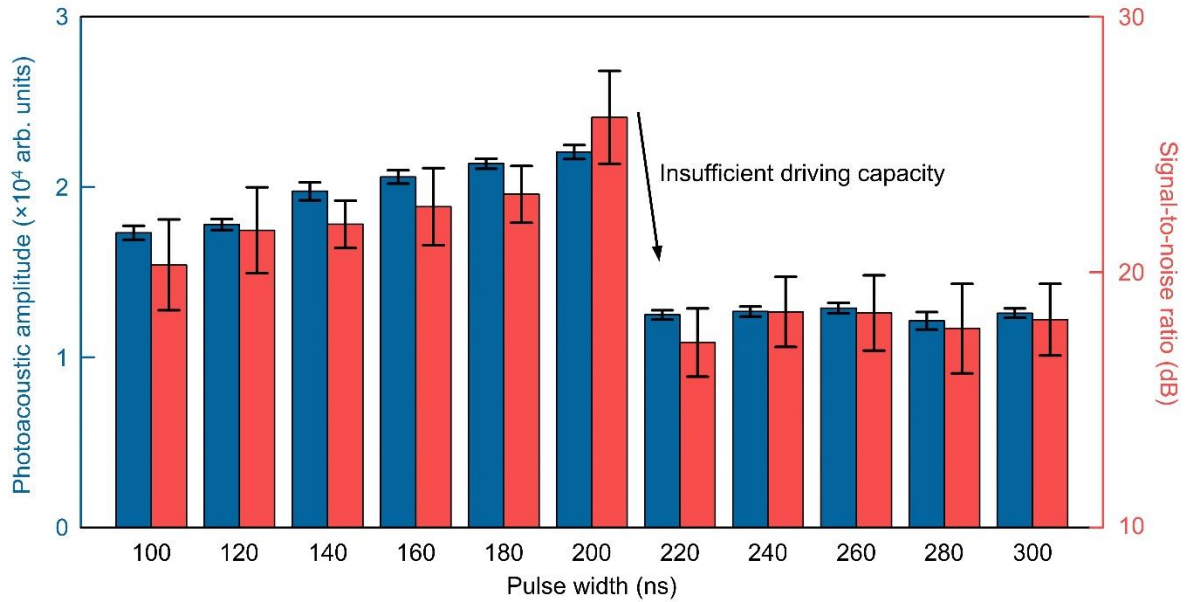


Supplementary Figure 17 | Measured receiving sensitivity mappings of the photoacoustic patch at 0 hour and 1 hour, respectively. The 3D image shows the mappings at 21 depths from 5 mm to 25 mm. Two horizontal planes at the depth of 10 mm and 20 mm are also shown on the right, respectively. The receiving sensitivity of the photoacoustic patch was measured in a water tank (ONDA, AIMS III). The results at two moments are very close, which may be because the

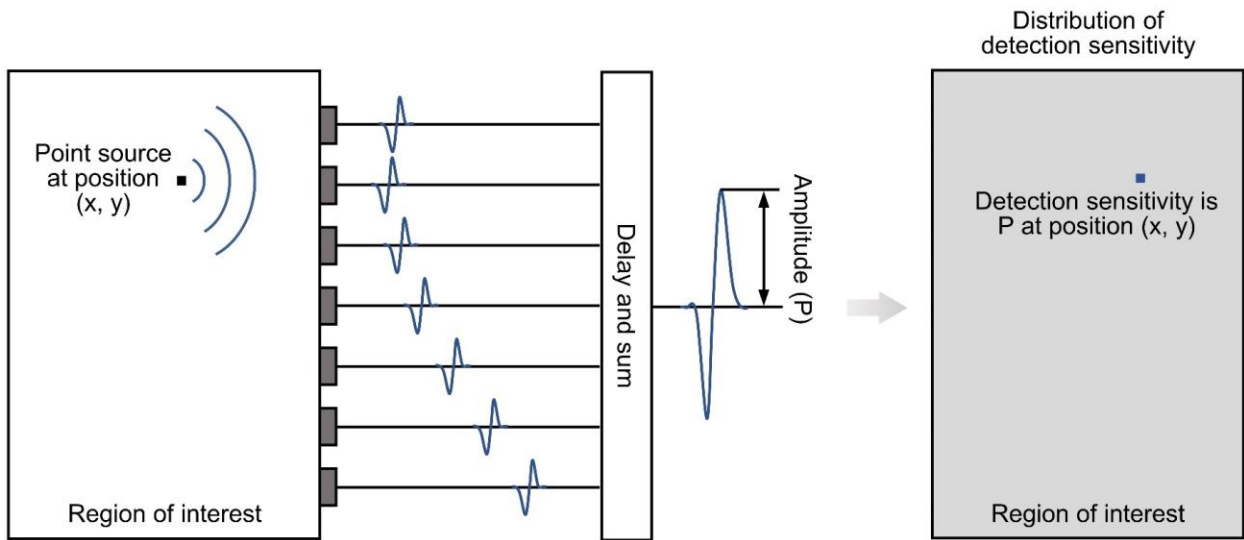
photoacoustic patch was immersed in water. The heat was dissipated into the water tank. However, according to the analysis in Supplementary Figure 16, the receiving sensitivity of the ultrasound transducers will not change too much either, even when the water temperature rises from 25 °C to 36 °C. Therefore, the dependency of receiving sensitivity on the temperature is not a concern in this study.



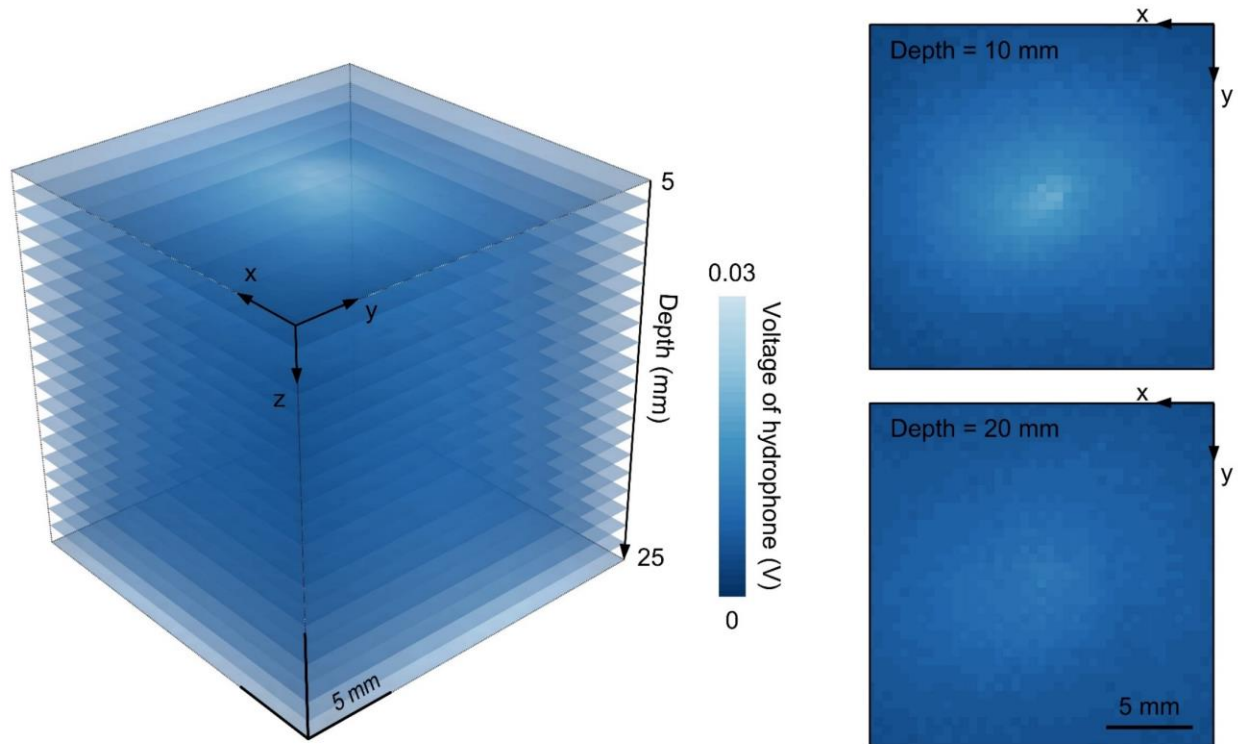
Supplementary Figure 18 | Influence of the pulse repetition frequency of the VCSELs on the overall patch temperature. The temperature increases as the pulse repetition frequency increases. Under a given pulse repetition frequency, the patch temperature gradually rises within the first few minutes and then stabilizes. 3 kHz is used in this study.



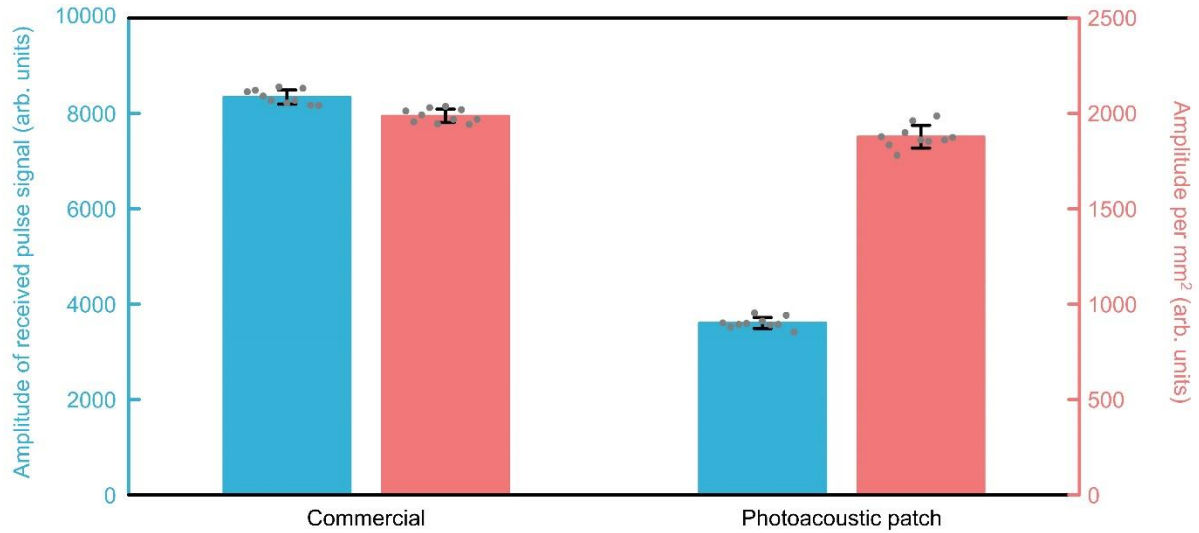
Supplementary Figure 19 | Influence of laser pulse width/duration on the photoacoustic signal amplitude and signal-to-noise ratio. The photoacoustic signal amplitude and signal-to-noise ratio increase as the pulse duration when the duration is below 200 ns. When the duration is above 200 ns, the laser diode driver (PicoLAS) used in this work cannot support further increased pulse duration due to its limited power. Data are presented as mean values \pm standard deviation of 20 measurements.



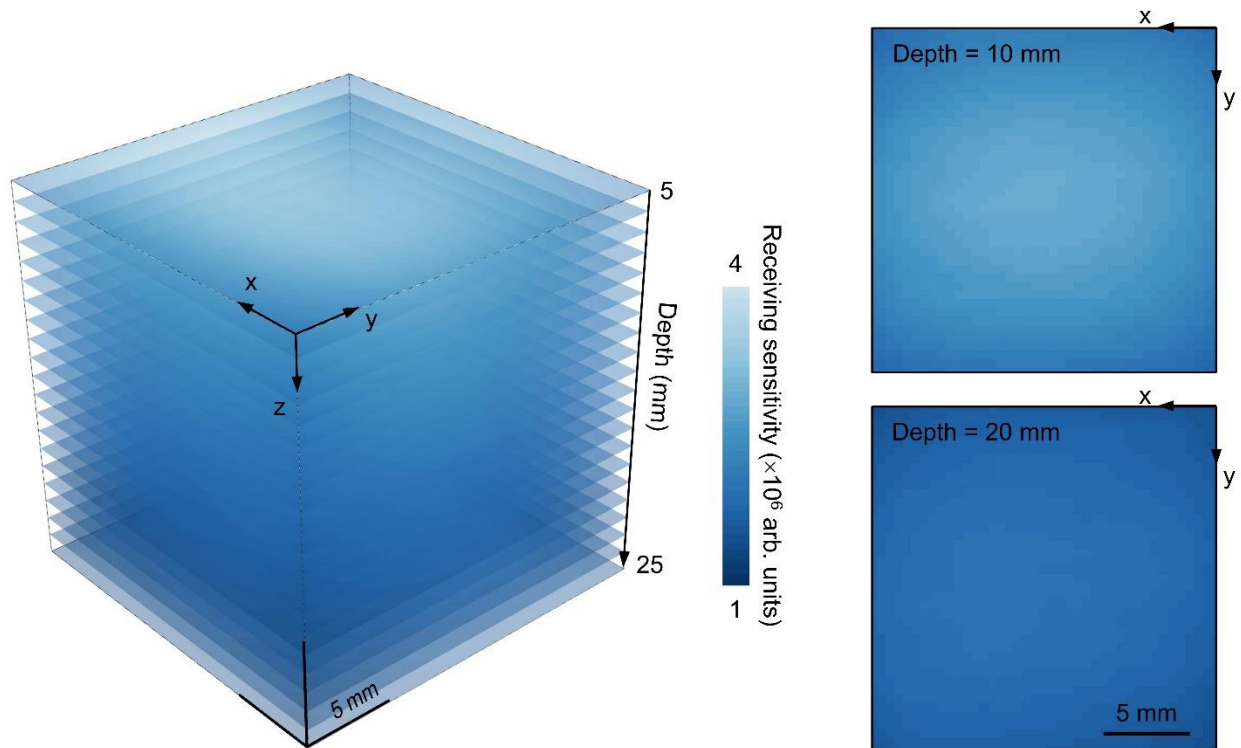
Supplementary Figure 20 | The method of calculating detection sensitivity. Assuming there is a point source at the position (x, y) , the amplitude of beamformed signals (P) is set as the detection sensitivity of this position illustrated in Fig. 2d.



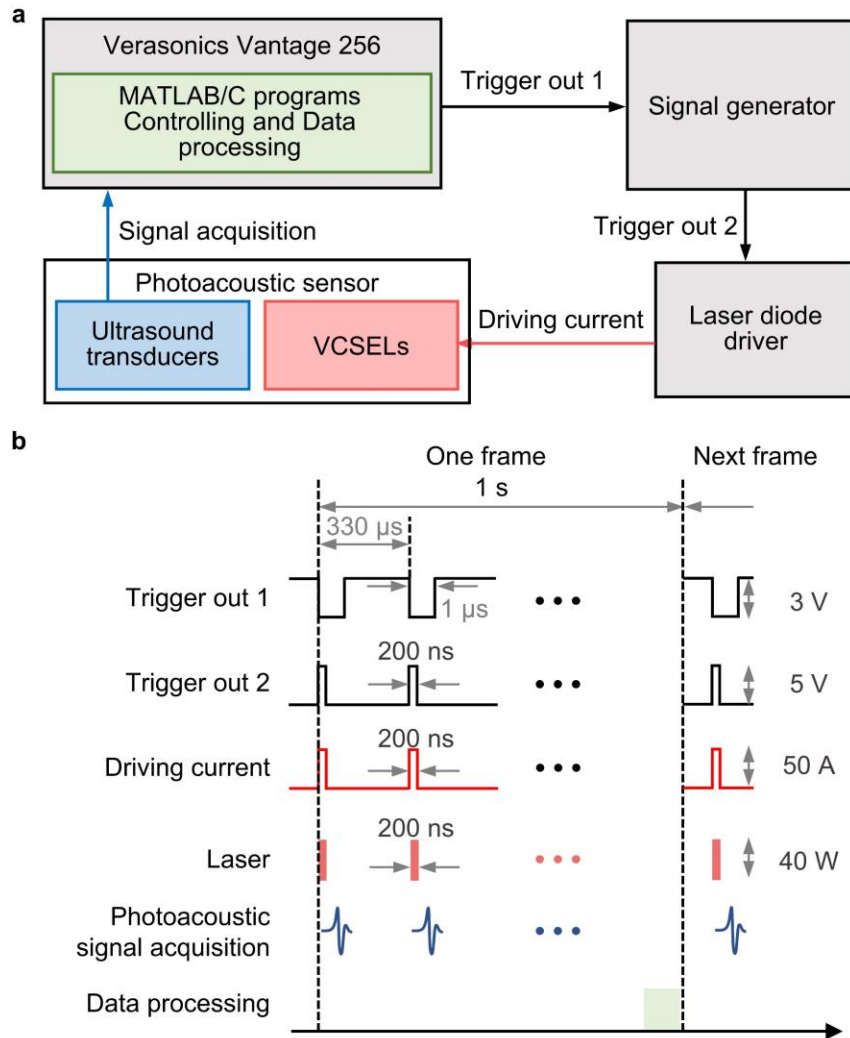
Supplementary Figure 21 | Measured transmitting sound field of one transducer element. The 3D image shows the mappings at 21 depths from 5 mm to 25 mm. Two horizontal planes at the depth of 10 mm and 20 mm are shown on the right, respectively. The figure shows the 3D ultrasound field underneath the transducer at a depth from 5 mm to 25 mm, with a horizontal area of 2 cm × 2 cm.



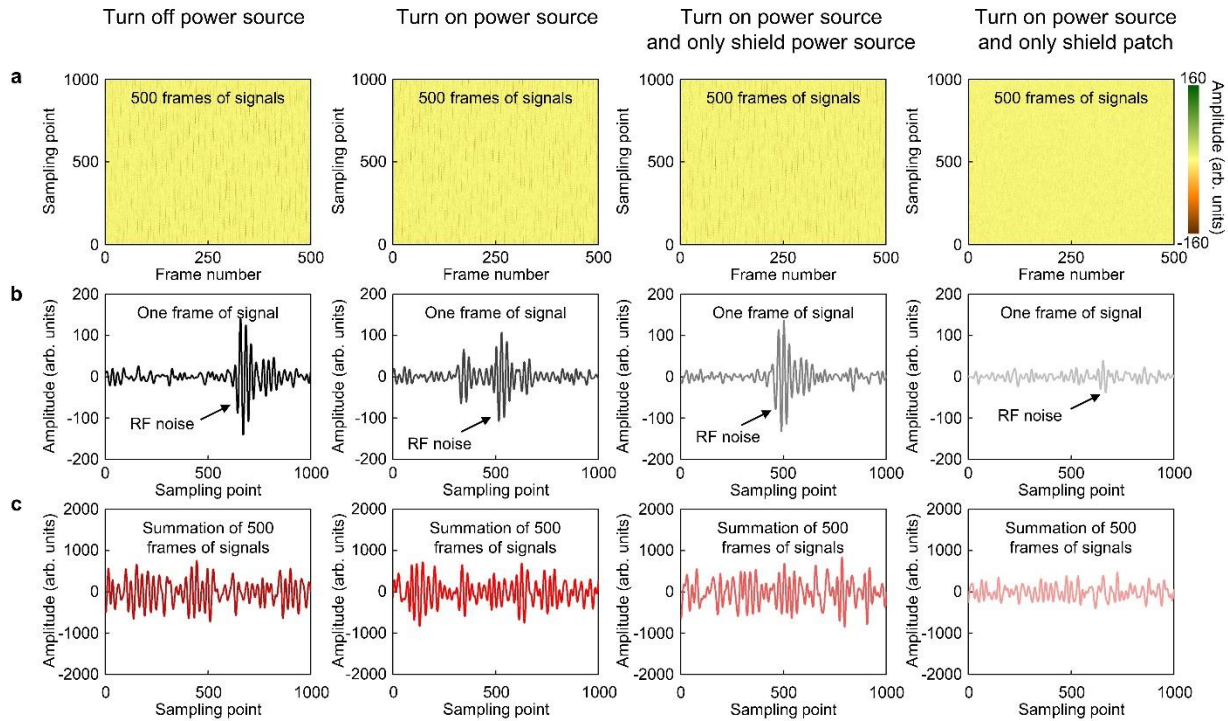
Supplementary Figure 22 | Comparison of receiving sensitivity between commercial ultrasound probe and the photoacoustic patch. Blue and red bars show the sensitivity without and with considering the area of transducer element. The sensing areas of one transducer were 4.2 mm² and 1.92 mm² for the commercial probe and the patch, respectively. Because the amplitude of measured signal increases as the transducer area, we also calculated the signal amplitude per square millimeter. The results are the averages of 10 measurements. The error bars denote the standard deviation. Gray dots show the data of 10 measurements. The blue column bars show that the commercial probe has higher signal amplitude than the patch. Considering the difference in the transducer area, the red bars show that the amplitude of the patch is only about 11% lower than the commercial probe, which means the patch has a very similar performance to the commercial probe.



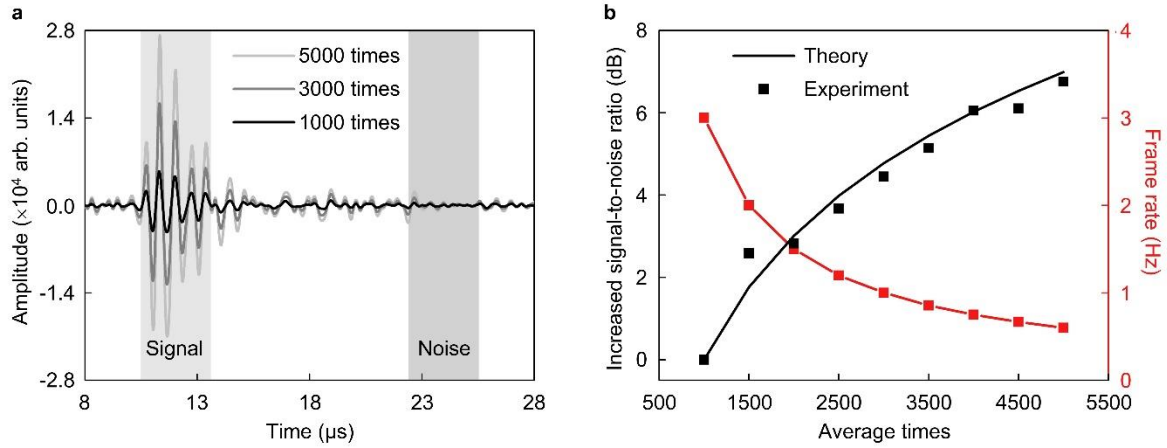
Supplementary Figure 23 | Measured receiving sensitivity mapping of the photoacoustic patch. The 3D image shows the mappings at 21 depths from 5 mm to 25 mm. Two horizontal planes at the depth of 10 mm and 20 mm are shown on the right, respectively. The results show the normalized 3D sensing field underneath the patch at a depth from 5 mm to 25 mm, with a horizontal area of $2\text{ cm} \times 2\text{ cm}$.



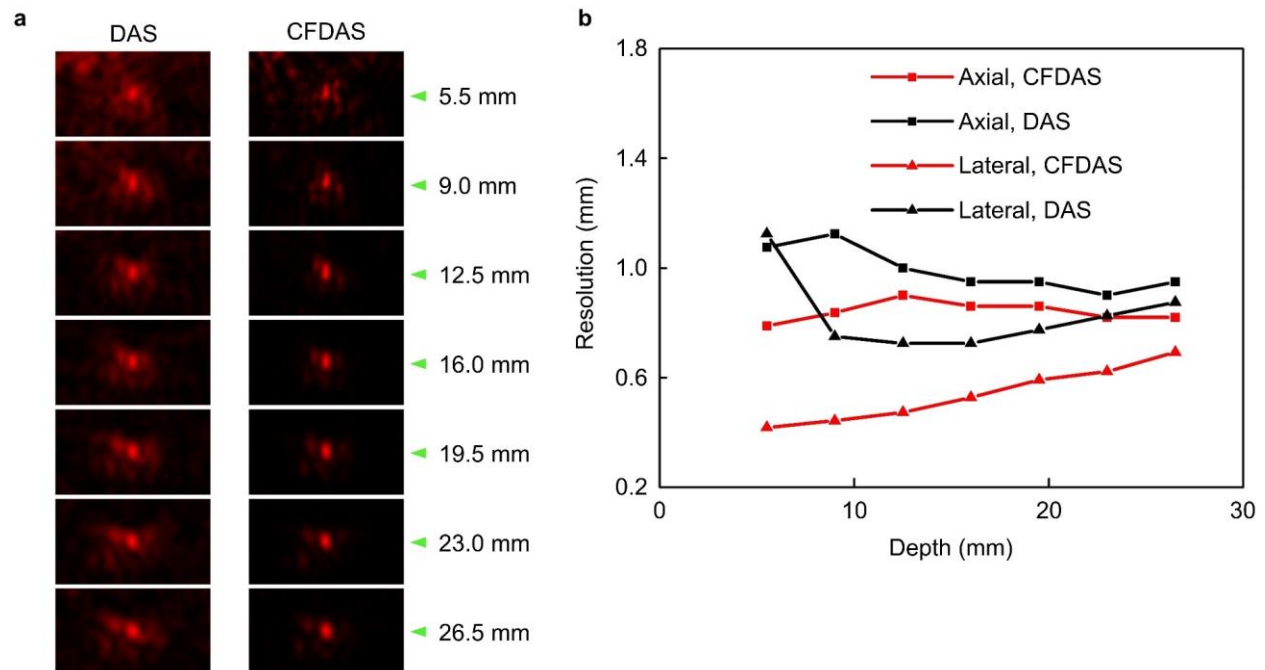
Supplementary Figure 24 | Schematic framework of the photoacoustic system. a, The hardware framework of the system. The Verasonics Vantage 256 controls the timing sequence of the entire system through a customized MATLAB program. It outputs a trigger signal to the signal generator, which then exports a pulsed trigger signal to the laser diode driver. With the driving current, the laser diodes will emit laser and excite the hemoglobin molecules to generate photoacoustic waves. At the moment of laser emission, the transducers start to measure photoacoustic waves and relay the signals to the Verasonics for processing, which is done by customized MATLAB and C programs. **b,** Timing sequence of the system. The pulse repetition frequency of laser emission and signal receiving is 3 kHz. One frame of image is reconstructed based on 3000 averaged signals in one second. The frequency of measured photoacoustic signal is mainly decided by the laser pulse width and the bandwidth of the piezoelectric transducer.



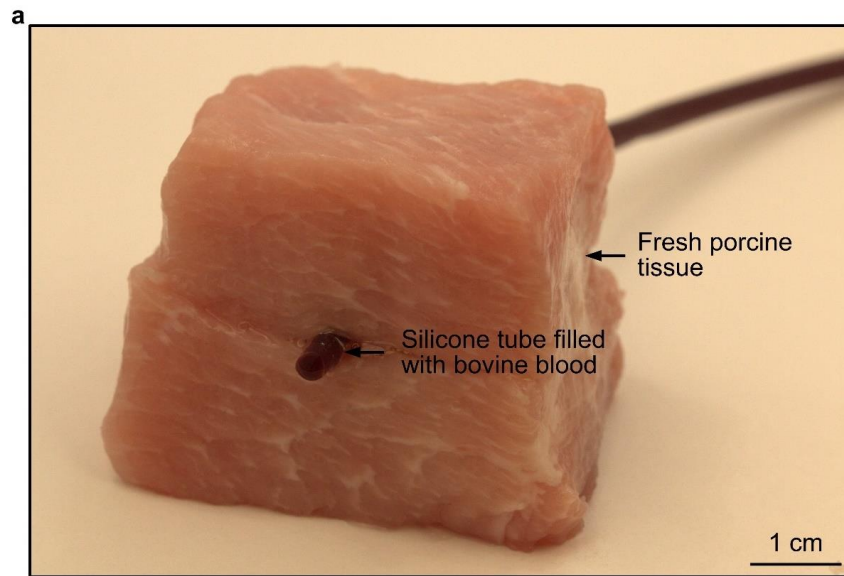
Supplementary Figure 25 | Influence of external radiofrequency (RF) noise. We did four groups of tests to show the influence of RF noise, including 1. turning off the power supply and function generator; 2. turning on the power supply and function generator, applying no shielding; 3. turning on the power supply and function generator, and only shielding the power supply and function generator; 4 turning on the power supply and function generator, and only shielding the photoacoustic patch. For the last situation, we assume it is the ideal case since it should eliminate the noise theoretically. We saved and analyzed the background noise at these four conditions. **a**, 500 frames of time-domain background noise at these four different situations are shown here. Only 500 frames of signals were measured to save storage space. It is obvious that strong RF noise exists in the first three cases, while shielding the patch itself can decrease the RF noise greatly. **b**, One typical frame of the temporal background noise at different situations. The background noise for the fourth situation is very stationary, only affected by weak RF noise. **c**, Summation of all of the 500 frames of noise. The summation is also used in the photoacoustic signal measurement, which is equivalent to signal averaging. The summation results show that RF noise is greatly decreased for all cases, benefiting from the data summation. All of the noise curves present the stationary feature, even without any shielding. The RF noise level may be further decreased by more average times. In addition, the noise levels of all of the first three cases are close to each other and only slightly higher than the ideal fourth case. We can also conclude that the power source and function generators introduce neglectable noise, including RF noise and stationary noise.



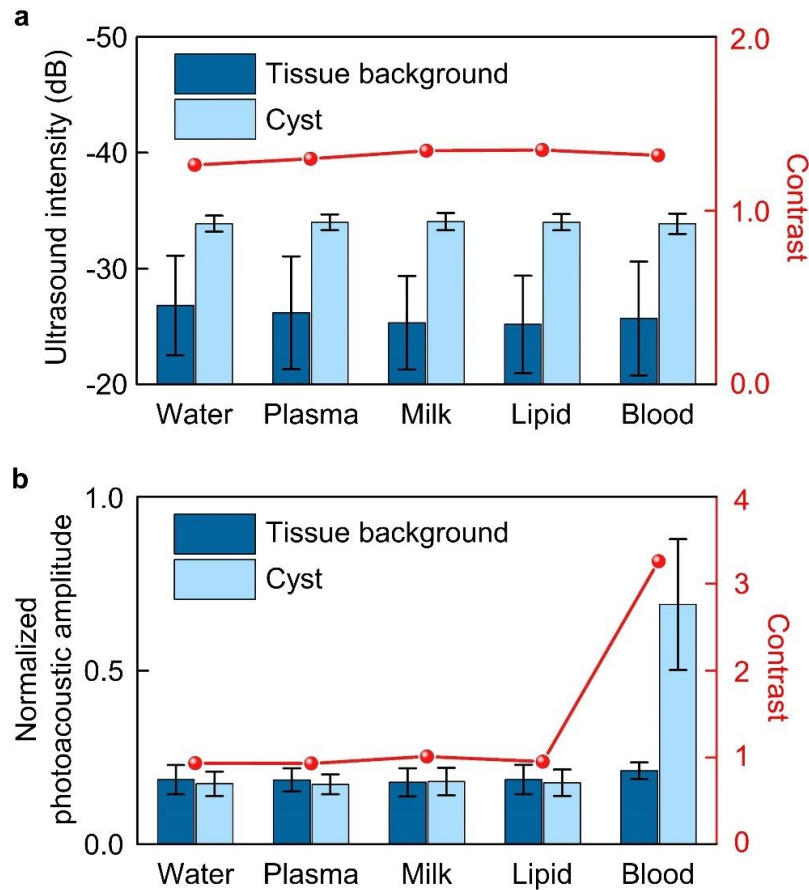
Supplementary Figure 26 | Influence of the average times on the signal-to-noise ratio. a, Photoacoustic signals averaged by 1000, 3000, and 5000 times, respectively. **b,** The signal-to-noise ratio increases as the average times. The increased value is calculated by setting the value averaged by 1000 times as the baseline. The frame rate decreases as the average times. 3000 average times are selected in this work because of the trade-off between the signal-to-noise ratio and the frame rate.



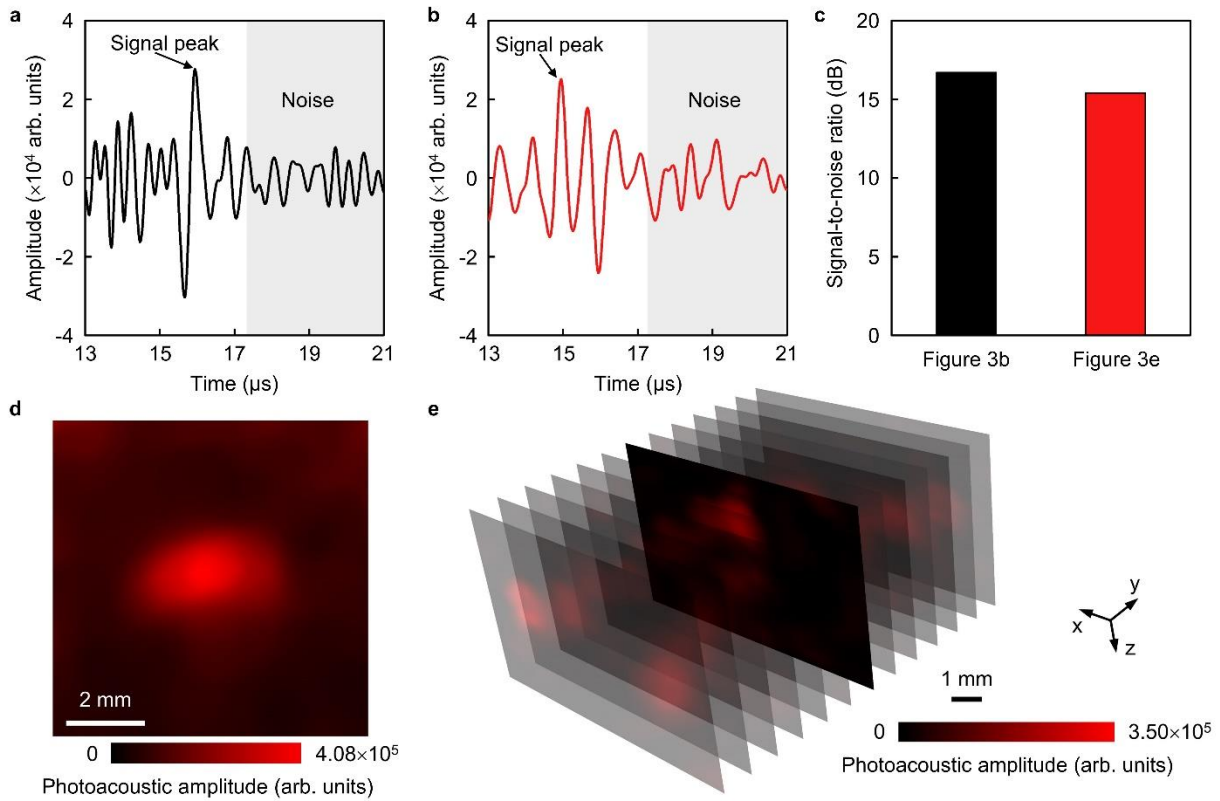
Supplementary Figure 27 | Comparison between two different image reconstruction algorithms, Delay And Sum (DAS) and Coherent Factor weighted Delay And Sum (CFDAS). **a**, Photoacoustic images are reconstructed based on the DAS and CFDAS, respectively. To characterize the resolutions of a photoacoustic imaging system, a linear object with very small diameter is usually used, such as hairs^{91,111,112}, carbon fibers^{113,114}. We adopted those well-established standard methods for resolution characterization by embedding the linear sources in real biological tissues¹¹², water¹¹³⁻¹¹⁷, or water like gelatin phantoms^{91,111,118,119}. According to the literature, we also find that most studies show the resolution characterization in water or water like gelatin phantoms. Water or water like gelatin phantoms have lower optical absorption and scattering coefficients than realistic biological tissues, which will improve the signal to noise ratio of photoacoustic signals and contrast to noise ratio of photoacoustic images. But they will not affect the characterization results of imaging resolution. Therefore, we used the gelatin phantom as the background media for better accuracy and ease of operation. The hairs were embedded in different gelatin phantoms, respectively. **b**, Axial and lateral resolutions versus the depth. The CFDAS offers better axial and lateral resolutions than the DAS at all depths and is thus used in this work.



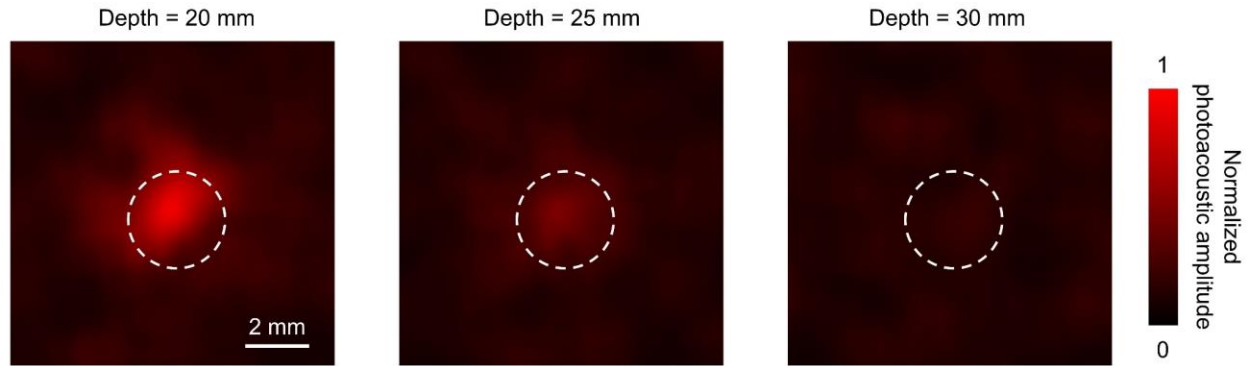
Supplementary Figure 28 | Optical photographs of the cyst phantom and different biofluids.
a, The cyst phantom is made of porcine tissues and a transparent silicone tube filled with different biofluids. **b**, Various biofluids that can probably be found in cysts in the human body.



Supplementary Figure 29 | The average ultrasound intensities and photoacoustic amplitudes inside and outside the cysts. a, For the ultrasound images, the intensities of the tissue backgrounds and cyst inclusions are close to each other for all cysts, as well as their intensity contrasts. The bars show the average ultrasound intensities of 400 image pixels in the cyst and background, respectively. The error bar shows the standard deviation. **b,** For the photoacoustic images, the amplitudes of the tissue backgrounds are the same for all cysts, but the blood cyst has the highest amplitude and therefore the highest inside to outside intensity contrast among all cysts. The bars show the average photoacoustic amplitudes of 2000 image pixels in the cyst and background, respectively. The error bar shows the standard deviation.

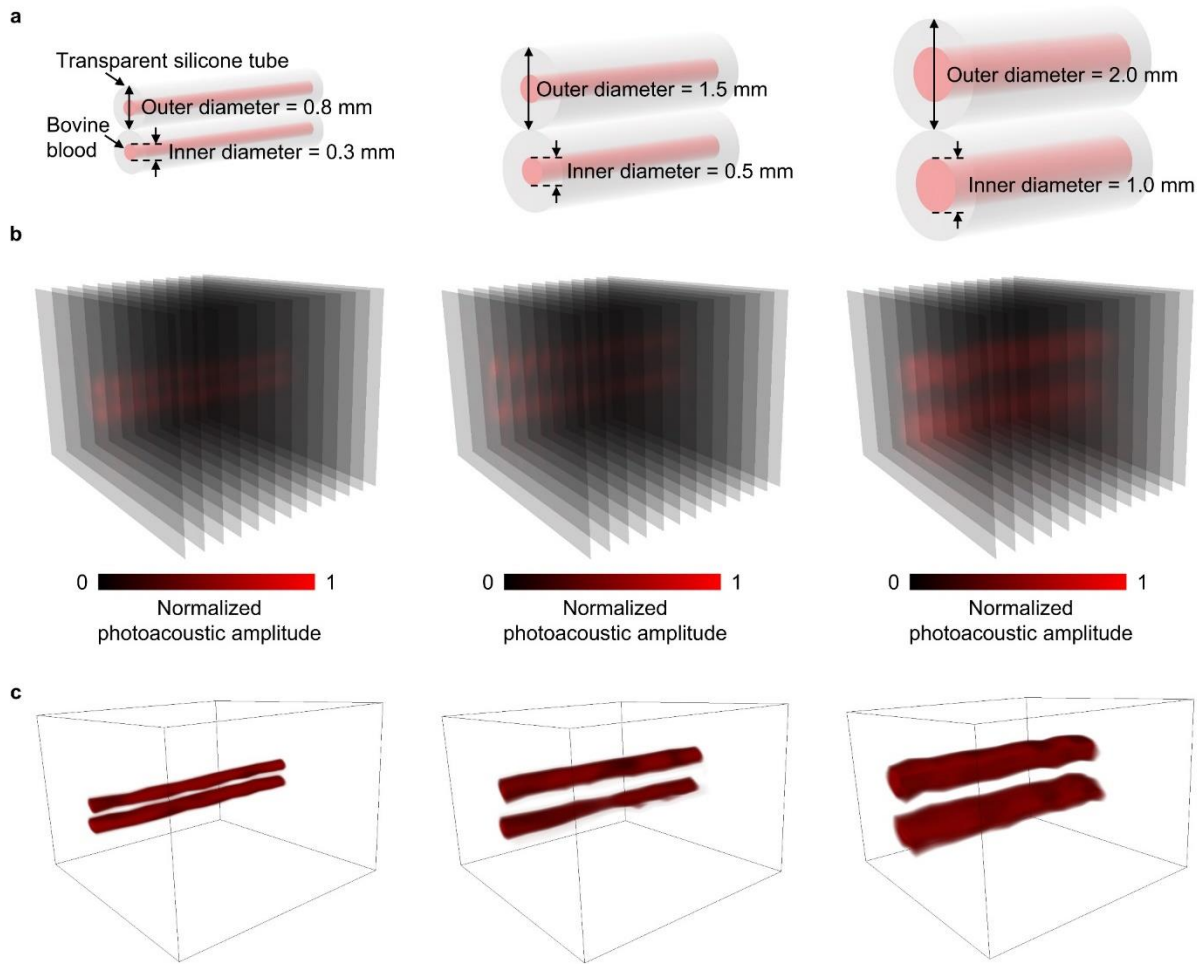


Supplementary Figure 30 | Supplementary experimental data in porcine tissues. a, A typical time-domain signal of the phantom in Fig. 3b. **b,** A typical time-domain signal of the phantom in Fig. 3e. **c,** Signal-to-noise ratios of the signals in **a** and **b**. Signal-to-noise ratio is defined as $20\log_{10}(\text{Peak photoacoustic signal}/\text{Root mean squared error of noise})^{108-110}$. **d,** The image in Fig. 3b in absolute scale. **e,** The image in Fig. 3d in absolute scale.

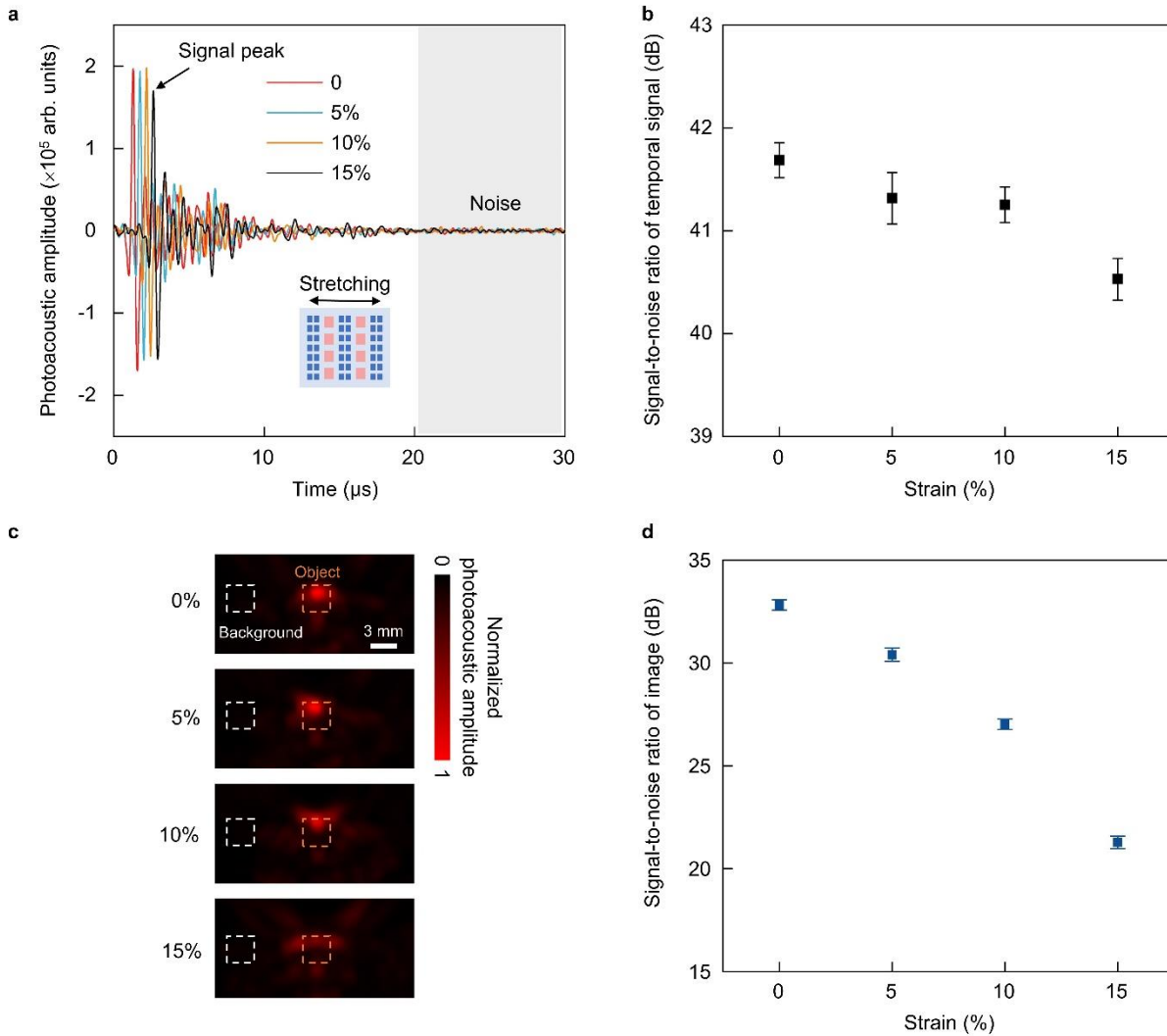


Supplementary Figure 31 | Images of the silicone tube in the porcine tissue at different depths.

To determine the maximum detection depth of the photoacoustic patch, we performed an *ex-vivo* test on porcine tissue phantoms. We embedded a silicone tube under porcine tissues. The tube was filled with bovine blood. We tested the photoacoustic signals of the tube at the depth of 2 cm, 2.5 cm, and 3 cm. The photoacoustic images were reconstructed and shown. All the images were normalized by the same factor. At the depth of 20 mm, the tube has higher amplitude than the background, which shows good image result. At the depth of 25 mm, the amplitude of the tube is slightly higher than the background. At the depth of 30 mm, the tube and the background media are indistinguishable, which means the photoacoustic patch cannot operate at this detection depth. Therefore, we can determine the maximum penetration depth of the photoacoustic patch is about 25 mm on *ex-vivo* porcine tissue phantoms.

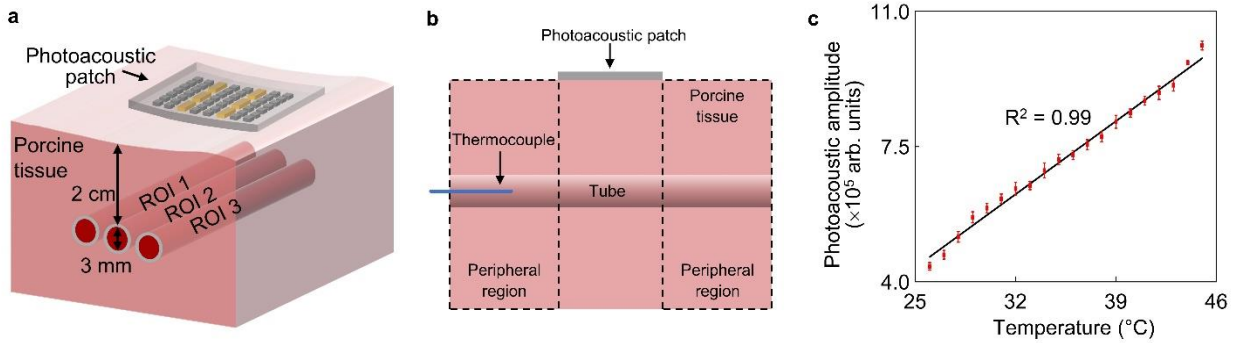


Supplementary Figure 32 | 3D photoacoustic imaging of overlapping vessels. To test the capability of 3D imaging of two overlapping vessels, we detected three different gelatin phantoms. **a**, Schematics of three phantoms, which contain two overlapping transparent silicone tubes, respectively. The tubes are filled with bovine blood. The outer diameters of the tubes are 0.8, 1.5, and 2.0 mm, while the inner diameters are 0.3, 0.5, and 1.0 mm, respectively. Those numbers resemble typical sizes of major vessels in the human body. **b**, 13 slices of reconstructed 2D photoacoustic images of the overlapping tubes. It is clear that all of the overlapping vessels are distinguishable. **c**, 3D images of the corresponding overlapping vessels.

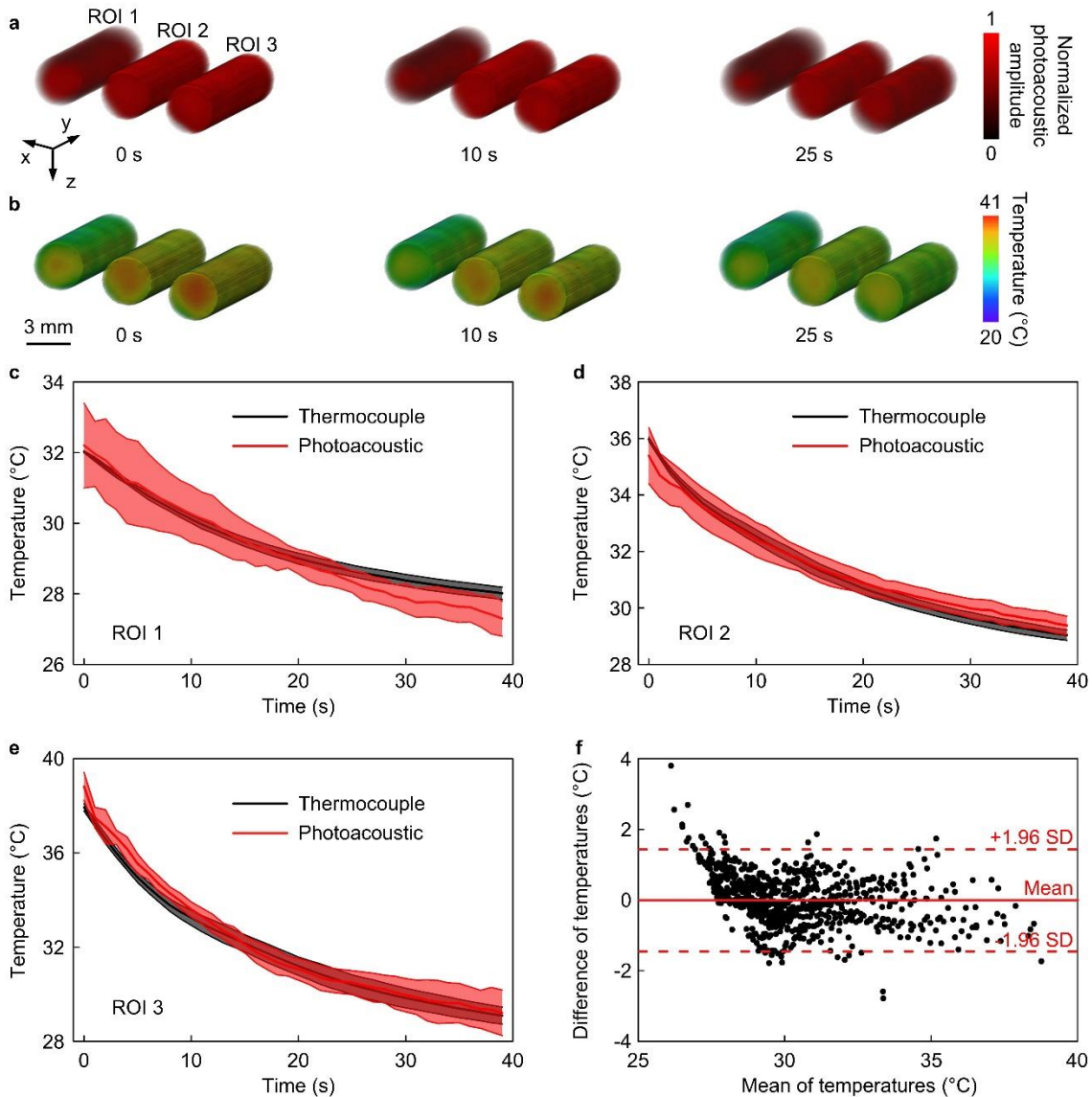


Supplementary Figure 33 | Influence of strain on the SNR of the patch. To test the influence of stretching on the device performance, we tested the device on a gelatin phantom, which contained a transparent silicone tube filled with bovine blood. We quantitatively calculated the signal to noise ratio (SNR) of both temporal signals and photoacoustic images under different strain levels. **a**, The photoacoustic patch was stretched uniaxially along the horizontal direction by 0%, 5%, 10%, and 15%. Typical temporal photoacoustic signals of one ultrasound transducer are shown when the patch was under different strains. The signals under strains are shifted in time by about 0.5, 1, and 1.5 μ s, respectively to make waveforms visually distinguishable. When the patch was stretched, the distance of the laser diodes increased. This could slightly decrease the optical intensity in the phantom. Therefore, the amplitude of photoacoustic signal slightly decreased. SNR of temporal signal is defined as $20\log_{10}(\text{Peak photoacoustic signal}/\text{Root mean squared error of noise})^{108-110}$. **b**, SNR of temporal signals has a small decrease as the patch is stretched. Data are presented as mean values \pm standard deviation of 10 measurements. However, stretching would also increase the distance between ultrasound transducer elements. As a result, the image reconstruction will be affected if we still use the original transducer positions in the beamforming algorithm. **c**, The photoacoustic images under different strain levels. As the strain increases, the reconstructed images show stronger distortion. The image quality substantially degraded when the

strain level reached 15%. For photoacoustic images, the SNR is defined as $20\log_{10}(\text{Average pixel values in the region of object (orange box)}/\text{Standard deviation of pixel values in the background (white box)})^{86,120}$. **d**, The image SNR will decrease as the strain level increases. Data are presented as mean values \pm standard deviation of 10 measurements. In this work, the photoacoustic patch could be attached to the skin with minimal stretching ($<5\%$). The image quality does not show noticeable degradation at 5% strain. For future applications when large strain is required, we can add an additional strain sensor on the photoacoustic patch to monitor the strain level as a way to compensate for the change of distance between transducers.

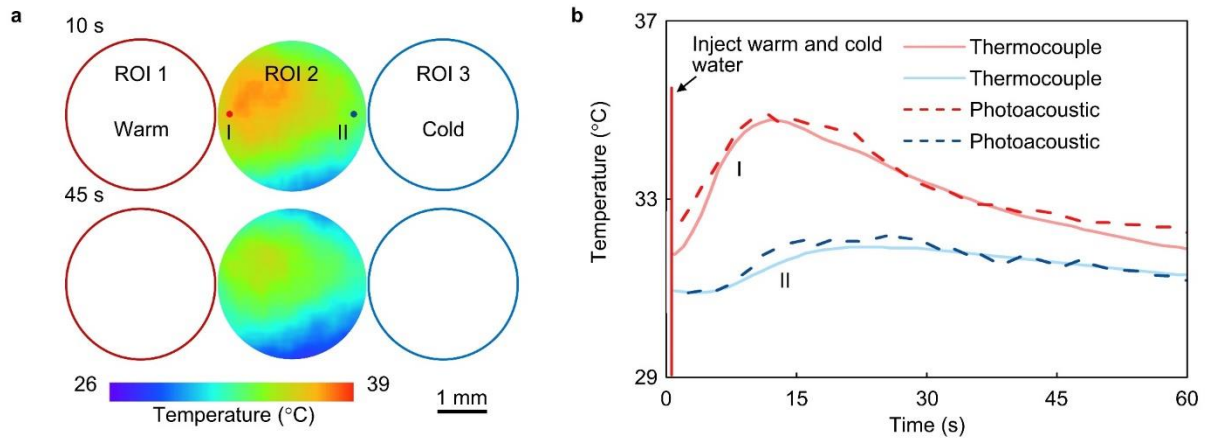


Supplementary Figure 34 | Relationship between the temperature measured by the thermocouple and the photoacoustic amplitude measured by the patch. To test the ability of photoacoustic patch to measure core temperature, we used the soft photoacoustic patch to measure the temperature in a phantom and checked its performance with thermocouples. **a**, The phantom is composed of warm bovine blood injected in three regions of interest (ROIs) underneath 2 cm thick room-temperature porcine tissues. Thermocouples were placed in the tubes, where the photoacoustic measurements were also taken for validation. **b**, Schematic showing the side view of the corresponding phantom. The peripheral regions mean those far from the photoacoustic patch in the horizontal direction, not directly underneath the patch. The porcine tissue phantom is large enough to keep the temperature uniform along the flowing direction inside the tubes enclosed by porcine tissues. **c**, Beamformed photoacoustic amplitude verse the temperature in the center of ROI 2. Data are presented as mean values \pm standard deviation of 20 measurements. Linear fitting ($R^2 \sim 0.99$) demonstrates the feasibility of core temperature measurement by the patch.

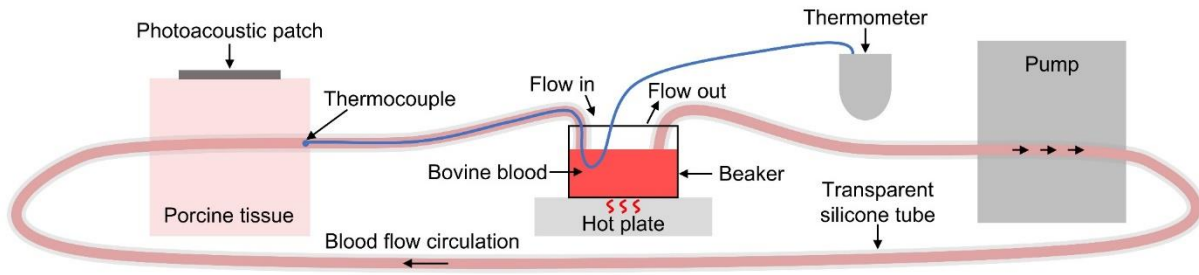


Supplementary Figure 35 | Response of the patch to dynamic temperature changes by continuously measuring warm bovine blood as they were injected into the phantom (Fig. S34). Upon injection, the temperatures of the three regions of interest (ROIs) were close to 32, 36, and 38 °C, which then quickly decreased. The measurement results were validated simultaneously by thermocouples. We injected the same kind of whole bovine blood into the three tubes using three syringes, respectively. Each syringe was filled with warm blood at different temperatures. Therefore, after injecting the blood into the tubes, the initial temperatures in the tubes are different, resulting in different temperature profiles at different moments. **a**, Photoacoustic images, and **b**, Temperature mappings captured by the photoacoustic patch at 0, 10, and 25 s after injecting warm blood into the tubes. **c-e**, Changes in temperature measured by the photoacoustic patch and the thermocouples in ROIs 1-3. The black curves are the mean values of five thermocouple measurements, and the red curves are the mean values of five photoacoustic measurements. The shades of the curves are standard deviations of the measurements. **f**, Bland-Altman plot (Supplementary Note 7) showing the statistical analysis of 600 pairs of results measured by the thermocouple and photoacoustic patch. The horizontal axis is the mean of the temperatures

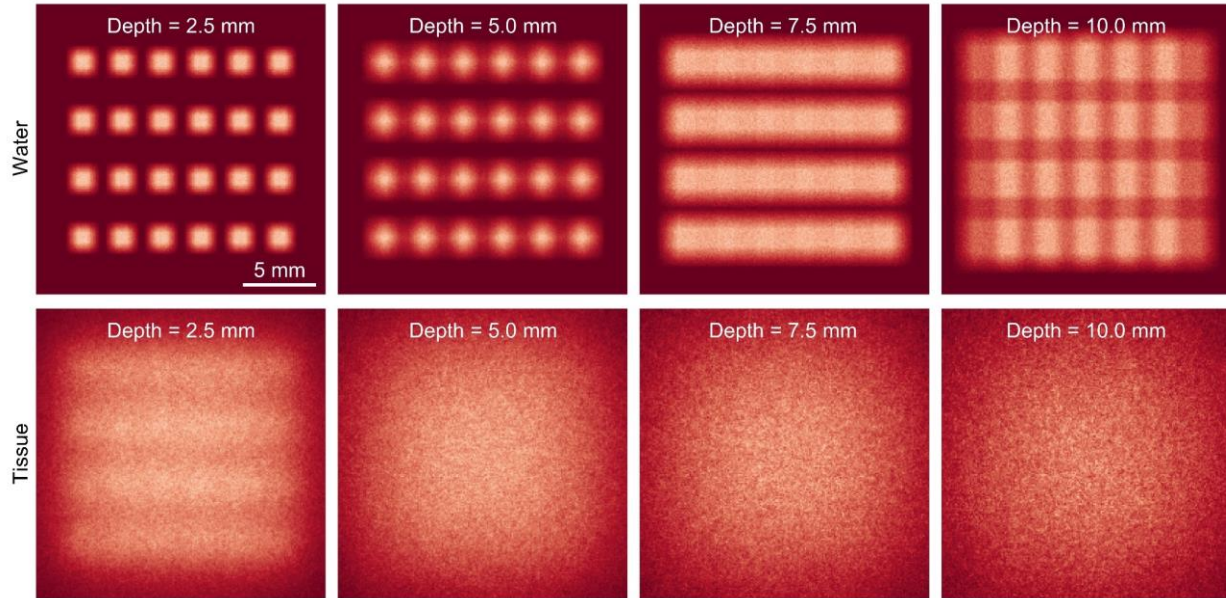
measured by the two devices, while the vertical axis is the difference between them. Bland-Altman plot analyzes the agreement between two datasets measured by two detection methods⁶⁴, which is widely used to compare a new measurement technique with the gold standard⁶⁵⁻⁶⁷. Mean defines the average value of difference. -1.96 SD (i.e., standard deviation) and $+1.96$ SD label the lower and upper limit boundaries of the 95-confidence interval in standard normal distribution. As shown, most (94.8%) of the datapoints are within ± 1.96 standard deviations difference, demonstrating the excellent agreement between the two devices with a high statistical robustness. According to our calculation, the standard deviation between the thermocouple and photoacoustic patch is about 0.7 °C, which is considered as the accuracy of the photoacoustic patch at the depth of 2 cm in *ex-vivo* porcine tissue. The high accuracy of temperature measurement benefits from the high power of laser diodes and high receiving sensitivity of ultrasound transducers. The entire patch has a pulse energy of about 0.192 mJ with a pulse duration of 200 ns. This power is close to the 0.2 mJ of a commercial LED-array-based photoacoustic imaging system^{38,91}, which has achieved *in-vivo* imaging at a depth of over 2 cm. Comparison of measured receiving sensitivity between the photoacoustic patch and commercial ultrasound probe also shows they have similar performance on the wave receiving (Fig. S22). There are many studies in the literature that have reported accuracies better than this work, such as 0.6 °C in a deep chicken¹²¹, 0.2 °C and 0.5 °C on phantom and animal using a portable photoacoustic system¹²², and a high accuracy of 0.18 °C in a photoacoustic based close-loop temperature control system¹²³. A temperature accuracy of 0.16 °C on porcine tissues has also been reported⁶⁰. Because this is the demonstration of proof-of-concept of flexible and stretchable photoacoustic patch, there is still a lot of space to improve, such as enhancing the laser energy.



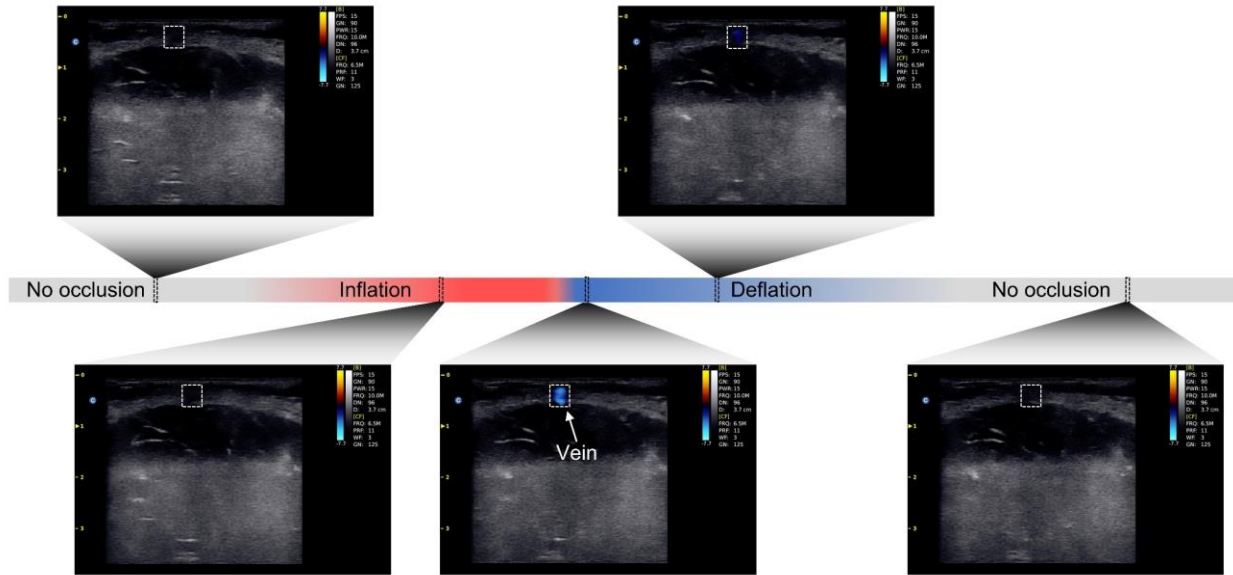
Supplementary Figure 36 | Core temperature mapping using the photoacoustic patch. We tested regions of interest (ROI) 2 (Fig. S34), filled with room temperature blood, under a changing thermal gradient created by all of the ROIs. We first injected blood at the room temperature into ROI 2. The blood in ROI 2 was static during the experiment. Then, we quickly injected warm and cold water into ROIs 1 and 3, respectively. The water flow in ROIs 1 and 3 stopped after the warm and cold water filled the tubes fully, which was achieved within 1 second. After the injection, fluids in ROIs 1, 2, and 3 all kept static. We used the photoacoustic patch to image the temperature gradient in ROI 2 created by all the ROIs. **a**, The mapping results show that the region close to ROI 1 has a much higher temperature than that near ROI 3 initially (top panel); the difference decreases rapidly with time (bottom panel). To verify the accuracy of these results, two thermocouples are placed in the ROI 2, labeled as points I and II. **b**, The temporal temperature curves measured at these two points show a strong correlation between the thermocouples and the photoacoustic patch.



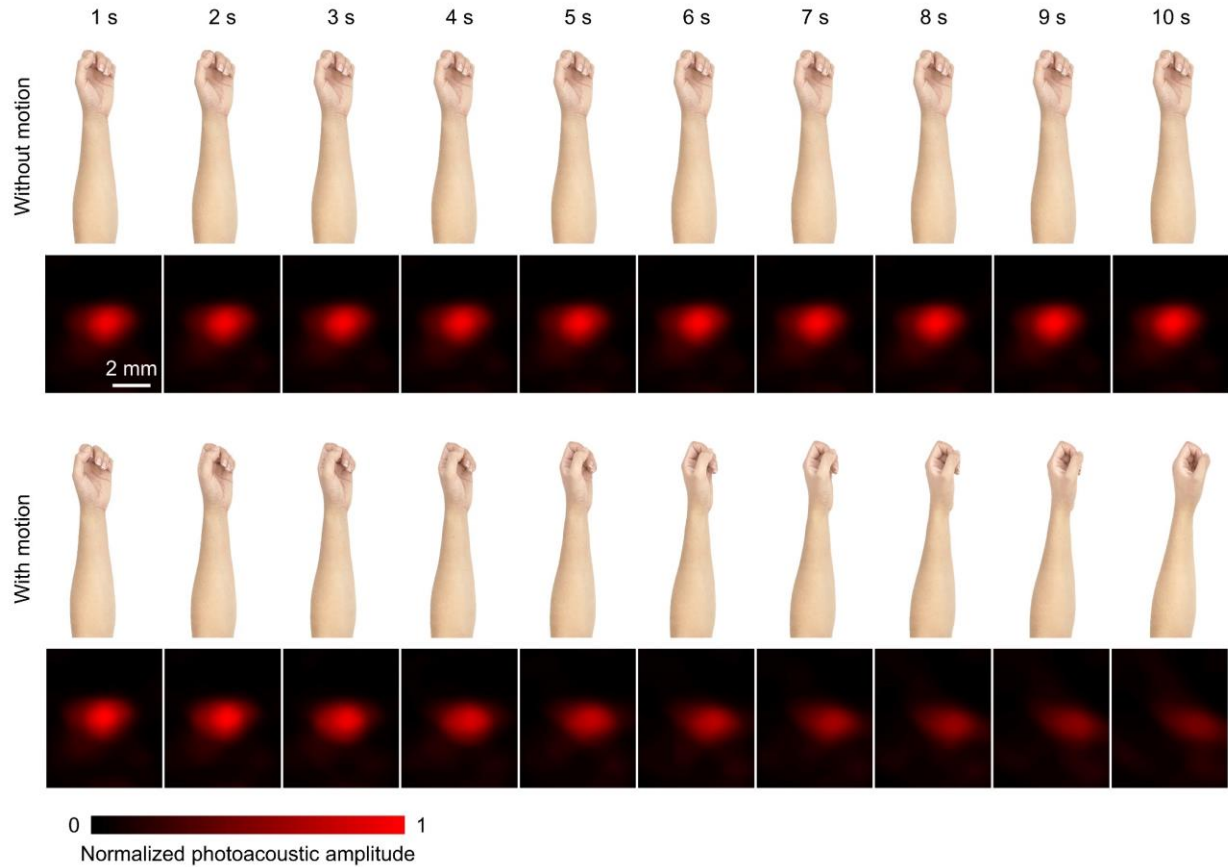
Supplementary Figure 37 | Schematic showing the experimental setup. We used a pump (Huiyu, BT300J-1A) to drive the blood to flow in a transparent silicone tube with an inner diameter of 3 mm. The rate of flow was set to be $\sim 9 \text{ mL s}^{-1}$, resulting in a blood flowing speed of $\sim 127 \text{ cm s}^{-1}$, which was higher than the blood flow velocity of most blood vessels in the human body. The two ends of the tube were immersed in a breaker containing bovine blood. The beaker was placed on a hot plate to heat the blood to different temperatures during flowing. The blood could also naturally cool down while the hot plate was turned off. A portion of the tube was embedded underneath a porcine tissue at a depth of $\sim 2 \text{ cm}$, which was measured by the photoacoustic patch. A soft thermocouple was inserted into the tube to measure the blood temperature simultaneously. The data was read by a thermometer and recorded in a laptop continuously.



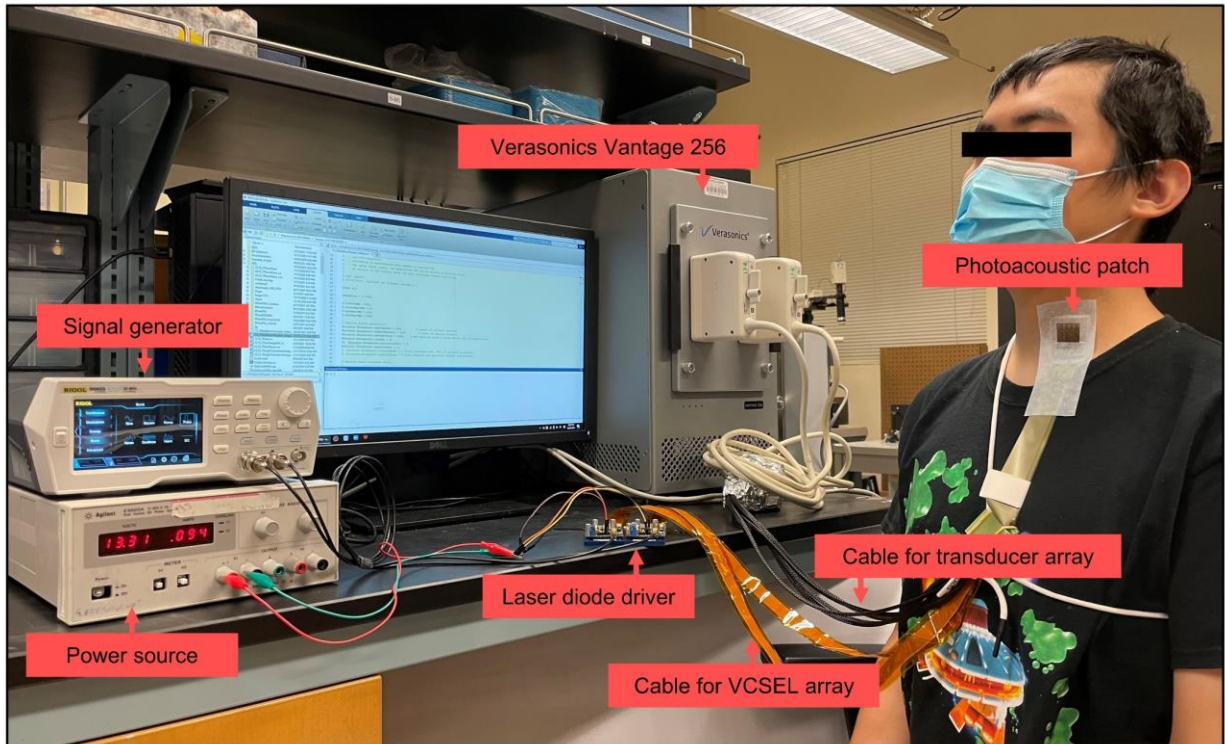
Supplementary Figure 38 | Optical distribution simulation at different depths in the water and tissue performed in an open-source MATLAB toolbox — MCmatlab. For conventional photoacoustic imaging systems, the transducer array is usually immersed in water^{9,10}, which serves as the acoustic coupling media between the array and tissue. Ultrasound gel can be also applied as an alternative acoustic coupling media. Water and ultrasound gel both have high optical transparency and low scattering coefficients, which means they have low diffusion capability. In this case, if the optical beam illuminated from an optical fiber or a prism is not uniform, a long stand-off distance (about 10 mm) is usually required to make sure the optical beam reach the tissue skin as uniform as possible. To decrease this stand-off distance or expand the illumination area, an optical diffuser^{9,10} can be inserted between the optical source and the tissue. The results in the figure are all normalized individually to show the beam pattern. When the photoacoustic patch illuminates water, the first row presents the distribution of optical intensity at different depths. The absorption coefficient μ_a , scattering coefficient μ_s , Henyey–Greenstein scattering anisotropy factor g , and refractive index n are set as 0.00036 cm^{-1} , 10 cm^{-1} , 1, and 1.3, respectively. It is obvious that the optical beam is not uniform. This explains why conventional photoacoustic imaging systems need a long stand-off to achieve a uniform beam pattern on the skin surface. The second row shows the optical distribution at different depths in the tissue. The absorption coefficient μ_a , scattering coefficient μ_s , Henyey–Greenstein scattering anisotropy factor g , and refractive index n are set as 0.1 cm^{-1} , 85 cm^{-1} , 0.9, and 1.3, respectively. The results show that biological tissue has strong diffusion effect on the laser beam. There is a stand-off distance for our patch, which is less than 2.5 mm. The distribution of optical pattern is even more uniform at the depth of 2.5 mm in the tissue than that at the depth of 10 mm in the water. In our studies, we are interested in deep tissues ($>5 \text{ mm}$), beyond which the optical distribution is very uniform. Except for the imaging of superficial veins in the hand, foot, thigh, and forearm, all the other experiments are not affected by the stand-off distance. When detecting the superficial veins, a 1 cm-thick gelatin phantom was added between the patch and forearm to compensate for this stand-off distance.



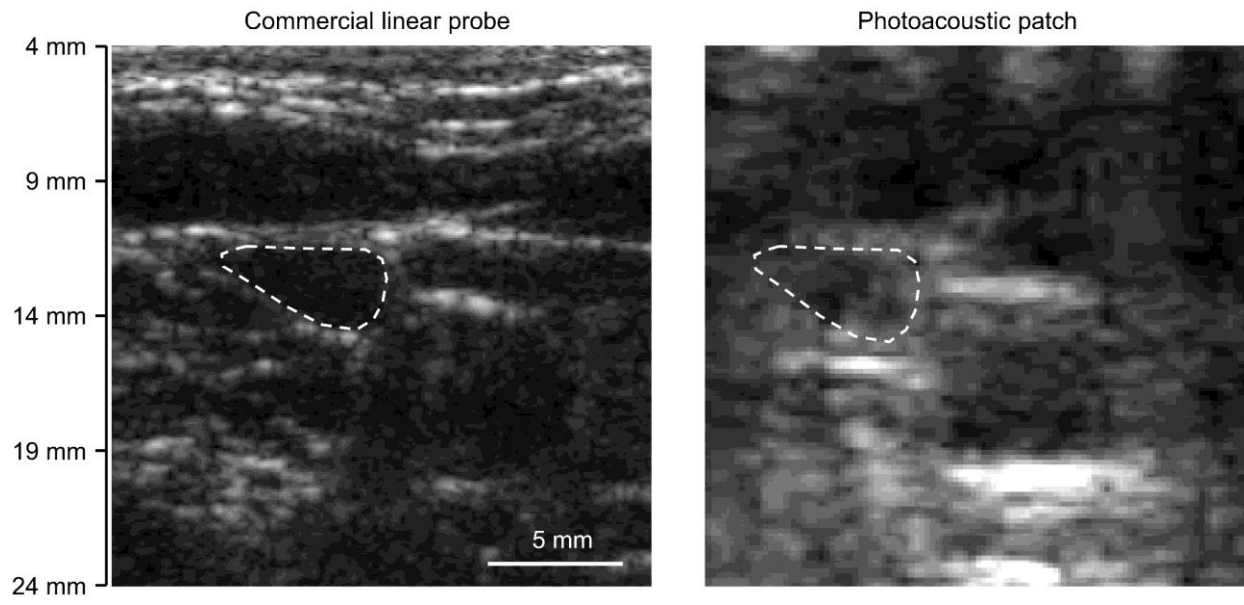
Supplementary Figure 39 | Ultrasound B-mode and color flow Doppler images of veins in the forearm acquired by a commercial ultrasound system (Chison ECO5) during venous occlusion test. The working frequency was 10 MHz. The dual mode images — ultrasound B-mode and color Doppler image, at different stages of venous occlusion test are shown in this figure. Due to the low sensitivity of ultrasound Doppler to slow blood flow, we used a cuff to induce ischemia followed by sudden release of the cuff to increase the blood flow in the vein. Five images were measured before occlusion, during inflation (~ 90 mmHg), right after deflation, after deflation, and no occlusion. Blood flow is undetectable in the first, second, and fifth images. The third image shows the moment immediately after the cuff was released. At that moment, the blood flow was the fastest and thus detected. And the blood flow quickly vanished in the image because the blood velocity dropped fast. The ultrasound Doppler detection of veins in the forearm shows low sensitivity because of the slow blood flow, which is very common for small blood vessels¹²⁴. To the contrary, the photoacoustic patch achieves high-contrast photoacoustic images of the veins.



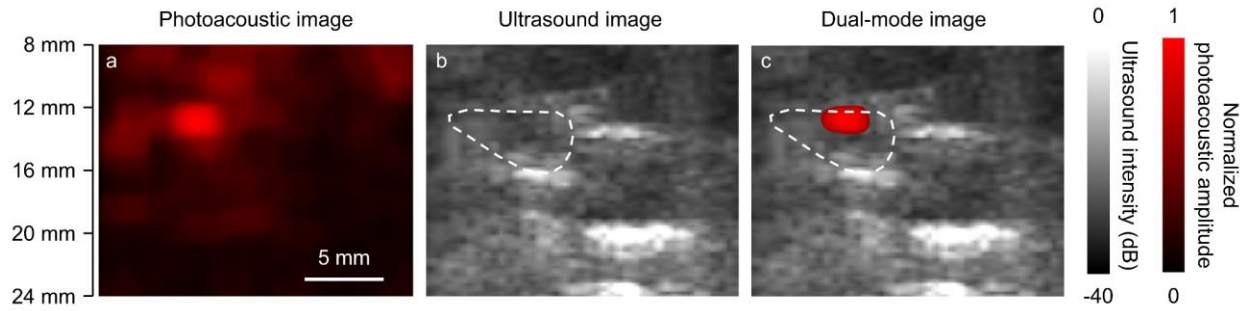
Supplementary Figure 40 | Photoacoustic imaging artifact caused by forearm movement. The figure shows two measurements of the vein in the forearm, which includes 10 frames of images of the vein corresponding to static forearm and moving forearm. For the situation without motion, the images of the blood vessel are stable. However, as displayed in the second row, rotating the forearm caused the displacement and distortion of the blood vessel. During the measurements of veins in this study, the volunteer kept the arm and neck still to decrease the influence of motion.



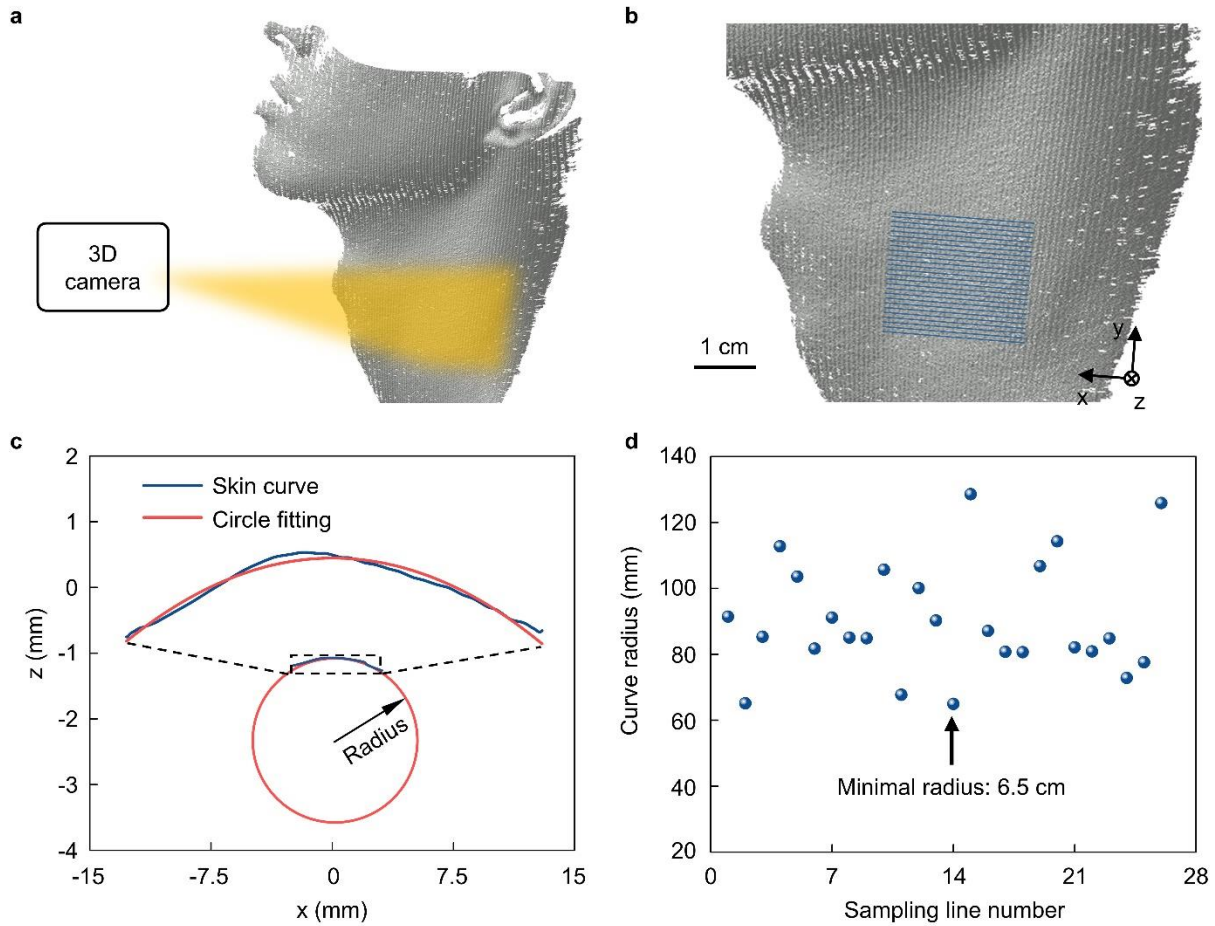
Supplementary Figure 41 | Photos of the measurement system, including the photoacoustic patch, driving circuits of the VCSEL array, and the Verasonics system. The key components have been labelled.



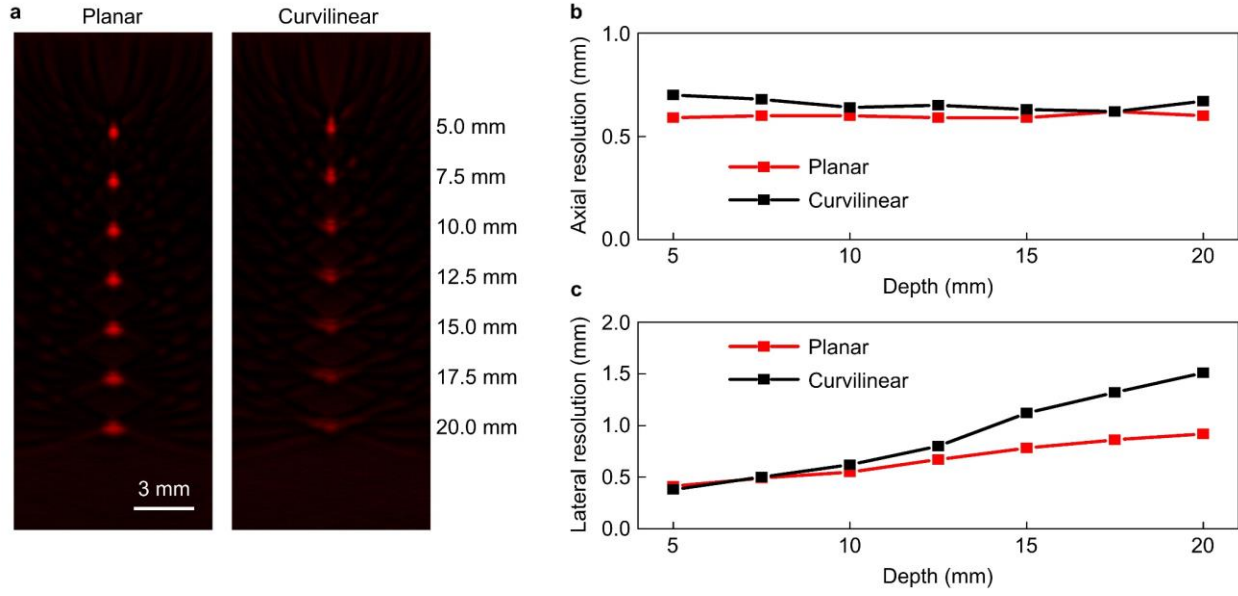
Supplementary Figure 42 | Comparison of ultrasound B-mode images acquired by a commercial probe and the photoacoustic patch. The commercial probe (Verasonics, L11-5v) has better ultrasound imaging quality than the photoacoustic patch because of the higher frequency (8 MHz) and more transducer elements (128 elements).



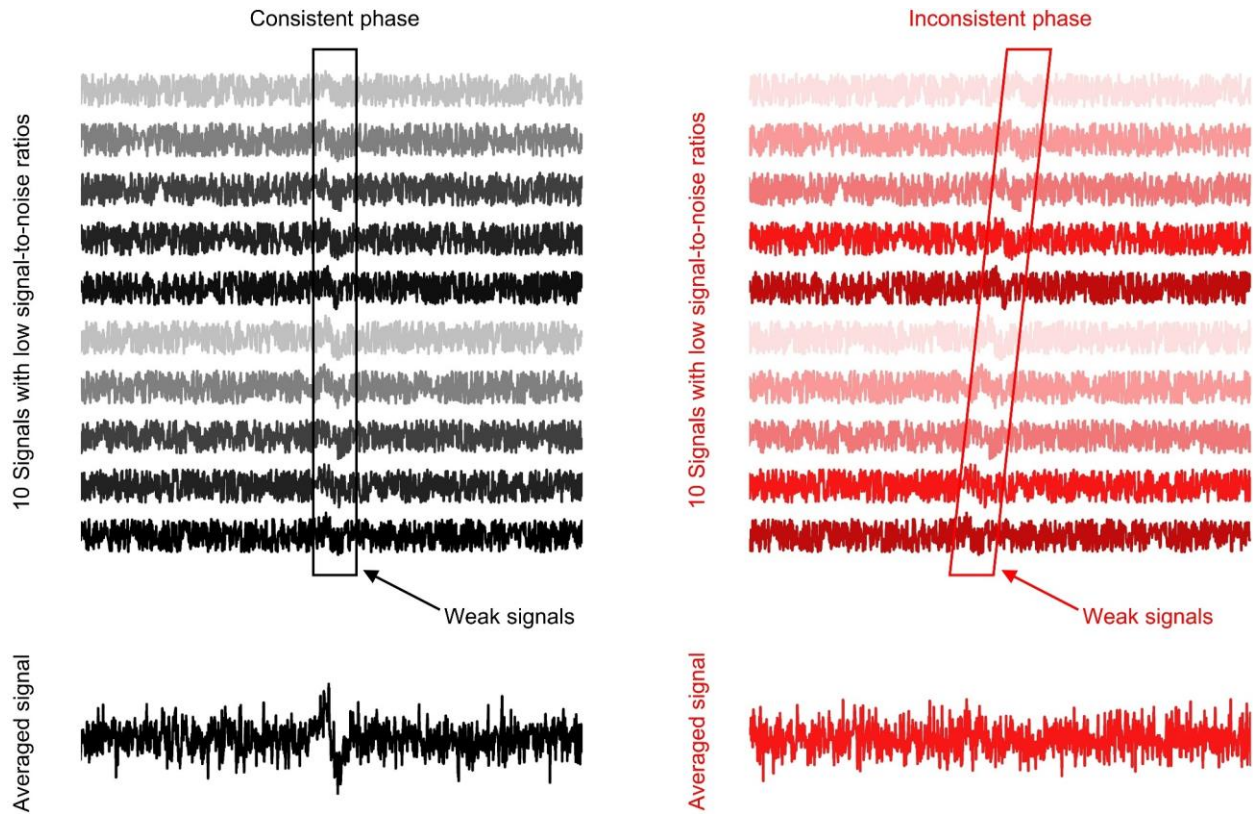
Supplementary Figure 43 | Dual-mode images of the internal jugular vein acquired by photoacoustic patch. a, One typical 2D photoacoustic image of the internal jugular vein. **b**, Corresponding ultrasound B-mode image. **c**, Co-registered ultrasound image and photoacoustic image, where only the photoacoustic amplitude larger than 0.5 was displayed. Even though there are some areas introduce photoacoustic contrasts, the internal jugular vein has the highest signal amplitude.



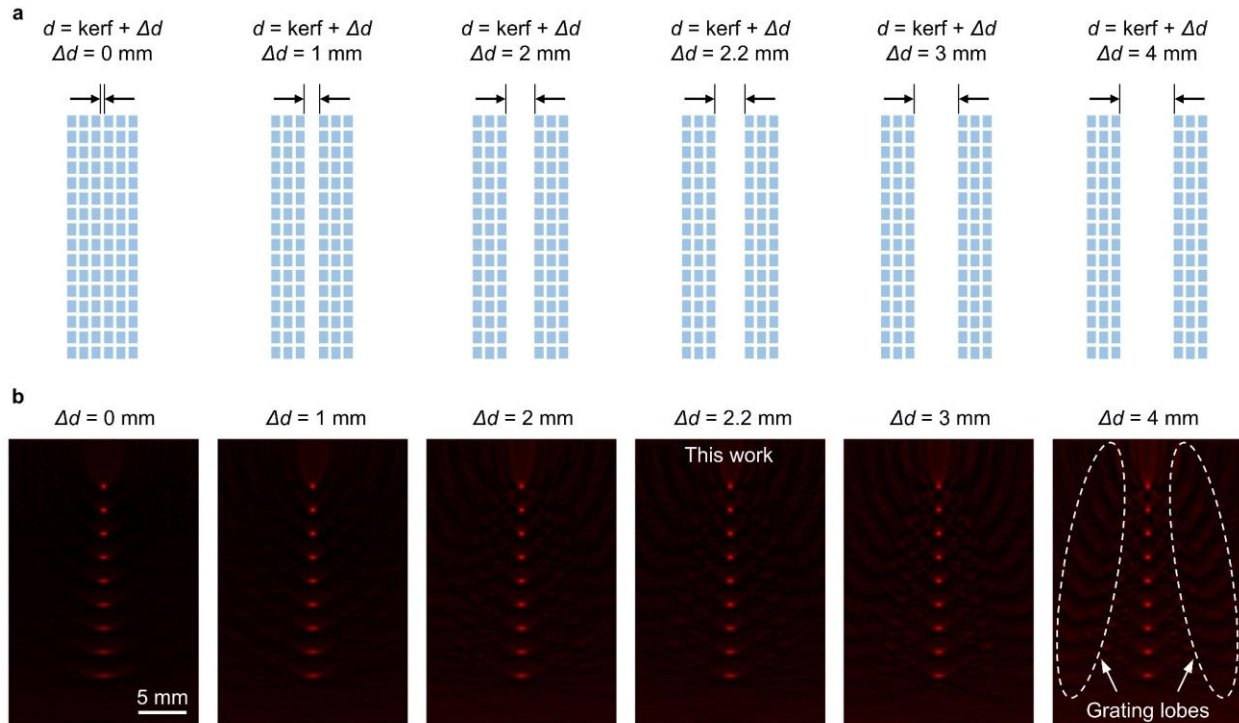
Supplementary Figure 44 | Characterization of skin curvatures by a 3D camera. a, Schematics of scanning the neck with a 3D camera. **b,** Extracting curves of the scanned skin surface. The 26 intersection lines are labeled in blue. **c,** Determining radius of skin curvature by circle fitting. **d,** Measured curvature radii at 26 positions on the subject. The smallest radius is found to be 6.5 cm, which is used in this work to evaluate the influence of the skin curvature on the imaging performance of the soft photoacoustic patch.



Supplementary Figure 45 | Influence of the skin curvature on the imaging results. a, Imaging results of point sources at different depths when the soft photoacoustic patch is placed on planar (left) and curvilinear (right) surfaces. Changes in **b**, the axial and **c**, the lateral resolutions at different depths when the patch is placed on the planar and curvilinear surfaces, respectively.

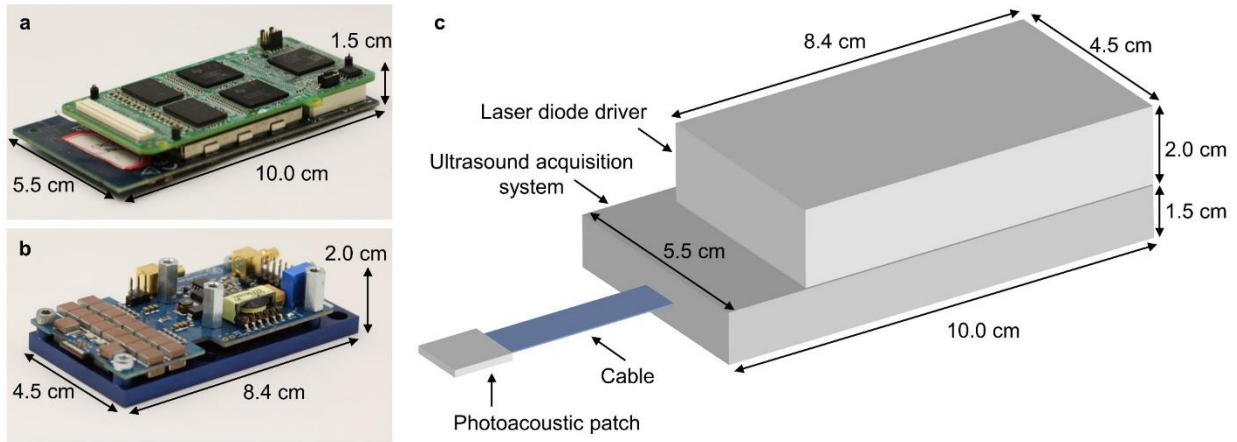


Supplementary Figure 46 | Comparison of averaged signals between consistent and inconsistent phases. A relatively static tissue yields a consistent phase in the photoacoustic signals, which can get a high signal-to-noise ratio after signal averaging. A dynamic tissue will generate inconsistent phases, resulting in a reduced signal-to-noise ratio after signal averaging.



Supplementary Figure 47 | Influence of the VCSEL chip size on the imaging performance.

Photoacoustic imaging simulation is performed in an open-source MATLAB toolbox — *k*-Wave. **a**, Schematics showing larger VCSEL chips lead to increased distances between the transducers. Δd is defined as the extra distance caused by VCSEL chips between every three columns of ultrasound transducers. **b**, Simulated reconstructed images with stronger intensities of grating lobes at increased distances between the transducers. For case $\Delta d = 0$ mm, the distance of each two ultrasound transducers (i.e., the pitch) is 0.8 mm, close to the wavelength at 2 MHz. The photoacoustic image shows weak grating lobes. For the other five cases, the effective pitch increases, which enhances grating lobes. However, the amplitudes of grating lobes are still much weaker than the main lobes. Furthermore, the lateral resolution is improved as the effective pitch dimension increases because the aperture of the array is increased. This Figure is correlated to Supplementary Figure 4, emphasizing the influence of VCSEL chip size.



Supplementary Figure 48 | Portable photoacoustic device. The main reason why the current testing system is bulky is that we used a bulky ultrasound research platform (Verasonics system) to acquire photoacoustic signals. Verasonics system also consumes the most power in the entire device. This system is powerful but has many redundant functions that are not necessary for our applications, such as ultrasound wave transmission, high intensity focused ultrasound. The current photoacoustic patch is connected with a high-power laser diode driver and data acquisition system through some cables. Because one coaxial cable for ultrasound signal receiving only has 60 channels, we had to use multiple coaxial cables to connect all of the 240 transducer elements. Alternatively, we can use one coaxial cable containing 256 channels to reduce the number of cables. Therefore, we can keep only two cables connected with the backend controlling system, one for laser diode driving and the other for data acquisition. It is highly possible to replace the current bulky backend system with a handheld backend controlling system. The number of cables will be greatly reduced. The photoacoustic patch, including the laser diodes and ultrasound transducers, can be connected with the portable device with one customized cable. In recent years, portable ultrasound systems with ultra-compact sizes have been developed for point-of-care uses. **a**, A typical portable system developed by Texas Instruments¹²⁵, which has a size of $\sim 10.0 \text{ cm} \times 5.5 \text{ cm} \times 1.5 \text{ cm}$. This system can replace the bulky Verasonics system to record photoacoustic signals. In addition, this system has low power consumption of $\sim 2.5 \text{ W}$ ¹²⁵, which can be powered by a USB cable plugged into a laptop. **b**, The laser diode driver used in this work has a compact size of $\sim 8.4 \text{ cm} \times 4.5 \text{ cm} \times 2.0 \text{ cm}$. The power consumption of the driver is less than 10 W when driving the laser diodes at a pulse repetition rate of 3 kHz. Furthermore, the power consumption is tunable and can be further cut down by reducing the laser pulse width, pulse repetition rate, and imaging frame rate. For example, assuming decreasing the imaging frame rate from 1 Hz to 0.5 Hz, the laser diode driver power consumption can be theoretically reduced by $\sim 50\%$, i.e., $< 5 \text{ W}$ of total power consumption. **c**, A schematic of handheld photoacoustic device with possible dimensions that are predicted based on existing electrical circuits. The power consumption of such a system can be reduced to be in the range of several Watts.

	Wearable	Long-term continuous	Noninvasive	Detection depth	Spatial resolution	Citations
Magnetic Resonance Imaging (MRI)	No	No	Yes	>10 cm	~1.5 mm	1
Positron Emission Tomography (PET)	No	No	Yes	>10 cm	~3 mm	3
Fluorescence imaging	No	No	Yes	~3 mm	~4 μm	5
Optical Coherence Tomography (OCT)	No	No	Yes	<2 mm	~1–10 μm	7
Bulky photoacoustic imaging system	No	No	Yes	>4 cm	<0.25 mm	9,10
Electrochemical soft electronics	Yes	Yes	Yes	~3 mm	N/A	11
Optical soft electronics	Yes	Yes	Yes	<3 mm	N/A	12
Photoacoustic patch	Yes	Yes	Yes	>2 cm	~0.7 mm	This work

Supplementary Table 1 | Comparison between different methods for biomolecular detection.

In comparison to existing wearable electronics, the photoacoustic patch in this work realizes non-invasive 3D mapping of biomolecules in deep tissues. This technology not only achieves imaging resolutions and detection depth comparable with the conventional bulky systems, but also has compact size and conformal mechanical properties, which are suitable for long-term monitoring.

Type	Pulse energy	Pulse repetition rate	Imaging frame rate	Number of data averaging	Size of ultrasound probe	Size of laser source	Citation
Laser	~20 mJ cm ⁻² @ 680-950 nm	100 Hz	100 Hz (3D)	0	Spherical matrix array, cylindrical shape Diameter ~ 70 mm, Thickness > 80 mm	Not described.	84
Laser	23 mJ cm ⁻² @ 1064 nm 19 mJ cm ⁻² @ 694 nm	10 Hz 1 Hz	0.5 Hz (3D)	0	Hemispherical matrix array Diameter = 260 mm	Not described.	85
Laser	15 mJ cm ⁻² @ 532 nm, 27 mJ cm ⁻² @ 1064 nm	10 Hz	10 Hz (2D) ~0.025 Hz (3D)	0	ATL L7-4, commercial linear probe	Optical head: 775 × 178 × 190 mm Power supply: 622 × 282 × 508 mm	86
Laser	20 mJ cm ⁻² @ 730-900 nm 50 mJ cm ⁻² @ 1064 nm	10 Hz	10 Hz (3D)	0	Spherical matrix array with a radius of 40 mm, thickness > 80 mm	Integrated unit: 483 × 762 × 1092 mm	87
Laser	6.25 ~ 12.5 mJ cm ⁻² @ 1064 nm 20 mJ cm ⁻² @ 1064 nm	10 Hz	10 Hz (2D) ~1/15 Hz (3D)	0	Ring transducer array, Diameter = 220 mm, Elevation size = 5 mm	Optical head: 1173 × 508 × 120 mm Power supply: 770 × 640 × 757 mm	9,126
Laser	10 mJ cm ⁻² @ 610 nm	10 Hz	10 Hz (2D)	0	Ring transducer array, Diameter = 100 mm, Elevation size = 20 mm	Not described.	88
Laser	2 mJ cm ⁻² @ 630 nm 2 mJ cm ⁻² @ 780 nm 30 mJ cm ⁻² @ 780 nm	20 Hz	20 Hz (2D)	0	Ring transducer array, Diameter = 100 mm, Elevation size = 20 mm	Optical head: 800 × 450 × 150 mm Power supply: 446 × 449 × 177 mm Cooling system: 446 × 449 × 266 mm Control unit: 446 × 449 × 133 mm	89,127
Laser	125 mJ cm ⁻² @ 532 nm	10 Hz	10 Hz (2D)	0	ATL L7-4, commercial linear probe	Optical head: 147 × 526 × 125 mm Harmonic modules: 99 × 123 × 125 mm Power supply: 513 × 507 × 283 mm	128
Laser	12.7 mJ cm ⁻² @ 1064 nm	20 Hz	20 Hz (2D)	0	Ring transducer array, Diameter = 80 mm, Elevation size = 14 mm	Optical head: 735 × 179 × 162 mm Power supply: 647 × 334 × 554 mm	129
Laser	5 mJ cm ⁻² @ 760 nm	20 Hz	1 Hz (2D)	10	Ring transducer array, Diameter = 100 mm	Not described.	90
LED	10 μJ cm ⁻² @ 850 nm 2 μJ cm ⁻² @ 690 nm	1~4 kHz	0.15~30 Hz (2D)	32~25600	LEDs and ultrasound probe integrated. Ultrasound probe: Linear array, ~ 40 × 10 × 80 mm Optical head: 12.4 × 86.5 × 10.2 mm × 2 LED driver: -	91	
LED	< 200 μJ @ 850 nm < 80 μJ @ 690 nm	4 kHz, 16 kHz	10 Hz, 500 Hz (2D)	384 / 32	LEDs and ultrasound probe integrated. Ultrasound probe: Linear array, ~ 40 × 10 × 80 mm Optical head: 12.4 × 86.5 × 10.2 mm × 2 LED driver: -	38	
LED	1.8 μJ @ 460 nm; 0.4 μJ @ 530 nm 1.7 μJ @ 590 nm; 2.7 μJ @ 620 nm 9 μJ @ 623nm	500 Hz	0.05 Hz 0.1 Hz (2D)	5000 / 10000	Cylindrical single transducer, Diameter = 10 mm Length: -	Optical head (LED): 11 × 10 × 5.3 mm 9 × 9 × 5.4 mm LED driver: 51 × 82.5 × 13 mm	92
Laser diode	24 μJ / 184 μJ @ 905 nm	20 kHz / 2 kHz	4 Hz / 0.4 Hz (2D)	5000	Not described.	Not described.	31

Laser diode	0.56 mJ (1.5 mJ cm ⁻²) @ 805 nm	210 Hz	10 Hz (2D)	20	LEDs and ultrasound probe integrated. Size not mentioned. Larger than a commercial linear probe.	93
Laser diode	1.4 mJ (0.28 mJ cm ⁻²) @ 803 nm	7 kHz	1/3 Hz (2D)	42	Cylindrical single transducer, Diameter = 10 mm Length: -	Optical head: 137 × 76 × 38 mm 94
Laser diode	~192 μJ @ 850 nm	3 kHz	1 Hz (2D, offline 3D)	3000	Laser diodes and ultrasound transducer integrated. Overall footprint: 20 × 16 × 1.2 mm	This work

Supplementary Table 2 | Comparison between the soft photoacoustic patch in this work and other photoacoustic systems. Specifications of typical photoacoustic tomography systems include laser source type, pulse energy, pulse repetition rate, imaging frame rate, number of data averaging, size of ultrasound probe, and size of laser source. In the literature, PAT systems equipped with high-power lasers usually describe the laser energy per area on the tissue surface, while low-cost PAT systems using laser diodes or LEDs usually describe the pulse energy. The maximum pulse energy for the first kind is in the range from tens of millijoules to several joules by referring to the datasheets of the lasers.

	Wearable	Long-term continuous	Response time	Depth	Spatial mapping	Citations
Magnetic Resonance Imaging (MRI)	No	No	<1 s	>10 cm	Yes	53
Resistance temperature detectors and thermistors	Yes	Yes	~1 s	Skin surface	Yes	50-52
Zero Heat flux model	Yes	Yes	~180 s	~1 cm	No	58
Dual Heat flux model	Yes	Yes	>447 s	9.2 mm	No	27
Photoacoustic patch	Yes	Yes	~1 s	>2 cm	Yes	This work

Supplementary Table 3 | Comparison of different noninvasive temperature measurement techniques. The photoacoustic patch can noninvasively map the core temperature with high accuracy and fast response.

Equipment name	Company	model
Ultrasound Research platform	Verasonics	Vantage-256
Ultrasound transducer connector	ATL	Customized
Adapter	Verasonics	UTA-260D
Signal generator	Rigol	DG822
Power Supply	Agilent	E3620A
Laser diode driver	PicoLAS	LDP-V 240-100 V3.3
Thermometer	Omega Engineering	HH806AU
Thermocouple	Omega Engineering	SC-TT-K-30-36
ACF cable	Elform	Customized
Micro-coaxial cable	I-PEX	Customized
PCB convert board	JLC	Customized

Supplementary Table 4 | Equipment name, company name, and model of equipment in the experiments.

Material name	Company	Model
VCSEL	Ace Photonics	850nm VCSEL
Piezoelectric material	Del Piezo	1-3 PZT-5H
Ecoflex	Smooth On	00-30
Silver-Epoxy	Von Roll	3022
Copper foil	Oak-Mitsui Inc.	N/A
Polyimide	HD Microsystem	P12535
Aluminum Nitride	MARUWA	Customized
Gold	VEM	Gold sputtering target

Supplementary Table 5 | Material name, company, and model of the materials used in the experiments.

References

- 1 Uecker, M. *et al.* Real-time MRI at a resolution of 20 ms. *NMR Biomed.* **23**, 986-994 (2010).
- 2 Berger, A. How does it work?: Magnetic resonance imaging. *BMJ: British Medical Journal* **324**, 35 (2002).
- 3 Gambhir, S. S. Molecular imaging of cancer with positron emission tomography. *Nature Reviews Cancer* **2**, 683-693 (2002).
- 4 Berger, A. How does it work?: Positron emission tomography. *BMJ: British Medical Journal* **326**, 1449 (2003).
- 5 Diao, S. *et al.* Fluorescence imaging in vivo at wavelengths beyond 1500 nm. *Angew. Chem.* **127**, 14971-14975 (2015).
- 6 Huang, D. *et al.* Optical coherence tomography. *Science* **254**, 1178-1181 (1991).
- 7 Robles, F. E., Wilson, C., Grant, G. & Wax, A. Molecular imaging true-colour spectroscopic optical coherence tomography. *Nat. Photonics* **5**, 744-747 (2011).
- 8 Wang, L. V. & Hu, S. Photoacoustic tomography: in vivo imaging from organelles to organs. *science* **335**, 1458-1462 (2012).
- 9 Lin, L. *et al.* Single-breath-hold photoacoustic computed tomography of the breast. *Nat. Commun.* **9**, 1-9 (2018).
- 10 Li, L. *et al.* Single-impulse panoramic photoacoustic computed tomography of small-animal whole-body dynamics at high spatiotemporal resolution. *Nat. Biomed. Eng.* **1**, 1-11 (2017).
- 11 Gao, W. *et al.* Fully integrated wearable sensor arrays for multiplexed in situ perspiration analysis. *Nature* **529**, 509-514 (2016).
- 12 Lee, G.-H. *et al.* Multifunctional materials for implantable and wearable photonic healthcare devices. *Nature Reviews Materials* **5**, 149-165 (2020).
- 13 Lee, H. *et al.* Wearable/disposable sweat-based glucose monitoring device with multistage transdermal drug delivery module. *Science advances* **3**, e1601314 (2017).
- 14 Choi, J., Ghaffari, R., Baker, L. B. & Rogers, J. A. Skin-interfaced systems for sweat collection and analytics. *Science advances* **4**, eaar3921 (2018).
- 15 Bariya, M., Nyein, H. Y. Y. & Javey, A. Wearable sweat sensors. *Nature Electronics* **1**, 160-171 (2018).
- 16 Arakawa, T. *et al.* Mouthguard biosensor with telemetry system for monitoring of saliva glucose: A novel cavitas sensor. *Biosensors and Bioelectronics* **84**, 106-111 (2016).
- 17 Kim, J. *et al.* Wearable salivary uric acid mouthguard biosensor with integrated wireless electronics. *Biosensors and Bioelectronics* **74**, 1061-1068 (2015).
- 18 Reid, R. C., Minter, S. D. & Gale, B. K. Contact lens biofuel cell tested in a synthetic tear solution. *Biosensors and Bioelectronics* **68**, 142-148 (2015).
- 19 Park, J. *et al.* Soft, smart contact lenses with integrations of wireless circuits, glucose sensors, and displays. *Science advances* **4**, eaap9841 (2018).
- 20 Ku, M. *et al.* Smart, soft contact lens for wireless immunosensing of cortisol. *Science advances* **6**, eabb2891 (2020).
- 21 Wang, Z. *et al.* Microneedle patch for the ultrasensitive quantification of protein biomarkers in interstitial fluid. *Nature Biomedical Engineering* **5**, 64-76 (2021).

- 22 Yang, B., Fang, X. & Kong, J. In situ sampling and monitoring cell-free dna of the epstein–barr virus from dermal interstitial fluid using wearable microneedle patches. *ACS applied materials & interfaces* **11**, 38448-38458 (2019).
- 23 Boyne, M. S., Silver, D. M., Kaplan, J. & Saudek, C. D. Timing of changes in interstitial and venous blood glucose measured with a continuous subcutaneous glucose sensor. *Diabetes* **52**, 2790-2794 (2003).
- 24 Hauke, A. *et al.* Complete validation of a continuous and blood-correlated sweat biosensing device with integrated sweat stimulation. *Lab on a Chip* **18**, 3750-3759 (2018).
- 25 Fallis, W. M. Monitoring urinary bladder temperature in the intensive care unit: state of the science. *American Journal of Critical Care* **11**, 38-45 (2002).
- 26 Krizanac, D. *et al.* Femoro-iliacal artery versus pulmonary artery core temperature measurement during therapeutic hypothermia: an observational study. *Resuscitation* **84**, 805-809 (2013).
- 27 Zhang, Y. *et al.* Theoretical and experimental studies of epidermal heat flux sensors for measurements of core body temperature. *Advanced healthcare materials* **5**, 119-127 (2016).
- 28 Teunissen, L., Klewer, J., De Haan, A., De Koning, J. & Daanen, H. Non-invasive continuous core temperature measurement by zero heat flux. *Physiological measurement* **32**, 559 (2011).
- 29 Liu, S. *et al.* Toward wearable healthcare: A miniaturized 3d imager with coherent frequency-domain photoacoustics. *IEEE transactions on biomedical circuits and systems* **13**, 1417-1424 (2019).
- 30 Kalva, S. K., Upputuri, P. K. & Pramanik, M. High-speed, low-cost, pulsed-laser-diode-based second-generation desktop photoacoustic tomography system. *Optics Letters* **44**, 81-84 (2019).
- 31 Allen, T. J. & Beard, P. C. Pulsed near-infrared laser diode excitation system for biomedical photoacoustic imaging. *Optics letters* **31**, 3462-3464 (2006).
- 32 Singh, M. K. A. & Steenbergen, W. Photoacoustic-guided focused ultrasound (PAFUSion) for identifying reflection artifacts in photoacoustic imaging. *Photoacoustics* **3**, 123-131 (2015).
- 33 Xia, W. *et al.* Handheld real-time LED-based photoacoustic and ultrasound imaging system for accurate visualization of clinical metal needles and superficial vasculature to guide minimally invasive procedures. *Sensors* **18**, 1394 (2018).
- 34 Jo, J. *et al.* Detecting joint inflammation by an LED-based photoacoustic imaging system: a feasibility study. *Journal of biomedical optics* **23**, 110501 (2018).
- 35 Zhang, H. F., Maslov, K., Stoica, G. & Wang, L. V. Functional photoacoustic microscopy for high-resolution and noninvasive in vivo imaging. *Nature biotechnology* **24**, 848-851 (2006).
- 36 Yao, J. *et al.* High-speed label-free functional photoacoustic microscopy of mouse brain in action. *Nat. Methods* **12**, 407-410 (2015).
- 37 Liu, S. *et al.* Handheld photoacoustic imager for theranostics in 3D. *IEEE Trans. Med. Imaging* **38**, 2037-2046 (2019).
- 38 Zhu, Y. *et al.* Light emitting diodes based photoacoustic imaging and potential clinical applications. *Scientific reports* **8**, 1-12 (2018).
- 39 Manwar, R., Zafar, M. & Xu, Q. Signal and Image Processing in Biomedical Photoacoustic Imaging: A Review. *Optics* **2**, 1-24 (2021).

- 40 Singh, M. K. A., Sato, N., Ichihashi, F. & Sankai, Y. LED-Based Photoacoustic Imaging. *Springer* **10**, 978-981 (2020).
- 41 Smith, A. M., Mancini, M. C. & Nie, S. Second window for in vivo imaging. *Nature nanotechnology* **4**, 710-711 (2009).
- 42 Sordillo, L. A., Pu, Y., Pratavieira, S., Budansky, Y. & Alfano, R. R. Deep optical imaging of tissue using the second and third near-infrared spectral windows. *Journal of biomedical optics* **19**, 056004 (2014).
- 43 Upputuri, P. K. & Pramanik, M. Photoacoustic imaging in the second near-infrared window: a review. *J. Biomed. Opt.* **24**, 040901 (2019).
- 44 Chen, Y.-S., Zhao, Y., Yoon, S. J., Gambhir, S. S. & Emelianov, S. Miniature gold nanorods for photoacoustic molecular imaging in the second near-infrared optical window. *Nat. Nanotechnol.* **14**, 465-472 (2019).
- 45 Lyu, Y., Li, J. & Pu, K. Second Near -Infrared Absorbing Agents for Photoacoustic Imaging and Photothermal Therapy. *Small Methods* **3**, 1900553 (2019).
- 46 Sordillo, L. A. *et al.* in *Optical Biopsy XII*. 89400V (International Society for Optics and Photonics).
- 47 Fulbrook, P. Core body temperature measurement: a comparison of axilla, tympanic membrane and pulmonary artery blood temperature. *Intensive and Critical Care Nursing* **13**, 266-272 (1997).
- 48 Shi, C. *et al.* Application of a sub-0.1-mm³ implantable mote for in vivo real-time wireless temperature sensing. *Sci. Adv.* **7**, eabf6312 (2021).
- 49 Shin, J. *et al.* Bioresorbable optical sensor systems for monitoring of intracranial pressure and temperature. *Sci. Adv.* **5**, eaaw1899 (2019).
- 50 Han, S. *et al.* Battery-free, wireless sensors for full-body pressure and temperature mapping. *Sci. Transl. Med.* **10** (2018).
- 51 You, I. *et al.* Artificial multimodal receptors based on ion relaxation dynamics. *Science* **370**, 961-965 (2020).
- 52 *Thermocouple Response Time*, <<https://www.omega.com/en-us/resources/thermocouples-response-time>> (2019).
- 53 Denis de Senneville, B., Quesson, B. & Moonen, C. T. Magnetic resonance temperature imaging. *Int. J. Hyperthermia* **21**, 515-531 (2005).
- 54 Eshraghi, Y. *et al.* An evaluation of a zero-heat-flux cutaneous thermometer in cardiac surgical patients. *Anesthesia & Analgesia* **119**, 543-549 (2014).
- 55 Huang, M., Tamura, T., Tang, Z., Chen, W. & Kanaya, S. A wearable thermometry for core body temperature measurement and its experimental verification. *IEEE journal of biomedical and health informatics* **21**, 708-714 (2016).
- 56 Kitamura, K.-I., Zhu, X., Chen, W. & Nemoto, T. Development of a new method for the noninvasive measurement of deep body temperature without a heater. *Med. Eng. Phys.* **32**, 1-6 (2010).
- 57 Yamakage, M. & Namiki, A. Deep temperature monitoring using a zero-heat-flow method. *J. Anesth.* **17**, 108-115 (2003).
- 58 Pesonen, E. *et al.* The focus of temperature monitoring with zero-heat-flux technology (3M Bair-Hugger): a clinical study with patients undergoing craniotomy. *J. Clin. Monit. Comput.* **33**, 917-923 (2019).
- 59 Zhou, Y. *et al.* Thermal memory based photoacoustic imaging of temperature. *Optica* **6**, 198-205 (2019).

- 60 Shah, J. *et al.* Photoacoustic imaging and temperature measurement for photothermal cancer therapy. *J. Biomed. Opt.* **13**, 034024 (2008).
- 61 Alaeian, M. & Orlande, H. R. B. Inverse photoacoustic technique for parameter and temperature estimation in tissues. *Heat Transfer Engineering* **38**, 1573-1594 (2017).
- 62 Wu, X., Sanders, J. L., Stephens, D. N. & Oralkan, Ö. in *2016 38th Annual International Conference of the IEEE Engineering in Medicine and Biology Society (EMBC)*. 3235-3238 (IEEE).
- 63 Duck, F. A. *Physical properties of tissues: a comprehensive reference book*. (Academic press, 2013).
- 64 Dewitte, K., Fierens, C., Stockl, D. & Thienpont, L. M. Application of the Bland–Altman plot for interpretation of method-comparison studies: a critical investigation of its practice. *Clinical chemistry* **48**, 799-801 (2002).
- 65 Lee, K. *et al.* Mechano-acoustic sensing of physiological processes and body motions via a soft wireless device placed at the suprasternal notch. *Nature biomedical engineering* **4**, 148-158 (2020).
- 66 Chung, H. U. *et al.* Skin-interfaced biosensors for advanced wireless physiological monitoring in neonatal and pediatric intensive-care units. *Nature medicine* **26**, 418-429 (2020).
- 67 Chung, H. U. *et al.* Binodal, wireless epidermal electronic systems with in-sensor analytics for neonatal intensive care. *Science* **363** (2019).
- 68 Song, Z., Ding, H., Li, J. & Pu, H. Circular curve-fitting method for field surveying data with correlated noise. *J. Surv. Eng.* **144**, 04018010 (2018).
- 69 Treeby, B. E. & Cox, B. T. k-Wave: MATLAB toolbox for the simulation and reconstruction of photoacoustic wave fields. *J. Biomed. Opt.* **15**, 021314 (2010).
- 70 Hai, P. *et al.* Label-free high-throughput photoacoustic tomography of suspected circulating melanoma tumor cells in patients in vivo. *Journal of biomedical optics* **25**, 036002 (2020).
- 71 Chaffer, C. L. & Weinberg, R. A. A perspective on cancer cell metastasis. *science* **331**, 1559-1564 (2011).
- 72 Wang, Y. *et al.* Fiber-laser-based photoacoustic microscopy and melanoma cell detection. *Journal of biomedical optics* **16**, 011014 (2011).
- 73 He, Y. *et al.* In vivo label-free photoacoustic flow cytography and on-the-spot laser killing of single circulating melanoma cells. *Scientific reports* **6**, 1-8 (2016).
- 74 Zhang, R. *et al.* Noninvasive photoacoustic measurement of glucose by data fusion. *Analyst* **142**, 2892-2896 (2017).
- 75 Pleitez, M. A. *et al.* In vivo noninvasive monitoring of glucose concentration in human epidermis by mid-infrared pulsed photoacoustic spectroscopy. *Analytical chemistry* **85**, 1013-1020 (2013).
- 76 Sim, J. Y., Ahn, C.-G., Jeong, E.-J. & Kim, B. K. In vivo microscopic photoacoustic spectroscopy for non-invasive glucose monitoring invulnerable to skin secretion products. *Scientific reports* **8**, 1-11 (2018).
- 77 Zhang, C., Zhang, Y. S., Yao, D.-K., Xia, Y. & Wang, L. V. Label-free photoacoustic microscopy of cytochromes. *Journal of biomedical optics* **18**, 020504 (2013).
- 78 Zhang, C., Zhang, Y., Yao, D.-K., Xia, Y. & Wang, L. V. in *Photons Plus Ultrasound: Imaging and Sensing 2012*. 82231W (International Society for Optics and Photonics).

- 79 Yang, L. *et al.* ICG - Conjugated and 125I - Labeled Polymeric Micelles with High Biosafety for Multimodality Imaging-Guided Photothermal Therapy of Tumors. *Advanced healthcare materials* **9**, 1901616 (2020).
- 80 Alander, J. T. *et al.* A review of indocyanine green fluorescent imaging in surgery. *International journal of biomedical imaging* **2012** (2012).
- 81 Lutzweiler, C., Meier, R., Rummeny, E., Ntziachristos, V. & Razansky, D. Real-time optoacoustic tomography of indocyanine green perfusion and oxygenation parameters in human finger vasculature. *Optics letters* **39**, 4061-4064 (2014).
- 82 Stoffels, I. *et al.* Metastatic status of sentinel lymph nodes in melanoma determined noninvasively with multispectral optoacoustic imaging. *Science translational medicine* **7**, 317ra199-317ra199 (2015).
- 83 Stylogiannis, A. *et al.* Continuous wave laser diodes enable fast optoacoustic imaging. *Photoacoustics* **9**, 31-38 (2018).
- 84 Deán-Ben, X. L., Fehm, T. F., Ford, S. J., Gottschalk, S. & Razansky, D. Spiral volumetric optoacoustic tomography visualizes multi-scale dynamics in mice. *Light: Science & Applications* **6**, e16247-e16247 (2017).
- 85 Na, S. *et al.* Massively parallel functional photoacoustic computed tomography of the human brain. *Nature Biomedical Engineering* **6**, 584-592 (2022).
- 86 Wang, Y., Wang, D., Hubbell, R. & Xia, J. Second generation slit-based photoacoustic tomography system for vascular imaging in human. *Journal of biophotonics* **10**, 799-804 (2017).
- 87 Ivankovic, I., Merčep, E., Schmedt, C.-G., Deán-Ben, X. L. & Razansky, D. Real-time volumetric assessment of the human carotid artery: handheld multispectral optoacoustic tomography. *Radiology* **291**, 45-50 (2019).
- 88 Li, L., Hsu, H. C., Verkhusha, V. V., Wang, L. V. & Shcherbakova, D. M. Multiscale Photoacoustic Tomography of a Genetically Encoded Near-Infrared FRET Biosensor. *Advanced Science* **8**, 2102474 (2021).
- 89 Zhang, P., Li, L., Lin, L., Shi, J. & Wang, L. V. In vivo superresolution photoacoustic computed tomography by localization of single dyed droplets. *Light: Science & Applications* **8**, 1-9 (2019).
- 90 Yang, J. *et al.* Photoacoustic assessment of hemodynamic changes in foot vessels. *Journal of biophotonics* **12**, e201900004 (2019).
- 91 Hariri, A. *et al.* The characterization of an economic and portable LED-based photoacoustic imaging system to facilitate molecular imaging. *Photoacoustics* **9**, 10-20 (2018).
- 92 Allen, T. J. & Beard, P. C. High power visible light emitting diodes as pulsed excitation sources for biomedical photoacoustics. *Biomedical optics express* **7**, 1260-1270 (2016).
- 93 Daoudi, K. *et al.* Handheld probe integrating laser diode and ultrasound transducer array for ultrasound/photoacoustic dual modality imaging. *Optics express* **22**, 26365-26374 (2014).
- 94 Upputuri, P. K. & Pramanik, M. Performance characterization of low-cost, high-speed, portable pulsed laser diode photoacoustic tomography (PLD-PAT) system. *Biomedical optics express* **6**, 4118-4129 (2015).
- 95 Mienkina, M. P. *et al.* Multispectral photoacoustic coded excitation imaging using unipolar orthogonal Golay codes. *Optics Express* **18**, 9076-9087 (2010).

- 96 Su, S.-Y. & Li, P.-C. Coded excitation for photoacoustic imaging using a high-speed diode laser. *Optics express* **19**, 1174-1182 (2011).
- 97 Mienkina, M. P. *et al.* Experimental evaluation of photoacoustic coded excitation using unipolar golay codes. *IEEE transactions on ultrasonics, ferroelectrics, and frequency control* **57**, 1583-1593 (2010).
- 98 Zhang, H. K., Kondo, K., Yamakawa, M. & Shiina, T. Coded excitation using periodic and unipolar M-sequences for photoacoustic imaging and flow measurement. *Optics Express* **24**, 17-29 (2016).
- 99 Zhou, M., Xia, H., Zhong, H., Zhang, J. & Gao, F. A noise reduction method for photoacoustic imaging in vivo based on EMD and conditional mutual information. *IEEE Photonics Journal* **11**, 1-10 (2019).
- 100 Sun, M., Feng, N., Shen, Y., Shen, X. & Li, J. Photoacoustic signals denoising based on empirical mode decomposition and energy-window method. *Advances in Adaptive Data Analysis* **4**, 1250004 (2012).
- 101 Donoho, D. L. & Johnstone, J. M. Ideal spatial adaptation by wavelet shrinkage. *biometrika* **81**, 425-455 (1994).
- 102 Zhou, M. *et al.* in *2018 40th Annual International Conference of the IEEE Engineering in Medicine and Biology Society (EMBC)*. 4796-4799 (IEEE).
- 103 Van de Sompel, D., Sasportas, L. S., Jokerst, J. V. & Gambhir, S. S. Comparison of deconvolution filters for photoacoustic tomography. *PloS one* **11**, e0152597 (2016).
- 104 Manwar, R. *et al.* Photoacoustic signal enhancement: towards utilization of low energy laser diodes in real-time photoacoustic imaging. *Sensors* **18**, 3498 (2018).
- 105 Nilsen, C.-I. C. & Holm, S. Wiener beamforming and the coherence factor in ultrasound imaging. *IEEE transactions on ultrasonics, ferroelectrics, and frequency control* **57**, 1329-1346 (2010).
- 106 Jeon, S. *et al.* Real-time delay-multiply-and-sum beamforming with coherence factor for in vivo clinical photoacoustic imaging of humans. *Photoacoustics* **15**, 100136 (2019).
- 107 Park, S., Karpouk, A. B., Aglyamov, S. R. & Emelianov, S. Y. Adaptive beamforming for photoacoustic imaging. *Optics letters* **33**, 1291-1293 (2008).
- 108 Friedlein, J. T. *et al.* Dual-comb photoacoustic spectroscopy. *Nature communications* **11**, 1-10 (2020).
- 109 Telenkov, S. & Mandelis, A. Signal-to-noise analysis of biomedical photoacoustic measurements in time and frequency domains. *Review of Scientific Instruments* **81**, 124901 (2010).
- 110 Lengenfelder, B. *et al.* Remote photoacoustic sensing using speckle-analysis. *Scientific reports* **9**, 1-11 (2019).
- 111 Wang, Y. *et al.* In vivo three-dimensional photoacoustic imaging based on a clinical matrix array ultrasound probe. *Journal of Biomedical Optics* **17**, 061208 (2012).
- 112 Kothapalli, S.-R. *et al.* Deep tissue photoacoustic imaging using a miniaturized 2-D capacitive micromachined ultrasonic transducer array. *IEEE Transactions on Biomedical Engineering* **59**, 1199-1204 (2012).
- 113 Wang, L., Maslov, K. I., Xing, W., Garcia-Urbe, A. & Wang, L. V. Video-rate functional photoacoustic microscopy at depths. *Journal of biomedical optics* **17**, 106007 (2012).
- 114 Shi, J. *et al.* High-resolution, high-contrast mid-infrared imaging of fresh biological samples with ultraviolet-localized photoacoustic microscopy. *Nature photonics* **13**, 609-615 (2019).

- 115 Yang, J. *et al.* Motionless volumetric photoacoustic microscopy with spatially invariant resolution. *Nature communications* **8**, 1-7 (2017).
- 116 Shi, J., Wang, L., Noordam, C. & Wang, L. V. Bessel-beam Grueneisen relaxation photoacoustic microscopy with extended depth of field. *Journal of biomedical optics* **20**, 116002 (2015).
- 117 Wang, L., Maslov, K., Yao, J., Rao, B. & Wang, L. V. Fast voice-coil scanning optical-resolution photoacoustic microscopy. *Optics letters* **36**, 139-141 (2011).
- 118 Cebrecos, A. *et al.* Beamforming for large-area scan and improved SNR in array-based photoacoustic microscopy. *Ultrasonics* **111**, 106317 (2021).
- 119 Deán-Ben, X. L., López-Schier, H. & Razansky, D. Photoacoustic micro-tomography at 100 volumes per second. *Scientific reports* **7**, 1-8 (2017).
- 120 Paul, S., Mandal, S. & Singh, M. S. Noise adaptive beamforming for linear array photoacoustic imaging. *IEEE Transactions on Instrumentation and Measurement* **70**, 1-11 (2021).
- 121 Yao, J., Ke, H., Tai, S., Zhou, Y. & Wang, L. V. Absolute photoacoustic thermometry in deep tissue. *Optics letters* **38**, 5228-5231 (2013).
- 122 Liu, S., Feng, X., Ruochong, Z. & Zheng, Y. in *2018 IEEE International Symposium on Circuits and Systems (ISCAS)*. 1-5 (IEEE).
- 123 Xiaohua, F., Fei, G. & Yuanjin, Z. Photoacoustic-based-close-loop temperature control for nanoparticle hyperthermia. *IEEE Transactions on Biomedical Engineering* **62**, 1728-1737 (2015).
- 124 Li, Y. L., Hyun, D., Abou-Elkacem, L., Willmann, J. K. & Dahl, J. J. Visualization of small-diameter vessels by reduction of incoherent reverberation with coherent flow power doppler. *IEEE transactions on ultrasonics, ferroelectrics, and frequency control* **63**, 1878-1889 (2016).
- 125 Instruments, T. *Ultrasound smart probe - Products and reference designs*, <<https://www.ti.com/solution/ultrasound-smart-probe?variantid=35221>> (2018).
- 126 Wray, P., Lin, L., Hu, P. & Wang, L. V. Photoacoustic computed tomography of human extremities. *Journal of biomedical optics* **24**, 026003 (2019).
- 127 Li, L. *et al.* Small near-infrared photochromic protein for photoacoustic multi-contrast imaging and detection of protein interactions in vivo. *Nature communications* **9**, 1-14 (2018).
- 128 Vu, T. *et al.* Photoacoustic computed tomography of mechanical HIFU-induced vascular injury. *Biomedical Optics Express* **12**, 5489-5498 (2021).
- 129 Zhang, Y. & Wang, L. Video-rate ring-array ultrasound and photoacoustic tomography. *IEEE Transactions on Medical Imaging* **39**, 4369-4375 (2020).